



UNIVERSIDAD NACIONAL AUTÓNOMA DE MÉXICO
PROGRAMA DE POSGRADO EN ASTROFÍSICA
INSTITUTO DE RADIOASTRONOMÍA Y ASTROFÍSICA

**FPGA-BASED BACK-END FOR
K-BAND WATER VAPOR RADIOMETRY
AT RADIO ASTRONOMY OBSERVATORIES**

T E S I S

PARA OPTAR POR EL GRADO DE:

MAESTRO EN CIENCIAS (ASTROFÍSICA)

PRESENTA

JETZAEI CUAZOSON GÓMEZ

TUTORES

DR. STANLEY E. KURTZ,

INSTITUTO DE RADIOASTRONOMÍA Y ASTROFÍSICA

DR. DANIEL FERRUSCA RODRÍGUEZ,

INSTITUTO NACIONAL DE ASTROFÍSICA, ÓPTICA Y ELECTRÓNICA

MORELIA, MICHOACÁN.

FEBRERO DE 2024.



Universidad Nacional
Autónoma de México

Dirección General de Bibliotecas de la UNAM

Biblioteca Central



UNAM – Dirección General de Bibliotecas
Tesis Digitales
Restricciones de uso

DERECHOS RESERVADOS ©
PROHIBIDA SU REPRODUCCIÓN TOTAL O PARCIAL

Todo el material contenido en esta tesis esta protegido por la Ley Federal del Derecho de Autor (LFDA) de los Estados Unidos Mexicanos (México).

El uso de imágenes, fragmentos de videos, y demás material que sea objeto de protección de los derechos de autor, será exclusivamente para fines educativos e informativos y deberá citar la fuente donde la obtuvo mencionando el autor o autores. Cualquier uso distinto como el lucro, reproducción, edición o modificación, será perseguido y sancionado por el respectivo titular de los Derechos de Autor.

*Con mucho cariño para Isabel y Éridan,
mi inspiración y motivación.*

*Para Zahira y Cristian,
en un abrir y cerrar de ojos, volveremos a encontrarnos.*

AGRADECIMIENTOS

A mi esposa e hijo, que me acompañan y motivan a continuar escalando en este proyecto de vida. También, a mis padres y hermanos, por siempre estar al tanto de nuestro bienestar a pesar de vivir tan distanciados de nosotros. ¡Los amo mucho!

El posgrado hubiese totalmente distinto sin mis compañeros de generación. Agradezco a todos por compartir sus experiencias, tiempo y aventuras: Dante, Jafet, Johanan, Mauricio, Bianca, Diego e Itzel.

Me siento absolutamente agradecido con mis directores, Stan Kurtz y Daniel Ferrusca por siempre estar al pendiente de mi trayectoria desde hace unos cuantos años y hasta ahora. Los considero parte fundamental de mi desarrollo académico. Agradezco también sus sabios consejos, personales y profesionales. Sin duda alguna, unos mentores en toda la extensión de la palabra.

Agradezco a los miembros del jurado, los Drs. Alice Passeto, Roberto Galván, Miguel Velázquez, David Hiriart y Erika Sohn por su valioso tiempo y por brindarme ideas sustanciales al mejoramiento de este trabajo recepcional. Extiendo este agradecimiento a los Drs. Eduardo Ibarra y de nuevo a David Hiriart por su invaluable asesoramiento académico en tópicos de radiometría, electrónica de microondas y caracterización de sitios. Las pláticas con ustedes siempre han sido muy enriquecedoras.

Aprendí una nueva perspectiva y un particular sentido de fraternidad profesional en el IRyA. Por ello, me gustaría agradecer al personal académico, técnico y administrativo por su ayuda durante mi estadía en el instituto en estos años.

Este trabajo de tesis fue realizado con fondos del Programa de Apoyo a Proyectos de Investigación e Innovación Tecnológica (PAPIIT) de la UNAM otorgada a los proyectos 564-IT100318 y 480-IT101622. Agradezco ampliamente a la DGAPA-UNAM la beca recibida durante este etapa.

Finalmente, externo mi agradecimiento al CONAHCYT por la Beca Nacional Tradicional otorgada al CVU 1032576 durante la duración de mis estudios de posgrado.

Sinceramente,

Jetzael

ABSTRACT

Atmospheric characterization is an important activity performed at astronomical observatories. In addition to provide parameters for data calibration, atmospheric monitoring helps with the management of observation time according to seasonal and diurnal variations in the atmosphere. A microwave radiometer is a powerful remote sensing tool that is often used for this purpose at radio astronomy observatories. In this work we present the design and integration of a versatile and low-cost digital back-end for radiometric water vapor measurements from a generic K-band receiver. The system consists of an analog conditioning stage which down-converts the frequency of the receiver signal for proper digitization. A dedicated high-performance Field-Programmable Gate Array-based platform performs the signal acquisition and processing of the power spectrum in order to get both zenith opacity and precipitable water vapor. Given its technical capabilities, the back-end will facilitate some substantial tasks for the TUL-1 dish antenna (32-m) at Tulancingo, Mexico: the instrument will provisionally contribute to the short- and long-term atmospheric characterization of the site with the possibility of extrapolating its use for continuum and spectral-line astronomical measurements in K-band. Moreover, the system will also be able to perform atmospheric monitoring for other existing and future radio astronomy sites, including potential ngVLA antenna sites in northern Mexico.

RESUMEN

La caracterización atmosférica es una actividad importante que se realiza en los observatorios astronómicos. Además de proporcionar parámetros para la calibración de datos, el monitoreo atmosférico ayuda a gestionar el tiempo de observación en función de las variaciones estacionales y diurnas de la atmósfera. Un radiómetro de microondas es una potente herramienta de teledetección que se utiliza muy a menudo para este propósito en los observatorios de radioastronomía. En este trabajo presentamos el diseño e integración de un back-end digital versátil y de bajo coste para mediciones radiométricas de vapor de agua a partir de un receptor genérico en banda K. El sistema consta de una etapa de acondicionamiento analógico que reduce la frecuencia de la señal del receptor para su correcta digitalización. Una plataforma basada en una Matriz de Compuertas Programables en Campo de alto rendimiento realiza la adquisición de la señal y el procesado del espectro de potencia para obtener tanto la opacidad cenital como el vapor de agua precipitable. Dadas sus capacidades técnicas, el back-end facilitará algunas tareas sustanciales para la antena TUL-1 (32 m) en Tulancingo, México: el instrumento contribuirá provisionalmente a la caracterización atmosférica a corto y largo plazo del sitio con la posibilidad de extrapolar su uso para mediciones astronómicas del continuo y líneas espectrales en banda K. Además, este instrumento también podrá realizar el monitoreo atmosférico de sitios radioastronómicos existentes y futuros, incluidos sitios potenciales para antenas ngVLA en el norte de México.

CONTENTS

Abstract	i
Resumen	iii
Contents	vi
Figure List	vii
Table List	x
1 Introduction	1
1.1 The Earth's Atmosphere	1
1.2 Water Absorption	3
1.2.1 Water Vapor or Liquid Water?	4
1.2.2 Energy Transitions	4
1.2.3 Water Vapor at Microwaves	5
1.3 Water Vapor Radiometry in Radio Astronomy	7
1.3.1 Phase Correction	8
1.3.2 Site Characterization	8
1.3.3 Atmospheric Monitoring	10
1.4 Project Approach	11
2 Microwave Radiometry	15
2.1 Radiometric Measurements	15
2.2 Instrument Calibration	17
2.3 Radiometer Architectures	19
3 Radiometric Data Retrieval	25
3.1 Retrieval theory	25
3.1.1 The Forward Problem	25
3.1.2 The Inverse Problem	26
3.2 Microwave Radiative Transfer Equation	26
3.3 Tip-Scan Method	27
3.4 Precipitable Water Vapor Retrieval	29
4 Radiometer Design	33

4.1	Conceptual Design	33
4.1.1	HartRAO Receiver	34
4.1.2	Instrumental Integration Time and Spectral Resolution	36
4.1.3	Required Spectral Resolution	39
4.2	Back-end Stage	43
4.2.1	Analog Filter Bank	44
4.2.2	Tunable Oscillator	44
4.2.3	Digital Spectrometer	45
4.3	Prototype	46
4.3.1	Architecture	46
4.3.2	Down-Conversion Stage	47
4.3.3	Digitization System	49
4.3.4	Implemented Spectrometer	52
4.3.5	Assembly	55
4.3.6	Costs	57
5	Radiometer Features	59
5.1	Analog Features	59
5.1.1	Bandwidth	59
5.1.2	Gain	59
5.1.3	Noise Figure	61
5.1.4	Sensitivity	62
5.1.5	Spurs	63
5.2	Digital Features	67
5.2.1	Power Calibration	67
5.2.2	Spectral Resolution	68
5.2.3	Spectrum Acquisition and Visualization	69
5.3	Summary	72
6	Final Discussion	73
6.1	Instrument Performance	73
6.2	Future Work	77
6.3	Scientific Products	78
	References	88
A	CASA Tools: <i>atmosphere</i>	89
A.1	Atmospheric Profile	90
A.2	Spectral Window	90
A.3	Atmospheric Variables	91
A.4	Practical Example	91
B	Scripts	95
C	Schematics	107
D	Intermodulation Products	111

LIST OF FIGURES

1.1	The atmospheric transmission permits ground-based observations only in the visible and radio windows. Note that, in terms of frequency, the ~ 300 GHz bandwidth of the radio window fits within the ~ 320 THz bandwidth of the visible range. Drawing taken from Granato (2010)	2
1.2	Simulated zenith transmission for three different atmospheric profiles. Modeling parameters are shown in the inner box. Image taken from Ulaby and Long (2014)	2
1.3	Water vapor and oxygen attenuation for an atmospheric profile of Kolkata, India. Input parameters of the models are shown in the inner box. Image taken from (Karmakar, 2014).	3
1.4	Vibrational energy levels of the water molecule (K-ladder diagram). The diagram divides the <i>para</i> paramagnetic states (magnetic moment $m_l = 0$) located to the left of ground state $0(0,0)$, whereas the <i>ortho</i> paramagnetic states ($m_l = 1$) are located to the right. Figure taken from Neufeld et al. (2013) and reproduced by permission of the AAS.	5
1.5	Signal phase delay caused by water vapor.	8
1.6	Mt Gamsberg in Namibia. The plateau covers an effective surface for construction of 2.3 km^2 . Photo taken by Schilling (2017)	9
1.7	Sierra Negra (left) is the neighbor mountain of Citlaltépetl volcano (right). The LMT is located at the top of Sierra Negra. Photo from Wikipedia (2023)	9
1.8	RPG-Tip-225 radiometer installed at the roof of the LMT's Visitor Center building.	10
1.9	Start-up of WVR III+ at HartRAO. The COVID-19 pandemic in 2020 delayed the installation of the instrument until late 2021. Photo credit: Stander et al. (2022)	11
1.10	32-m Tulancingo antennas: TUL-1 (left) and TUL-2(right). Photo credits: E. Ibarra-Medel, S. Kurtz.	11
1.11	Artistic impression of the ngVLA antennas. Image from ngVLA (2023)	12
1.12	Estimated ngVLA antennas locations. The array covers a large part of the North American territory. Map from ngVLA (2023)	12
2.1	Zenith angle geometry.	15
2.2	Typical observation for ground-based microwave radiometry. Adapted from Janssen (1993)	16
2.3	Radiometer calibration curves: (a) two-point and (b) three-point measurements.	17

2.4	Radiometer (<i>Device Under Test</i> , or DUT) calibration setup. Adapted from (Skou and Vine, 2006).	18
2.5	Total power radiometer architecture.	20
2.6	Dicke radiometer architecture.	21
2.7	Basic microwave spectrometer architectures.	23
3.1	The forward-problem process. Adapted from Ulaby and Long (2014).	25
3.2	The inverse-problem process. Adapted from Ulaby and Long (2014).	26
3.3	System noise temperature as a function of air mass.	29
3.4	Linear relations between PWV, zenith opacity and relative humidity.	30
4.1	Conceptual design of the K-band water vapor radiometer. We will focus on the design and testing of the back-end stage.	33
4.2	Uncovered HartRAO K-band receiver at LIRA.	34
4.3	Schematics of HartRAO receiver. Adapted from Stander (2021).	35
4.4	Receiver noise temperature of KRx around 22 GHz. Taken from Stander (2021).	37
4.5	Integration time as function of SNR. As bandwidth decreases (i.e. better resolution), it takes more integration time to reach a certain SNR.	38
4.6	Simulated profiles around water vapor line at 22.235 GHz.	40
4.7	Brightness temperature models and their respective fitted models compared to the theoretical profile.	42
4.8	RMSE between models as a function of number of channels.	43
4.9	Proposal of a filter-bank radiometer.	44
4.10	Proposal of a tunable-oscillator radiometer.	45
4.11	Proposal of a digital spectrometer.	45
4.12	Prototype's architecture.	47
4.13	Schematics of down-conversion stage.	47
4.14	Frequency conversion maps.	48
4.15	Digitization system topology.	49
4.16	Simple implementation of CASPER rfdc acquisition block for the RFSoc 2x2 board.	51
4.17	RFSoc programming process.	52
4.18	Digital architecture of the spectrometer.	52
4.19	Design of the digital spectrometer: Simulink's block diagram and its sections.	54
4.20	Mounting scheme of the back-end.	55
4.21	Final assembly of the back-end (bottom) and the KRx(top). Several other components are also indicated.	56
5.1	Back-end gain measurements.	60
5.2	Gains of the back-end channels. The gains of each channel at 1 GHz are labeled.	60
5.3	Noise figure of the back-end channels. The noise figures of each channel at 1 GHz are labeled.	61
5.4	Setup to measure the response to a 50-Ohm load.	63
5.5	Output spectra and spurs captured with the analyzer.	64
5.6	Spur spectrum due to the DDC. Only components between ± 1000 MHz appear in the output spectrum.	65

5.7	Spurs in the channels of the back-end. We plot both the low and high-resolution modes.	66
5.8	Measurement setup for power calibration.	68
5.9	Power calibration for the digital stage.	68
5.10	Spectrum acquisition and visualization flowchart.	70
5.11	Response spectra in the channels of the back-end.	71
6.1	Schematics of the water vapor radiometer designed by Rojas-Méndez (in prep)	77
6.2	Poster presented at the LXVI CNF.	79
A.1	Left: Transmission at the VLA site. Right: Zenith opacity. The PWV was 2 mm.	93
A.2	Atmospheric transmission for different PWV values at VLA.	93
C.1	Digital spectrometer block diagram.	108
C.2	Down-conversion connections.	109

LIST OF TABLES

3.1	Resulting PWV and zenith opacity from simulations at 22.235 GHz.	30
4.1	Technical specifications of HartRAO receiver (Stander, 2021).	36
4.2	Integration time for given bandwidth and SNR.	38
4.3	Group size, data rows and bandwidth per channel of calculated models. . . .	40
4.4	Estimated coefficients of fitted models.	41
4.5	Statistics of fitted models.	41
4.6	RMSE between models. Note that the $RMSE = 0$ in the 'a - a' row, since the model is compared to itself.	42
4.7	RF devices used for the down-conversion stage.	48
4.8	RFSoc key features (Xilinx, Inc., 2023).	49
4.9	Compatibility of software versions for the RFSoc 2x2.	50
4.10	DC features of power supplies.	55
4.11	AC features of the power supplies.	56
4.12	Back-end budget.	57
5.1	Analog spurs of the back-end.	63
5.2	Input parameters of Frequency Planner tool.	64
5.3	Spurs due to the DDC.	64
5.4	Spurs observed after digitization.	66
5.5	Significant spurs of the back-end.	67
5.6	Back-end main analog features.	72
5.7	Instrument features.	72
A.1	Arguments requested by <code>initAtmProfile</code> method.	90
A.2	Arguments requested by <code>initSpectralWindow</code> method.	90
A.3	Some <i>atmosphere's</i> variables on demand by the user.	91
A.4	VLA's weather conditions and spectral window arguments.	91
D.1	IP3 terms for $\nu_{RF} = 3.1$ GHz to 7.1 GHz and $\nu_{LO} = 3.1$ GHz.	112
D.2	IP3 terms for $\nu_{RF} = 3.1$ GHz to 7.1 GHz and $\nu_{LO} = 7.1$ GHz.	113

CHAPTER 1

INTRODUCTION

Radiometry is a science that deals with the measurement of radiation in any region of the electromagnetic spectrum. It is a set of techniques associated with the characterization of light by its radiation power. Particularly, microwave radiometry is dedicated to measuring energy emitted at radio frequencies from ~ 300 MHz to ~ 300 GHz. The main instrument used in this field is the radiometer: a practical electronic receiver that measures the noise power of an incoming signal (Karmakar, 2014).

Various engineering features make the radiometer a practical and versatile instrument in several fields: geosciences (Wang et al., 2020), military (Corlay et al., 2017), agroforestry (Gutiérrez-Guzmán et al., 2017), and even medicine (Groumpas et al., 2020). For radio astronomy, the radiometer has multiple applications: signal phase correction in interferometry-based observatories; atmospheric monitoring in both single-dish and interferometric radio telescopes; and site characterization for evaluating the potential of a radio astronomical site. We are interested in these radio astronomy applications, and particularly, the atmospheric monitoring with microwave radiometers.

In this chapter we briefly explore the fundamentals of microwave radiometry: starting from the atmospheric absorption phenomenon due to water vapor in the atmosphere and ending with the scientific applications of radiometers for radio astronomy. These topics will provide a proper panorama of the sense of this thesis, but we suggest that the reader consult the references to complement the information described here.

1.1 The Earth's Atmosphere

The chemical composition and thermodynamics of the Earth's atmosphere cause the absorption of high energy (short-wavelength) electromagnetic radiation. On the other hand, optical and radio wavelengths avoid the absorption phenomenon so that ground-based observations can be performed (Condon and Ransom, 2016). Although astronomers use the full electromagnetic spectrum, ground-based observations are only possible in certain atmospheric windows as shown in Fig. 1.1. We will focus on studying the relevance of atmospheric effects in the radio window.

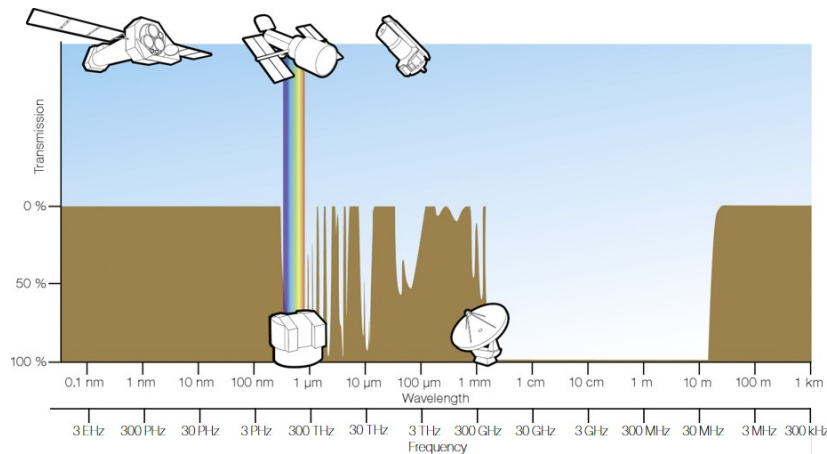


Fig. 1.1: The atmospheric transmission permits ground-based observations only in the visible and radio windows. Note that, in terms of frequency, the ~ 300 GHz bandwidth of the radio window fits within the ~ 320 THz bandwidth of the visible range. Drawing taken from [Granato \(2010\)](#).

The atmosphere is not completely transparent to radio waves. There is a slight amount of attenuation due to chemical composition and weather variations in the atmosphere, which must be considered to perform accurate radio astronomical observations. Fig. 1.2 shows the main components that contribute to attenuation in the atmosphere at frequencies up to 300 GHz. As can be seen, polar type atmospheres present better transmission capacity (or less attenuation) due to high air dryness, in contrast with tropical conditions. In addition, transmission by oxygen has minima at 60 GHz and 118 GHz, and the water line is important in both the 22 and 183 GHz bands ([Ulaby and Long, 2014](#)).

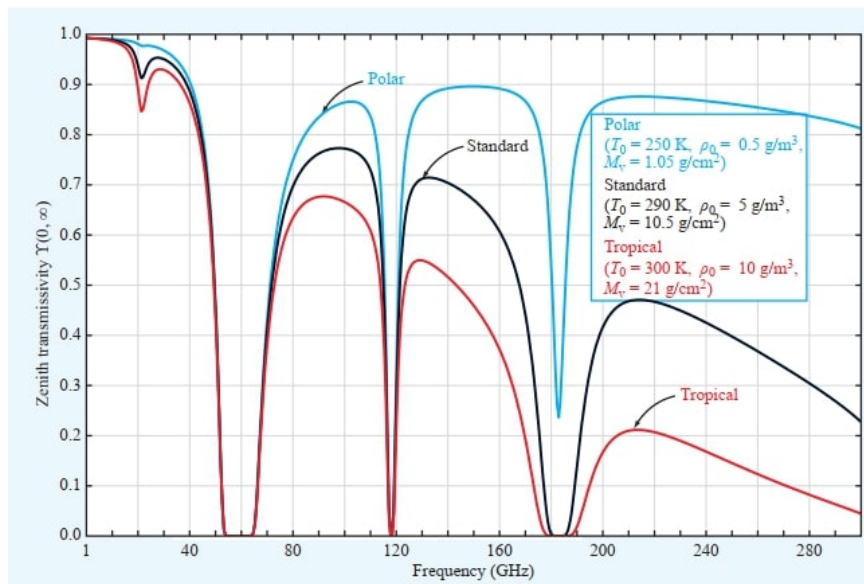


Fig. 1.2: Simulated zenith transmission for three different atmospheric profiles. Modeling parameters are shown in the inner box. Image taken from [Ulaby and Long \(2014\)](#).

Generally, it is possible to anticipate the behavior of the atmosphere at microwave frequencies by simulations using radiative transfer algorithms, such as *an atmospheric model* by Paine (2022) or *Atmospheric Transmission at Microwaves (ATM)* by Pardo et al. (2001)¹. For instance, Karmakar (2014) simulated the atmospheric attenuation in an arbitrary location at Kolkata, India. Fig. 1.3 shows the individual and combined attenuation due to water vapor and oxygen up to 225 GHz.

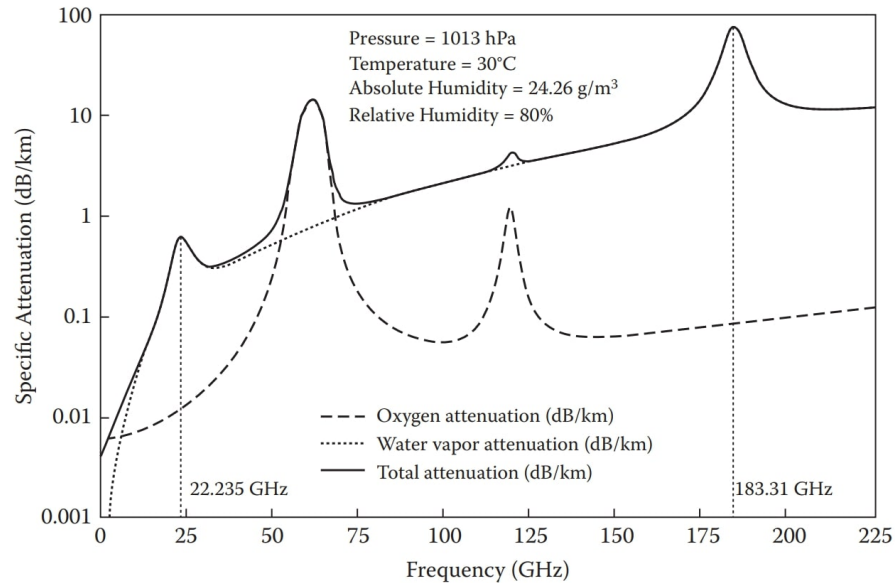


Fig. 1.3: Water vapor and oxygen attenuation for an atmospheric profile of Kolkata, India. Input parameters of the models are shown in the inner box. Image taken from (Karmakar, 2014).

Evidently, water vapor and oxygen exhibit a strong attenuation (or weak transmission capacity) in certain frequency ranges around resonant frequencies of these molecules. We highlight the role of water vapor in the atmosphere because at radio astronomy observatories, the water vapor absorption at centimeter and millimeter bands must be accounted for practical observations, both for signal attenuation and phase corrections.

1.2 Water Absorption

The properties of the water molecule and its interaction with light in our atmosphere are of particular interest in radio astronomy. To understand how the signal attenuation and phase correction are handled by radio astronomers, it is important to explain the absorption phenomenon from the basics. Thus we begin with a brief description of the physics of the water molecule and the differences between its liquid and gaseous phases. After that, we present the challenges of observing at 22 and 183 GHz bands.

¹both with a radio astronomy approach.

1.2.1 Water Vapor or Liquid Water?

The reader may note that we refer many times to *water vapor* (gaseous phase), but why not to liquid water? We briefly discuss this seemingly subtle difference here.

Water is a minor component of our atmosphere. However, the presence of water in the line-of-sight of an astronomical observation causes absorption and scattering. The physical state as water vapor or liquid water determines the way water interacts with electromagnetic radiation and consequently, how we characterize the amount of water in the atmosphere; each form has a different practical treatment for our radio astronomy purposes.

Water vapor is a group of water molecules in gaseous form. Given the size of molecules, the absorption and emission of light is most significant than scattering. Liquid water, on the other hand, refers to the water droplets (micrometer-sized) that make up clouds, which scatter and absorb radiation at a similar rate. By measuring the brightness temperature of the sky in the absence of background sources, we can characterize the radiative processes of both water forms as noise temperature sources.

The water vapor is measured by the *precipitable water vapor* (PWV). The PWV is the absolute amount of water vapor, measured in length units (e.g. mm or cm), dissolved in air. PWV refers to the depth that the molecules of water would occupy if the vapor were condensed into a liquid and distributed uniformly throughout the column (Kämpfer et al., 2013). Instead, the amount of liquid water (referred as *cloud liquid water*) can be measured by water mass per volume of air (e.g. g cm^{-3}) using a variety of techniques, such as radar or lidar (Ulaby and Long, 2014). In addition, Janssen (1993) suggests that cloud liquid water can be seen as a contaminant artifact for temperature profile calculations using microwave radiometry.

In contrast to optical observatories, where liquid water in the form of clouds is a fatal observing condition, in radio astronomy one can observe through clouds but it is the water vapor in the atmosphere which can produce a stronger effect. Additionally, water vapor is present in the atmosphere at all times, whether in dry or wet conditions. In this sense, we lean towards water vapor content in the atmosphere, and particularly to the troposphere, where most water vapor content is present (Janssen, 1993). The attenuation of incoming signals in microwave bands varies depending of the amount of atmospheric PWV, and it represents another parameter to be corrected in data calibration.

1.2.2 Energy Transitions

Water molecules, because of their internal structure, have both rotational and vibrational transitions: the former are caused by changes in rotational angular momentum, whereas vibrational transitions occur when the nuclei of the molecule change their separation by the fundamental vibrational modes. The rotational transitions of water fall in the centimeter to far-infrared (FIR) bands, and vibrational transitions correspond to the IR spectrum (Cernicharo, 2014). The main atmospheric absorption due to water vapor occurs at 22.235 GHz (cm-band) and 183.310 GHz (mm-band). The first occur between nuclear spin triplets in transition $J = 6$ to $J = 5$, and the second is between singlet spin in the transition $J = 3$ to $J = 2$ (Janssen, 1993). Some of the energy transitions of the H_2O molecule are shown in Fig. 1.4.

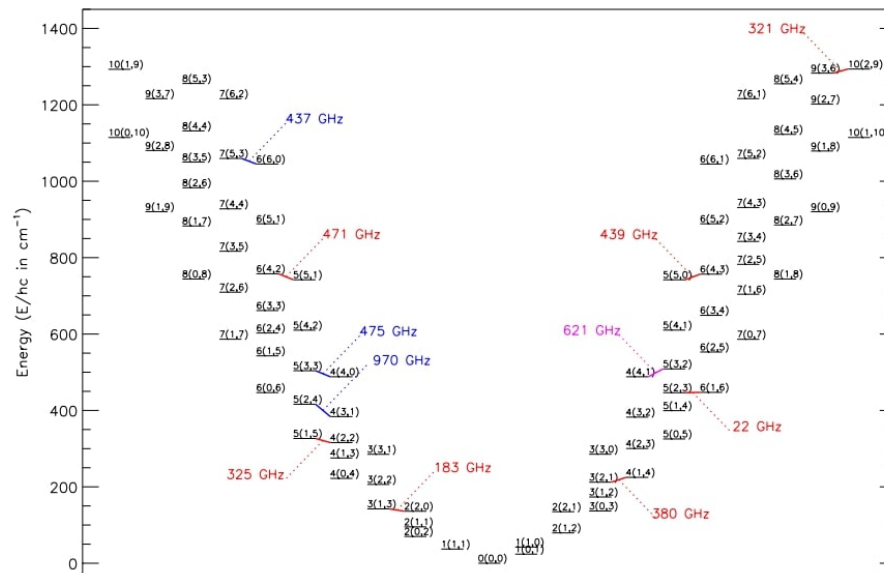


Fig. 1.4: Vibrational energy levels of the water molecule (K-ladder diagram). The diagram divides the *para* paramagnetic states (magnetic moment $m_l = 0$) located to the left of ground state $0(0,0)$, whereas the *ortho* paramagnetic states ($m_l = 1$) are located to the right. Figure taken from Neufeld et al. (2013) and reproduced by permission of the AAS.

Evidently, there are other water lines beyond 300 GHz in the diagram, e.g. at 325 or 448 GHz. However, we limit our study to the radiative effects of the water molecule in the atmosphere up to 40 GHz, since we are interested in emission in the K-band.

1.2.3 Water Vapor at Microwaves

Water vapor parameters can be retrieved from spectral measurements using a microwave radiometer centered at or near resonance frequencies of the water molecule, see e.g. Liu et al. (2021) and Otárola et al. (2009). This instrument observes the collision-broadened (also called pressure-broadened) emission lines caused by rotational transitions of water vapor in the microwave spectrum (Kämpfer et al., 2013). For our interests in atmospheric water vapor, we can use either 22 or 183 GHz lines for retrieval. Nevertheless, each water line has its own practical and physical issues, which influence the calculations in retrieval methods and must be considered for instrument design (Wang et al., 1989).

Line Intensity Water vapor emission is pressure-broadened at low altitudes and it is in a narrow line at high altitudes. The intensity of this emission is directly proportional to the vapor density, and it can be used for vertical content profiling (Solheim et al., 1998). The low opacity of the 22 GHz line limits the retrieval to only information about the vertical structures at low altitudes, while the 183 GHz emission line provides detailed vertical moisture profile above the tropopause (Westwater et al., 2004). On the other hand, atmospheric simulations, e.g. Karmakar (2012) or Ulaby and Long (2014), show that the line strength difference between 22 and 183 GHz is about two orders of magnitude, with the 183 GHz line being the more intense.

Line Shape Simulations also show that the 22 GHz line is relatively narrow of about 1 GHz width, whereas the 183 GHz line is broader, covering a few tens of GHz. Although several authors suggest that pressure-broadened lines can be modeled using, e.g. Van Vleck-Weisskopf or Voigt line shapes (Cruz-Pol et al., 1998; Paine, 2022), Gaussian or Lorentzian profiles can be used as a first approximation (Gaut, 1968; Westwater, 1978; Pardo et al., 2001). The choice of model depends on the conditions of the atmospheric environment, as well as the practical features of the instrumentation used to observe a certain line. For simplicity, we choose a Gaussian profile for modeling the atmospheric water vapor lines below in this work.

Sensitivity The stronger 183 GHz line can provide a higher Signal-to-Noise Ratio and, consequently, more accurate measurements (Kämpfer et al., 2013). However, this line poorly characterizes low altitude (high pressure) water vapor content, leading to the 22 GHz line being considered for ground-based atmospheric characterization (Haefele and Kämpfer, 2010). In addition, Wiedner (1998) found that the 183 GHz line can give a sensitivity (Kelvin per millimetres of PWV), of $\sim 4 - 20 \text{ K mm}^{-1}$, whereas the 22 GHz line achieves $\sim 0.4 \text{ K mm}^{-1}$. Also, the 183 GHz line begins to saturate with just 2 mm of PWV. Precisely because of the lower sensitivity to water vapor, the 22 GHz line is suitable for high humidity locations since the line is less prone to saturation (Ricaud et al., 2010). In terms of instrument design, the high sensitivity of the 22 GHz line leads to building radiometers with high sensitivity capabilities but with low-end frequency specifications, which indeed are more affordable than that of 183 GHz instruments.

Spectral Coverage Several water vapor radiometers use at least two frequency channels around 22 GHz or 183 GHz to improve accuracy and provide more robust retrieval algorithms, see e.g. Guiraud et al. (1979); Lutz et al. (1991); Liljegren (2002) or Schnitt et al. (2020). By surveying the sky at multiple frequency channels around water vapor lines, water vapor at different heights can be retrieved (Liu et al., 2021), and the physical conditions at the site can be obtained (Wiedner, 1998). Also, the liquid water contribution can be excluded since cloud liquid water emits radiation whose intensity is comparable (and consequently detectable) with water vapor's (England et al., 1992). Nevertheless, the technique of measuring multiple and widely separated spectral bands is only useful depending on the atmospheric parameters to retrieve. For some retrieval methods, it is enough to measure bands quite close to the water vapor lines.

Antennas Antenna size is often proportional to the wavelength to be observed. This means that 22 GHz antennas are likely to be larger than 183 GHz antennas, see e.g. the radiometers used by Ferrusca et al. (2020) or Pazmany (2007). Supposing that the designer chooses to implement feed horns for both 22 and 183 GHz radiometers, the feed horn size will be larger for a 22 GHz than a 183 GHz instrument. If the designer prefers to use *microstrip* technology rather than feed horns, the antenna size will be practically the same in both cases. By exploiting the use of microstrip, the entire radiometer can be integrated as a *System-On-Chip* architecture, as proposed by Behrens and Stander (2020) or (Sholley et al., 2003)). However, the use of feed horns generally means using wave-guides in the front-ends, and microstrip

allows to directly use coaxial lines instead from this part of the instrument, reflecting in the construction dimensions.

Cooled Systems A cooled radio-frequency receiver system provides low-noise, high sensitivity and gain stability. Due to the higher intensity and low sensitivity of the 183 GHz line, radiometers at this frequency often do not need a cooling stage (Wiedner, 1998). Since the 22 GHz systems need to be as (or more) sensitive as the water vapor line at this same frequency, these radiometric systems should be cooled, this being one more parameter to be considered in the budget. However, current electronics devices provide low-noise, robustness and stability without the need for a cooling system (Hills and Richer, 2000). This means that a cooling system is not strictly necessary for either frequency.

Budget In the context of radio frequency design, it is well-known that electronics at higher frequencies increases costs: the higher the frequency, the higher the budget should be. The main cause of this situation is the challenge of manufacturing and high-precise calibration of the features required for high frequency electronics. In this sense, the manufacture of a 22 GHz radiometric system will generally be less expensive than a 183 GHz.

To summarize these many considerations, we note that neither water line is usable for all purposes because each one has its advantages and disadvantages depending on the atmospheric parameters we are looking for. Whereas the 22 GHz line is strongly suitable for ground-based applications, the 183 GHz line is for high-altitude and space-borne atmospheric water vapor profiling. Hence, with the proper electronic design, any radiometer can be capable of detecting both lines, rescuing both its intensity and shape; the cost of building them will depend on the spectral channels and detection capabilities. If savings are sought, a single channel radiometer designed with modern electronics will be the suitable option for both 22 and 183 GHz lines. However, the geographical location of the site and the scientific purposes of the observatory are the entry factors that determine which radiometer has to be built. In the following section, we discuss the radio astronomical applications of radiometers, and from this we will take some important arguments to make such a decision.

1.3 Water Vapor Radiometry in Radio Astronomy

In addition to geosciences, climatology or forestry sciences, the radiometer also has relevance in radio astronomy, mainly for the correction of atmospheric effects. At single-dish observatories, it is the attenuation due to water vapor which affects the observations: the intensity of the signals degrades at higher frequencies, and even more so as the concentration of water vapor increases at the site (Wilson et al., 2013). On the other hand, at interferometric observatories, both the attenuation and phase fluctuations represent an observational issue, and both also worsen the situation when the water vapor concentration increases (Thompson et al., 2017). Thus, it is of utmost importance to keep the sky monitored in the short term to compensate for such phenomena, and in the long term to determine the seasonal transmission capacity of the site.

Throughout this chapter we have mentioned many times that the water vapor radiometer fulfills three fundamental functions in this field: the phase delay correction, site characterization, and atmospheric monitoring. Let us start with a briefly discuss of these issues.

1.3.1 Phase Correction

The phase correction has a strong relation with interferometric observations: the fluctuating amounts and the inhomogeneity of water vapor in the atmosphere leads to phase shifts of the incoming signals in observations (Wiedner, 1998). To understand this phenomenon, let us see Fig. 1.5.

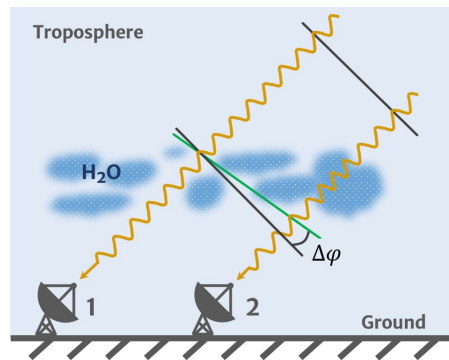


Fig. 1.5: Signal phase delay caused by water vapor.

The black line before the water vapor clumps, represents the undistorted wave front, and it must be perpendicular to the propagation direction from the source. The black line after the clumps must be the ideal wave front, which remains perpendicular to the propagation direction. However, due to the change in the refraction index between dry air and the water vapor clump, the actual wave front (green line) has been shifted by $\Delta\varphi$. In this way, the wave front will reach telescope 1 first, and after an extra delay $\Delta\varphi$, the signal will reach telescope 2. The de-phased signal must be corrected in the calibration process, and such compensation is the so-called *phase delay correction*.

By measuring the sky brightness temperature and retrieving the PWV in the direction of the antenna beam, the phase fluctuations can be compensated. Generally, these measurements are made with auxiliary radiometers in each antenna of the observatory. For a thorough review of the maths of phase fluctuations and implementation, we refer to *Section 13.1.6* of Thompson et al. (2017)

1.3.2 Site Characterization

Before the construction of radio astronomical observatories, it is important to make atmospheric studies to determine the potential of the site for radio astronomy purposes, and make geographic studies for civil engineering planning. Regarding the first issue, radiometers and weather stations are used for such objectives. Unlike phase correction applications, it is not necessary to install one radiometer per antenna, not even at the same line-of-sight.

The radiometers assigned for site characterization are located close to the telescopes and not only scan over the line-of-sight of the telescope, but do so for the entire sky of the site. Let us introduce two cases of site characterization in radio astronomy:

- (a) Mt Gamsberg in Namibia (see Fig. 1.6) has been considered as a potential site for mm-wave radio astronomy as part of the Africa Millimetre Telescope (AMT) (Backes et al., 2017). Moreover, Elsässer (2004) mentioned that the site has sky conditions comparable to La Silla in Chile, and the reports of Sarazin (1995) support the statement. In addition, a sky characterization using water vapor radiometers has been made by Frans (2020), which concludes that the amount of PWV over three years was comparable to the Chajnantor Plateau (Chile) and Mauna Kea (USA).



Fig. 1.6: Mt Gamsberg in Namibia. The plateau covers an effective surface for construction of 2.3 km². Photo taken by Schilling (2017).

- (b) Sierra Negra volcano (see Fig. 1.7) is the site of the Large Millimeter Telescope (LMT) in Mexico. At an elevation of 4580 m, the site provides the clearest and driest skies for mm-wave radio astronomy during winter and spring seasons (Zeballos et al., 2016). Due to excellent atmospheric conditions, the site was chosen among several candidates in Mexico for the construction of the LMT, such as San Pedro Mártir and Guadalupe Island mountains (Carramiñana, 2016). The atmospheric transmission studies before the construction of the telescope were fully reported by (Torres et al., 1997).



Fig. 1.7: Sierra Negra (left) is the neighbor mountain of Citlaltépetl volcano (right). The LMT is located at the top of Sierra Negra. Photo from Wikipedia (2023).

1.3.3 Atmospheric Monitoring

Having a well-monitored atmosphere is substantial for observation duties in radio astronomy. Atmospheric conditions strongly influence the decision of making observations mainly in the cm-band and mm-band. Regardless the general weather conditions, the atmospheric opacity determines the total attenuation of incoming signals in radio telescopes. This is where radiometers come into play: the real-time atmospheric monitoring, which is kind of a short term application of site characterization, or viewed from another perspective, the characterization after the construction and during scientific duties of the telescope. We introduce two currently-used instruments for this purpose:

- (a) The LMT is equipped with a 225 GHz water vapor radiometer (see Fig. 1.8). This instrument was designed by Radiometer Physics® and provides a real-time report of the atmospheric opacity due to water vapor, including weather conditions, at the mentioned band (Ferrusca and Contreras, 2014). The elevation and weather of the site make it an ideal place to monitor water vapor content at 183 GHz. However, as we have mentioned in Section 1.2.3, frequencies around this line can be used to estimate the water vapor. In the case of LMT, the 225 GHz band is used. Weather and atmospheric opacity reports in the LMT have been made using this instrument for the last 10 years (Zeballos et al., 2016; Ferrusca et al., 2022).



Fig. 1.8: RPG-Tip-225 radiometer installed at the roof of the LMT's Visitor Center building.

- (b) The atmospheric monitoring at Hartebeesthoek Radio Astronomy Observatory (HartRAO) in South Africa is made by the WVR III+ radiometer (see Fig. 1.9). This instrument was originally designed and constructed by the Swiss Federal Institute of Technology (ETH) and was later refurbished (renamed as WVR III+) early this decade by (Ferrusca et al., 2020), replacing several subsystems. The WVR III+ can perform measurements at 23.8 and 31.4 GHz to characterize the PWV and atmospheric opacity around the 22 GHz water vapor line, and the state-of-the-art embedded system provides several capabilities for both radio astronomy and geodesy studies (Cuazon et al., 2021).



Fig. 1.9: Start-up of WVR III+ at HartRAO. The COVID-19 pandemic in 2020 delayed the installation of the instrument until late 2021. Photo credit: Stander et al. (2022).

1.4 Project Approach

We are focusing this work on atmospheric characterization and site monitoring. The instrument presented in this thesis aims to adequately cover the tasks required for both issues, meeting the needs of existing and future observatories, like the discussed below.

Tulancingo Site The Tulancingo earth station is a telecommunications facility located in Hidalgo, Mexico. The station was inaugurated in 1968 and commissioned for the XIX Olympic Games transmission. In the late 1990s, the station ceased operations due to the various technological changes of the time. Fortunately, the Institute of Radio Astronomy and Astrophysics (IRyA), together with government organizations, initiated the refurbishment and conversion of the Tulancingo station as a radio astronomical observatory to operate from the L to K bands (Kurtz et al., 2022). Since 2017, the project started with the commissioning of the TUL-1 antenna (see Fig. 1.10).



Fig. 1.10: 32-m Tulancingo antennas: TUL-1 (left) and TUL-2(right). Photo credits: E. Ibarra-Medel, S. Kurtz.

To date, a large part of the mechanical and networking system of the TUL-1 has been rehabilitated (Kurtz et al., 2022) and the optics of the antenna have been characterized by

Velázquez et al. (2022). Receivers, even electronics for future front-ends have been proposed by Ibarra-Medel et al. (2022). Currently, two receivers have been built for the TUL-1 detection system: a C-band and K-band (Stander et al., 2022). However, the station lacks an instrument for atmospheric monitoring during telescope operations and the current seasonal atmospheric conditions at the site have yet to be assessed.

ngVLA Project The *next-generation Very Large Array* (see Fig. 1.11) is an interferometric array project that significantly enhances the spatial resolution and sensitivity at the same spectral bands as the best radio astronomical observatories to date (ngVLA, 2023). The ngVLA will operate in the 1.2 - 116 GHz spectral band, complementing the performance of the *Atacama Large Millimeter/submillimeter Array* (ALMA) at high frequencies and the *Square Kilometre Array Observatory* (SKAO) at low frequencies.



Fig. 1.11: Artistic impression of the ngVLA antennas. Image from ngVLA (2023).

The array consists of 244, 18 m diameter, and 19, 6 m diameter dish antennas. As can be seen in Fig. 1.12, the array will be distributed primarily in the U.S., and will extend into territories in Mexico and Canada; the core will be located at the actual *Karl G. Jansky Very Large Array* (VLA) location. So that, the ngVLA will reach microsecond resolution for precision astrometry, which will satisfy the key science goals of the project.

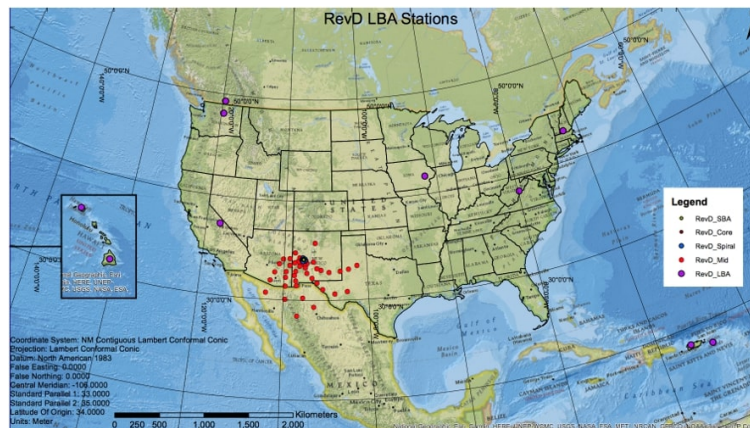


Fig. 1.12: Estimated ngVLA antennas locations. The array covers a large part of the North American territory. Map from ngVLA (2023).

Given that Northern Mexico is strongly considered for siting at least five of the array's antennas, locations in that area should be studied socioeconomically and characterized geographically to determine their feasibility as radio astronomical sites for the ngVLA. In this sense, a group of Mexican scientists, called the *Red Mexicana de Instrumentación para Radioastronomía* (REMIRA), seeks to perform the atmospheric characterization of potential sites in the North of the country using state-of-the-art technology and inter-institutional collaboration.

Taking into consideration the needs of these projects, a water vapor radiometer can be quite useful for tasks of characterization and evaluation of the sites, complementing the objectives of both work groups in the forthcoming years.

CHAPTER 2

MICROWAVE RADIOMETRY

So far we have dealt with the physical aspects of the water molecule behavior in the atmosphere as well as the astronomical applications, but we have yet to discuss the technical side of radiometry. Several engineering aspects of radiometry are discussed in this section; brightness temperature estimation, instrument response, including general architectures of radiometers.

2.1 Radiometric Measurements

To characterize the water vapor content of the atmosphere, we use the brightness temperature to quantify the emission by water molecules. But now the question is, how can we determine brightness temperature using a radiometer? To do so, we must find the relation between the amplitude of the radiometer response and the brightness temperature of the water emission.

Let us start by defining the geometry of ground-based measurements. The zenith opacity is described by the total opacity towards the zenith. As shown in Fig. 2.1, z is the angle formed by the zenith axis and the beam path at a given elevation.

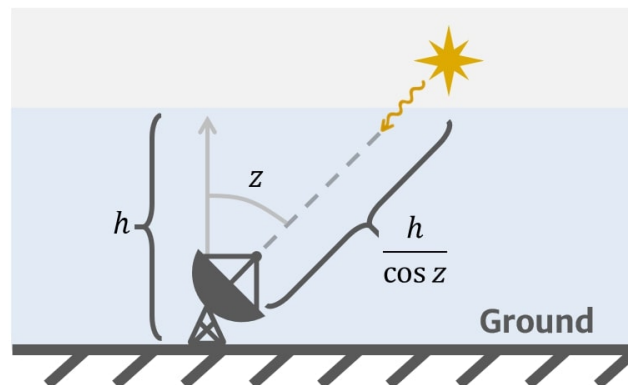


Fig. 2.1: Zenith angle geometry.

Using a plane parallel geometry (addressed in Chapter 3), the path length ℓ through the atmosphere is given by the height of the layer h and the zenith angle z as

$$\ell = \frac{h}{\cos z} = h \sec z . \quad (2.1)$$

The factor $\sec z$ in Eq. (2.1) is defined as the *air mass* X . Thus, we can express the path length simply as

$$\ell = hX . \quad (2.2)$$

If we perform a zenith measurement such that $z = 0$ (or $X = 1$), Eq. (2.2) becomes

$$\ell_0 = h , \quad (2.3)$$

which means that the telescope is pointed directly upwards, or at the zenith. In this way, we will refer to *zenith* variables with subscript 0, unless otherwise stated.

Suppose the scenario shown in Fig. 2.2 where a radiometric measurement is made: the radiometer (labeled as Rx) is pointing at a given zenith angle z .

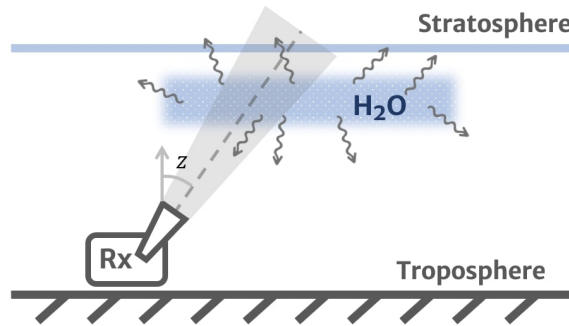


Fig. 2.2: Typical observation for ground-based microwave radiometry. Adapted from Janssen (1993).

Let S be the signal measured at the output of the radiometer in this measurement. For didactic purposes, let us say that S is given in voltage units. Following Janssen (1993), we assume a linear relationship between the receiver output signal and system noise temperature T_{sys} , in such a way that

$$S = GT_{\text{sys}} , \quad (2.4)$$

where G is system gain, which also can be seen as the voltage-temperature scaling factor. The *System Noise Temperature* refers to all noise contributions involved in the observation chain, both instrumental and external sources. Such contributions come from the atmospheric emission T_{atm} , the *cosmic microwave background* T_{cmb} , other background radio sources T_{rsb} , the *spill-over* radiation T_{spill} , the *receiver* temperature T_{rx} , among others (Burke et al., 2019), i.e.,

$$T_{\text{sys}} = T_{\text{atm}} + T_{\text{cmb}} + T_{\text{rsb}} + T_{\text{spill}} + T_{\text{rx}} + \dots \quad (2.5)$$

It is worth mentioning that real T_{sys} measurements indicate that the most significant temperature contributions are due to T_{sky} , T_{cmb} and T_{rx} . In practice, T_{rx} turns out to be much larger

than the other contributions, especially when we use a non-cryogenic receiver. So that, the system noise temperature can be approximated as

$$T_{\text{sys}} \approx T_{\text{atm}} + T_{\text{cmb}} + T_{\text{rx}} . \quad (2.6)$$

Additionally, T_{cmb} can be neglected only if T_{sky} and T_{rx} becomes much larger. In this sense, we can say that S is a direct measurement of the atmospheric brightness temperature. At this point, the signal is not particularly useful because we have not defined the gain (G) of the system and therefore, we require a calibration procedure for the instrument.

2.2 Instrument Calibration

The scaling factor G can be estimated by the slope of the voltage as a function of temperature, since we have assumed a linear relationship between them. A simple way to determine the slope is by measuring two points on the T_{sys} -voltage line and applying the standard definition of the slope. The idea is to measure the temperatures of two different blackbody sources using the radiometer (see Fig. 2.3a): a *cold* T_c , and a *hot* T_h temperature, such that $T_c < T_h$. Then, each measurement will have a respective voltage read-out, the cold V_c , and a hot V_h voltage. For the sake of illustration, we suppose that $V_c < V_h$.

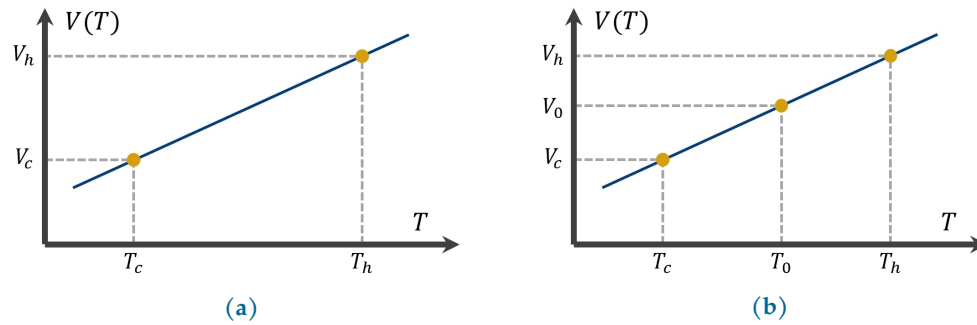


Fig. 2.3: Radiometer calibration curves: (a) two-point and (b) three-point measurements.

The curve $V(T)$ will be a line with a slope g and offset b , described by the equation

$$V(T) = gT + b . \quad (2.7)$$

The measurements will give the following set of voltages:

$$V_h = gT_h + b , \quad (2.8)$$

$$V_c = gT_c + b , \quad (2.9)$$

for the hot and cold load, respectively. If we solve these for g , we get the system gain

$$g = \frac{V_h - V_c}{T_h - T_c} , \quad (2.10)$$

and solving for b , we get the offset

$$b = \frac{V_c T_h - V_h T_c}{T_h - T_c} . \quad (2.11)$$

Thus, Eq. (2.7) becomes

$$V(T) = \left(\frac{V_h - V_c}{T_h - T_c} \right) T + \frac{V_c T_h - V_h T_c}{T_h - T_c}. \quad (2.12)$$

By setting $S \equiv V(T)$ and $T_{\text{sys}} \equiv T$ we relate Eq. (2.12) with Eq. (2.4) as

$$S = \left(\frac{V_h - V_c}{T_h - T_c} \right) T_{\text{sys}} + \frac{V_c T_h - V_h T_c}{T_h - T_c}. \quad (2.13)$$

Finally, we should determine the receiver temperature T_{rx} in order to characterize its contribution to the system temperature. Basically, the geometric T -intercept of the $V(T)$ line gives the receiver temperature. Taking advantage of the hot and cold measurements, we can use the classic Y -factor method (Pozar, 2011). The Y -factor is defined as the quotient of the hot load and the cold load voltages:

$$Y = \frac{T_h + T_{\text{rx}}}{T_c + T_{\text{rx}}} = \frac{V_h}{V_c}, \quad (2.14)$$

from which we can derive the receiver temperature

$$T_{\text{rx}} = \frac{T_h - Y T_c}{Y - 1}. \quad (2.15)$$

In the practical scenario, both sources must be well-defined and stable temperature sources. A suggested way is to use an electronic device called *noise generator*: while turned-on the device can be seen as the hot source; while turned-off we can assume a cold source. However, if $T_c \ll T_h$, the calibration loses reliability because only two points can not describe the $V(T)$ curve over a wide range because of the nearly-linear response of the instrument, and variations or errors in any point can drastically change the slope of the curve. An effective solution is to add a third point between T_c and T_h , since three points can describe the slope in a wide range, even if $T_c \ll T_h$. Let us call this intermediate measurement the *reference* temperature T_0 , as shown in Fig. 2.3b. By computing the average values of g and b of the three measurements, and following the steps shown in this section, this method will be more reliable than the two-point calibration. A practical suggestion to perform this method is given by Skou and Vine (2006), using the configuration shown in Fig. 2.4; emission of liquid nitrogen (LN₂) is used as the cold source, a noise generator signal is used as the hot source, and an impedance termination is used as reference source.

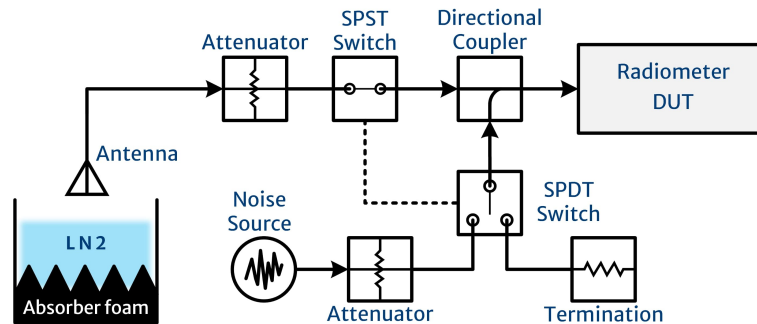


Fig. 2.4: Radiometer (Device Under Test, or DUT) calibration setup. Adapted from (Skou and Vine, 2006).

Several authors in the literature chose this calibration method, such as [Indermuehle et al. \(2013\)](#); [Miacci and Angelis \(2018\)](#), for its easy implementation, reliability in measurements and low-cost. However, we can find variants in the implementation, for instance:

- ▶ [Nagasaki et al. \(2016\)](#) uses a cooled radiometer system. The radiation emitted from inside the cryostat (40 K) is taken as a cold source, and it is measured through an optical window. A well-characterized (at ambient temperature) calibrator is used as the hot source. They point to the atmosphere to provide an intermediate temperature source. Then, the calibration is performed in a similar way to that mentioned above.
- ▶ [Fujisawa et al. \(2022\)](#) calibrates the antenna receiver systems by pointing at various temperature sources in the environment. The cold and intermediate temperature sources are taken from the atmosphere at different elevation angles, whereas the hot source is measured from an outside-temperature blackbody, which is a mountain near to the observatory. The authors suggest that, at least at the frequencies where the receivers work, measuring the radiation temperature of the mountain can give a higher accuracy in the calibration than measuring an ambient temperature source, as in the previous case.

These experiments can give us an entry scenario of the radiometer calibration in real-life. Some of the reasons we find various calibration techniques in the literature are that each method was designed according to the accuracy level demanded by the retrieval method, as well as the architecture capabilities of the radiometer. Ultimately, both items should converge in such a way that the needs of the observatory are met.

2.3 Radiometer Architectures

The radiometers we have mentioned so far, and those we will discuss later in this thesis, share some basic design elements, yet differ in others. Although from the structural implementation those instruments have obvious differences, the receiver chains are generally based on a fundamental architecture which is called the *total power radiometer*. These architectural differences are intended to improve one or more technical aspects of the radiometer, such as precision, gain fluctuations, even compatibility with next-generation devices.

Total Power Radiometer The total power radiometer (TPR) is considered as a *standard* architecture in radiometer design largely due to its simplicity. The main feature of the TPR is to provide an output voltage that is directly proportional to input power, i.e., to the brightness temperature observed with the antenna. The circuit is shown in [Fig. 2.5](#), from which is evident the implementation of a down-conversion mixing stage.

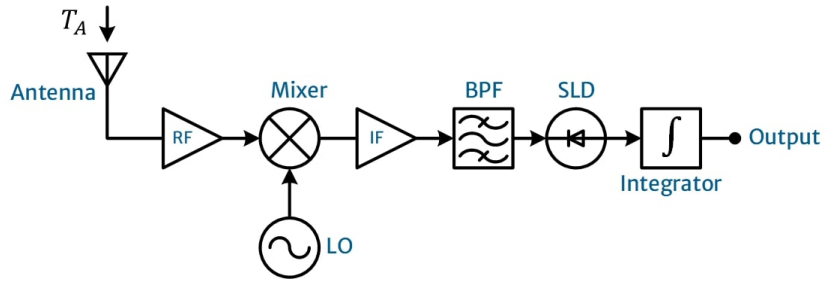


Fig. 2.5: Total power radiometer architecture.

The antenna signal is pre-amplified with the RF amplifier and then mixed with the Local Oscillator (LO) signal to produce an Intermediate Frequency (IF) signal at the mixer's output. The mixed signal is amplified by the IF Amp and it passed through a Band Pass Filter (BPF) to clean the IF signal from out-of-band signals. After that, a Square-Law Detector (SLD) provides an output that is proportional to the square of the IF envelope. In order to provide the time-average of the squared IF envelope, a Integrator is added to the circuit. Finally, the antenna temperature T_A can be derived by analyzing the output signal voltage.

For a given bandwidth $\Delta\nu$ and integration time τ , the temperature fluctuations detectable by the radiometer are characterized by the *ideal radiometer equation*

$$\sigma_{\text{TPR}} = \frac{T_{\text{sys}}}{\sqrt{\Delta\nu\tau}}, \quad (2.16)$$

using T_{sys} of Eq. (2.6). However, any electronic device is susceptible to variations in its physical properties, and the radiometer is no exception. In this sense, the sensitivity of the TPR can be described by the *practical radiometer equation*

$$\sigma_{\text{TPR}} = T_{\text{sys}} \left[\frac{1}{\Delta\nu\tau} + \left(\frac{\Delta G}{G} \right)^2 \right]^{1/2}, \quad (2.17)$$

where G is the system gain and ΔG is the *rms* (Root-Mean Squared) value of its fluctuating components. From Eq. (2.17) it is clearly seen that, if the square of the gain fluctuations is of a similar magnitude as $(\Delta\nu\tau)^{-1}$, the TPR sensitivity will be of the order of the system noise temperature. In such case, T_{sys} must be low enough to have excellent sensitivity, which indeed is never obtained in practice. So the gain fluctuations must be minimized as much as possible so as not to compromise the sensitivity only with T_{sys} .

It is well known that, theoretically, the TPR produces the best temperature sensitivity among all types of radiometers. Despite this wonderful feature, it is difficult to stabilize their gain fluctuations because of external temperature variations, power supply instability, variations on electrical properties of the devices, among others. Consequently, the instrument is quite difficult to calibrate, making the TPR unsuitable for many applications (Janssen, 1993).

Dicke Radiometer A practical solution to reduce gain fluctuation issues is to make periodic comparative measurements between a stable reference source whose temperature is similar to the antenna temperature, in such a way that the switching rate is higher than the highest frequency in the gain fluctuation spectrum (Ulaby and Long, 2014). This idea was originally proposed and implemented as a new instrument architecture by Dicke (1946), which is currently known as (yes, you guessed it!) the *Dicke radiometer*, shown in Fig. 2.6.

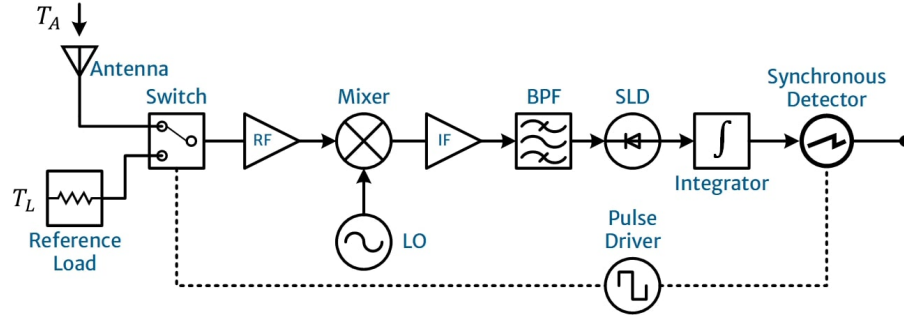


Fig. 2.6: Dicke radiometer architecture.

The Dicke radiometer (DR) is an improvement over the TPR, keeping practically the same topology of the TPR but incorporating a second signal input. In this case, a synchronized observation of the antenna and reference load signal is performed. The switching between sources is controlled by a Pulse Driver, which also synchronizes the output signal read-out with the Synchronous Detector. The switched measurements allow to decrease the contribution of the gain fluctuations to the sensitivity, as described below.

There are two implementation types for the DR, the unbalanced and balanced. The generalized case is known as *unbalanced* DR (UDR). If $T_A \neq T_L$, the UDR sensitivity is given by

$$\sigma_{\text{UDR}} = \left[\frac{(T_A + T_{\text{rx}})^2 + (T_L + T_{\text{rx}})^2}{\frac{1}{2}\Delta\nu\tau} \right]^{1/2}, \quad (2.18)$$

which is the idealized form for the UDR. Incorporating the gain fluctuations into Eq. (2.18), we obtain the practical form

$$\sigma_{\text{UDR}} = \left[\frac{(T_A + T_{\text{rx}})^2 + (T_L + T_{\text{rx}})^2}{\frac{1}{2}\Delta\nu\tau} + (T_A - T_L)^2 \left(\frac{\Delta G}{G} \right)^2 \right]^{1/2}. \quad (2.19)$$

On the other hand, when the reference load temperature is the same as the antenna temperature, i.e. $T_L = T_A$, the DR is said to be *balanced*. By taking this assumption, the idealized form of the *balanced* DR (BDR) can be derived from Eq. (2.18)

$$\sigma_{\text{BDR}} = \frac{T_A + T_{\text{rx}}}{\left(\frac{1}{2}\Delta\nu\tau \right)^{1/2}}, \quad (2.20)$$

which is two-times the ideal TPR sensitivity, described in Eq. (2.16). The factor-of-2 comes from dividing the net integration time by half because now, the source of interest is observed for half of time and because we are differentiating two random variables.

It is important to highlight that Eq. (2.20) express both the ideal and practical sensitivity of the balanced DR: if we replace $T_A = T_L$ in Eq. (2.19), we will obtain the same expression as Eq. (2.20).

From the last equations it can be seen that the sensitivity is lower than the TPR case. Although this technical improvement (particularly the BDR case) eliminates gain fluctuations, sensitivity decreases by a factor of two compared with the TPR case. Fortunately, there are a few other architectures that improve radiometer sensitivity, such as the correlation radiometer (Ulaby and Long, 2014), or the noise injection radiometer (Skou and Vine, 2006). However, all of them work on the principle of canceling the receiver noise contribution in a similar way as mentioned here. We will not address these topologies in this discussion but refer to Ulaby and Long (2014) for a detailed study of them.

Microwave Spectrometer The microwave spectrometer (MWS) is a special case of the radiometer which is used to resolve spectral features by measuring its power in narrow frequency ranges. The MWS results from dividing the spectral band of interest into a number of channels using the TPR topology in each channel (Janssen, 1993). The objective of the MWS is to measure the spectral components of a given signal. This is achieved by dividing the IF passband into as many elements as desired, and measure the amplitudes of each channel. Here we discuss two basic schemes of the MWS: a filter-bank and a tunable channel-based:

- (a) The filter-bank topology (see Fig. 2.7a) divides the IF passband using a Power Splitter and after that, a set of narrow-band filters, adjacent to one another, measure the spectral components simultaneously. The number of filters equals the number of frequency channels of the MWS. In principle, there is no upper limit to the number of frequency channels that can be used. This means that the instrument can cover the frequency band of interest with a very-high spectral resolution. However, the voluminous design of this idea represents a challenge for the costs and assembly of the instrument.
- (b) The tunable channel scheme (see Fig. 2.7b) performs a frequency sweep along the IF passband using a Tunable Local Oscillator (TLO) to provide the spectral elements. The sweep and the acquisition of the frequency channel is controlled by a Pulse Driver. So, the Synchronous Detector will give us the spectral elements in a serialized way. Compared to the filter-bank, this architecture is easy-to-implement and economically affordable. Nevertheless, it takes much longer to acquire the entire IF because the output signal is serially read.

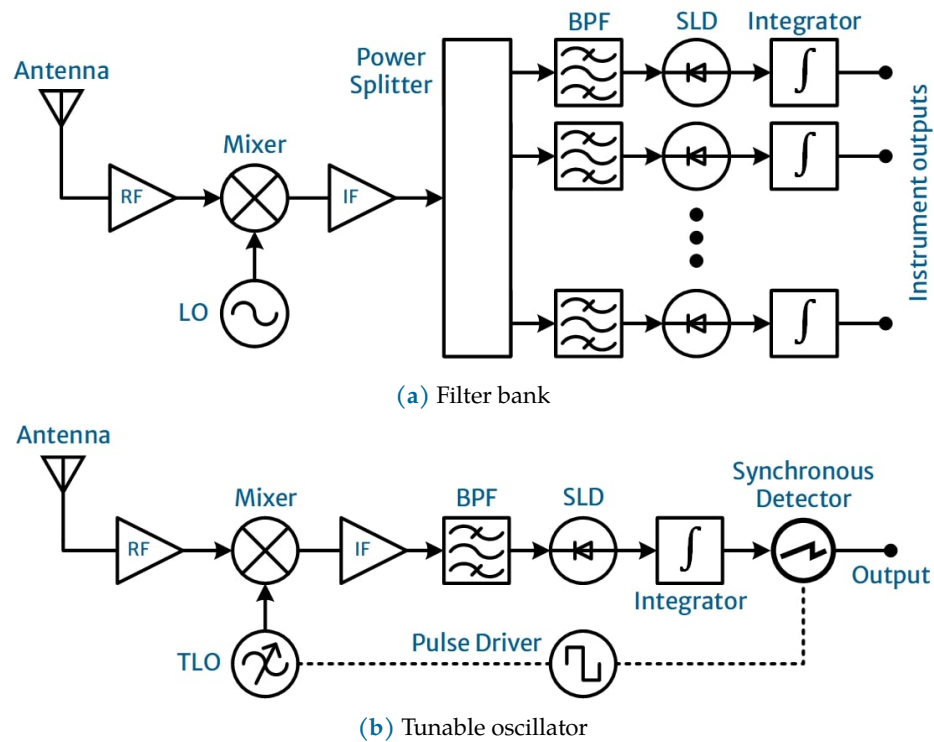


Fig. 2.7: Basic microwave spectrometer architectures.

We have explored some of the basic topologies for building a radiometer that could be useful for characterizing microwave water vapor lines, especially the 22 GHz line. To save costs, some scheme of switching radiometer tuned on or around the 22 GHz line could be used to obtain the average noise power in the band-pass of the instrument. If we are interested in reconstructing the line shape or being more precise in measuring the noise power, we had better use the microwave spectrometer topology. Regarding the goals of this work, the capability of shape reconstruction of the spectrometer represents a viable solution to characterize atmospheric water vapor in the K-band, so we are inclined towards this solution.

RADIOMETRIC DATA RETRIEVAL

A fundamental aspect of atmospheric measurements using microwave radiometers is the data retrieval, which refers to such methods and techniques that provide atmospheric variables based on the instrumental response. In this chapter, we introduce a general panorama of data retrieval in microwave radiometry, focusing on objectives and variables of interest for this work: the opacity and precipitable water vapor.

3.1 Retrieval theory

In remote sensing techniques there are two ways to obtain the sky parameters when an upward-looking atmospheric survey is performed: the **forward** and the **inverse** problems. They are the primary schemes on which the retrieval methods are based, and although they seem intuitive to solve, each one has its own implementation challenges (Karmakar, 2012).

3.1.1 The Forward Problem

The forward (or direct) problem is concerned with predicting the observed data or measurements given a set of physical parameters of the observed object or phenomenon (Ulaby and Long, 2014). Fig. 3.1 describes the forward problem: if the radiometer parameters (gain, receiver temperature, noise figure, etc.), the atmospheric variables (ground temperature, humidity, pressure gradients, etc.) and its boundary conditions are provided, the designer can directly implement a radiative transfer model to estimate the atmospheric brightness temperature with all the desired dependencies.

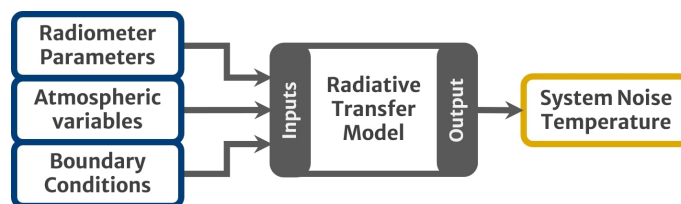


Fig. 3.1: The forward-problem process. Adapted from Ulaby and Long (2014).

3.1.2 The Inverse Problem

The inverse problem, on the other hand, is concerned with estimating the physical parameters of an object or phenomenon from the observed measurements. In another sense, it involves determining the underlying properties of the observed atmosphere that gave rise to the measured data (Janssen, 1993). As can be seen in Fig. 3.2, the radiometric observations of sky brightness temperature and *a priori* information about the site (altitude, weather conditions, time, etc) are given as input variables into an *inversion algorithm*, which tries to estimate the atmospheric variables (absorption coefficients, PWV, layer temperature, etc).

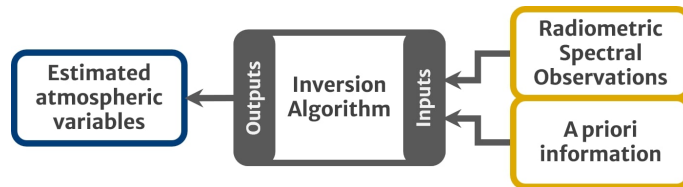


Fig. 3.2: The inverse-problem process. Adapted from Ulaby and Long (2014).

The forward problem requires a treatment in which most of the input variables are provided. In practice, these variables are measured at different atmospheric heights (possibly from outside the Earth) by *active remote sensing*, which is a technique that requires a feedback network of instruments for the atmospheric layer to be characterized. This means that the project costs increase significantly, making it economically unsuitable in most cases. In contrast, the inverse problem requires a single instrument on either side of the atmospheric layer instead of an instrument network, which means savings in the project's budget.

3.2 Microwave Radiative Transfer Equation

In the atmosphere, absorption attenuates incoming signals by the radiative transfer processes. If observers have a well-characterized atmospheric opacity, the solution of the radiative transfer equation can be directly implemented to provide the brightness temperature of the atmospheric emission measured by the radiometer. Before going to the formalism, let us clarify several considerations of this analysis:

- (a) The following analysis is performed in the Rayleigh-Jeans regime, since our interest are microwaves.
- (b) The scattering in the atmosphere is neglected because, as Janssen (1993) suggests, the total power involved in scattering is negligible compared with the power involved in absorption or emission processes.
- (c) The plane-parallel and stratified atmosphere model at lower heights is assumed since most of the absorption processes we are interested in happen in the troposphere, generally at $\lesssim 18$ km height (Kämpfer et al., 2013).
- (d) The geometry of the radiative transfer equation follows the ground-based observation scheme, where the top height of the layer is much smaller than the Earth's radii, as shown in Fig. 2.1 and Fig. 2.2.

The solution of the radiative transfer equation gives the brightness temperature of the atmospheric layer at the output T_{sky} , which is generated by the atmospheric emission, see [Condon and Ransom \(2016\)](#); [Janssen \(1993\)](#), and can be written as follows

$$T_{\text{sky}} = T_{b,0}e^{-\tau} + (1 - e^{-\tau})T_{\text{atm}} , \quad (3.1)$$

where $T_{b,0}$ is the input temperature of the atmospheric layer T_{atm} is the weighted-average temperature of the same layer. Eq. (3.1) is a more precise way to express the respective terms involved in Eq. (2.5). The exponential term in this equation is known as the *atmospheric transmission* \mathcal{T} , given by

$$\mathcal{T} = e^{-\tau} , \quad (3.2)$$

where τ is the total opacity due to the molecular species.

If we are only concerned about noise emission from the atmosphere, background radio sources can be neglected from T_{sky} by making observations at frequencies $\nu > 1$ GHz ([Condon and Ransom, 2016](#)). In this sense, we can assume that $T_{b,0} = T_{\text{cmb}}$, i.e, the cosmic microwave background radiation temperature. Hence, T_{sky} can be described by the following equation

$$T_{\text{sky}} = T_{\text{cmb}}e^{-\tau} + (1 - e^{-\tau})T_{\text{atm}} . \quad (3.3)$$

Eq. (3.3) is easily calculable because it is well-known that $T_{\text{cmb}} = 2.73$ K, and authors like [Thompson et al. \(2017\)](#) and [Ulaby and Long \(2014\)](#) suggest that a good-approximation of T_{atm} can be obtained from the ambient temperature T_{amb} , the atmospheric temperature lapse rate l , and the scale height of water vapor h_0 at the site, as follows:

$$T_{\text{atm}} = T_{\text{amb}} - lh_0 . \quad (3.4)$$

Using mean values of $l = 6.5$ K km⁻¹ and $h_0 = 2$ km we found that T_{atm} is smaller than T_{amb} by ~ 13 K. More precise studies on T_{atm} estimation can be found in [Han and Westwater \(2000\)](#), [Suparta et al. \(2007\)](#) or [Bevis et al. \(1992\)](#).

As anticipated, the radiative transfer equation in the microwave regime is the basic solution of the forward problem, and it is properly called the *forward model* in remote sensing. This model is easy-to-implement computationally, and is used in many atmospheric simulation codes¹. However, this is not the situation of most of real-life cases, since passive radiometry gives a direct measurement of T_{sky} instead of τ , which places us in the inverse problem.

3.3 Tip-Scan Method

Applying inversion algorithms, we introduce the so-called *Tipping curves* or *Tip-scan* method. The technique was originally proposed by [Dicke et al. \(1946\)](#), and it provides a direct way to obtain the atmospheric opacity derived from radiometric measurements without resorting to complex inversion algorithms, and surprisingly, it is derived from the forward model discussed above.

The working principle of tip curves is based on measuring T_{sys} as a function of air mass by scanning the atmosphere from the zenith to the horizon. We can take advantage of the

¹See the end of Section 1.1, where various algorithms are cited.

relation between the atmospheric opacity and the path length through the atmosphere, since this also varies with the air mass (Wilson et al., 2013).

First, the relation between the measured T_{sys} and T_{sky} has been addressed in Section 2.1, from which we get

$$T_{\text{sky}} = T_{\text{sys}} - T_{\text{rx}} , \quad (3.5)$$

since $T_{\text{sky}} \propto T_{\text{cmb}} + T_{\text{atm}}$. Then, we solve Eq. (3.3) for τ to obtain the generalized form

$$\tau = \ln \left(\frac{T_{\text{atm}} - T_{\text{cmb}}}{T_{\text{atm}} - T_{\text{sky}}} \right) . \quad (3.6)$$

On the other hand, if the opacity is low ($\tau \ll 1$), we can approximate the exponential term as $e^{-\tau} \approx 1 - \tau$. Hence, Eq. (3.3) can be expressed as

$$T_{\text{sky}} \approx (1 - \tau)T_{\text{cmb}} + (\tau)T_{\text{atm}} . \quad (3.7)$$

Solving Eq. (3.7) for τ , we obtain a nearly linear relation between T_{sky} and the zenith opacity

$$\tau \approx \frac{T_{\text{sky}} - T_{\text{cmb}}}{T_{\text{atm}} - T_{\text{cmb}}} . \quad (3.8)$$

Additionally, the total opacity as a function of zenith angle is given by

$$\tau = \tau_0 \sec z , \quad (3.9)$$

where τ_0 is the zenith opacity along the line-of-sight. This allows to rewrite Eq. (3.6) and Eq. (3.8) as

$$\tau_0 = \ln \left(\frac{T_{\text{atm}} - T_{\text{cmb}}}{T_{\text{atm}} - T_{\text{sky}}} \right) \left(\frac{1}{\sec z} \right) , \quad (3.10)$$

$$\tau_0 \approx \left(\frac{T_{\text{sky}} - T_{\text{cmb}}}{T_{\text{atm}} - T_{\text{cmb}}} \right) \left(\frac{1}{\sec z} \right) , \quad (3.11)$$

respectively. Note that we can express the trigonometric term of this set of equations as the air mass X^{-1} (see Eq. (2.2)).

By varying the zenith angle and measuring the respective T_{sys} , we will obtain the zenith opacity τ_0 by analyzing the slope of the curve. This is a process known as *doing a tip curve*. For example, suppose we have a receiver noise temperature $T_{\text{rx}} = 80$ K, and an atmospheric mean temperature of $T_{\text{atm}} = 277$ K (corresponding to $T_{\text{amb}} = 290$ K). In addition, let us perform a scan for air masses of $1 \leq X \lesssim 3$ for zenith opacity values of $\tau_0 = 0.1, 0.3, 0.5, 0.7, 1.0$, and plot T_{sys} from Eq. (3.8) using Script B.1. We will obtain the tip curves shown in Fig. 3.3.

Although opacities have been provided in the previous exercise, in practice these values are not given by the user. However, we have control over the air mass variation and the T_{sys} measurement, so it will be sufficient to analyze the resulting tip curve. Given the procedure, and linking Eq. (3.5) with Eq. (3.10) it is obvious that $T_{\text{sys}}(z)$, so what remains, is to graphically calculate the slope m from lines such as those shown in Fig. 3.3. Thus, the zenith opacity can be calculated as

$$\tau_0 = \frac{m}{T_{\text{atm}}} , \quad (3.12)$$

where m is given in Kelvin, and we have finally found the relationship between radiometric measurements and atmospheric opacity.

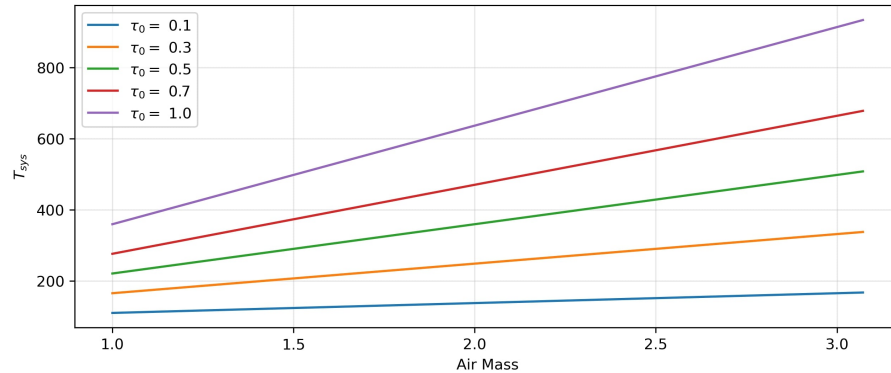


Fig. 3.3: System noise temperature as a function of air mass.

Tip-scan helps to estimate the atmospheric opacity in a certain frequency band. Evidently, we should have a calibrated instrument to enhance the opacity calculations with the minimum uncertainty. Thus, it is important to perform a calibration procedure, as mentioned in Section 2.2, before the observations. Moreover, [Hiriart and Rojas \(2023\)](#) suggests that once the radiometric measurements are done, the tip-curve's offset must be corrected to ensure the coincidence of all the curves in $T_{\text{sys}}(X = 0) = T_{\text{cmb}} + T_{\text{rx}}$ in our case.

3.4 Precipitable Water Vapor Retrieval

Precipitable water vapor (PWV) is a measure of the total amount of water vapor molecules in the atmosphere. PWV represents the water vapor content in a vertical column measured from the surface to the top of the atmospheric layer of interest. ([Burke et al., 2019](#)). As we have mentioned in Section 1.2, water molecules can absorb energy at certain specific microwave frequencies when light travels through the atmosphere, resulting in an attenuation or loss of line intensity. This loss is characterized by the zenith opacity we discussed in Section 3.3. The atmospheric water vapor content is directly related to this absorption: the more water vapor in the atmosphere, the greater the attenuation of microwaves, i.e., they are directly proportional quantities ([Ulaby and Long, 2014](#)).

In radio astronomy applications, PWV is strongly related to the atmospheric attenuation and the path length delay ([Thompson et al., 2017](#)). This quantity is referred to as an additional measure of the quality of the sky at a given frequency band, in the short and long term. The most common way to estimate the PWV at the observing site consists of performing a retrieval algorithm from radiometric measurements, being supported by atmospheric simulations ([Wilson et al., 2013](#)).

In the following, we present a procedure to estimate the PWV from tipping measurements of opacity. We rely on atmospheric simulations to get the zenith opacity by varying the relative humidity using an *atmosphere* algorithm. We find a set of equations which relates the input relative humidity at the site with the zenith PWV and opacity.

Following [Thompson et al. \(2017\)](#), we assume a linear relation between the zenith opacity and the PWV as

$$\tau_0 = \alpha_v PWV + \tau_{\text{dry}}, \quad (3.13)$$

where α_v is the absorption coefficient of water vapor (given in mm^{-1}), and τ_{dry} (dimensionless) is the zenith dry opacity (atmosphere in absence of liquid water), which depends on frequency, site elevation and weather conditions ([Janssen, 1993](#)). Since we are interested in PWV, we express Eq. (3.13) as

$$PWV = \frac{1}{\alpha_v} \tau_0 - \frac{\tau_{\text{dry}}}{\alpha_v}. \quad (3.14)$$

As suggested by [Marvil \(2010\)](#), it is necessary to simulate the atmosphere, analyze the data, and compile the respective variables to find the constants of Eq. (3.14). We use *atmosphere* for simulations via the Script B.2, which calculates the zenith opacity and PWV for a given relative humidity value at a single frequency (22.235 GHz). The simulated site has similar weather and geographical conditions as the VLA observatory (see Appendix A). The simulations run for relative humidity values from 10% to 100%, which gives different values of τ_0 and *PWV*, listed in Table 3.1.

Table 3.1: Resulting *PWV* and zenith opacity from simulations at 22.235 GHz.

<i>RH</i> [%]	<i>PWV</i> [mm]	τ_0	<i>RH</i> [%]	<i>PWV</i> [mm]	τ_0
10	0.78	0.016517	60	4.68	0.047567
20	1.56	0.022771	70	5.46	0.053712
30	2.34	0.029002	80	6.23	0.059836
40	3.12	0.035212	90	7.01	0.065938
50	3.90	0.041400	100	7.78	0.072020

We plot $PWV(\tau_0)$ and $\tau_0(RH)$, obtaining the lines shown in Fig. 3.4.

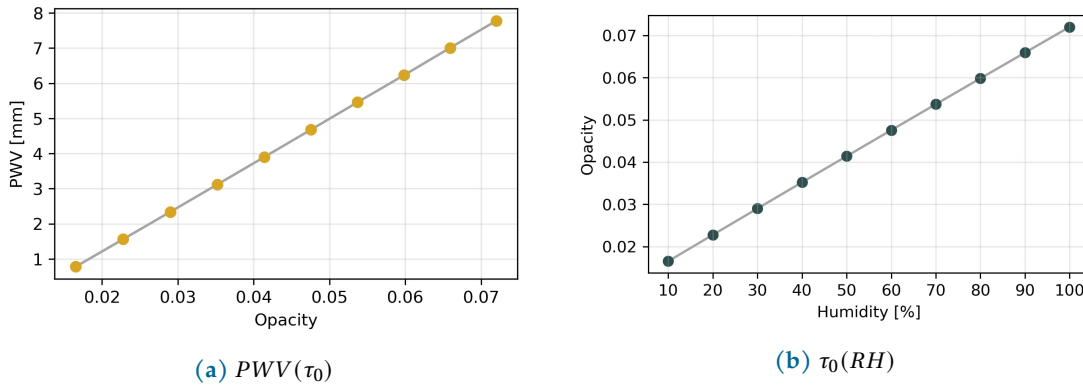


Fig. 3.4: Linear relations between *PWV*, zenith opacity and relative humidity.

The slope of the line and the offset in Fig. 3.4a can be described analytically with Eq. (3.12). We found that the factors $\alpha_v^{-1} = 126.1859 \text{ mm}$ and $\tau_{\text{dry}}\alpha_v^{-1} = 1.3163 \text{ mm}$, allow us to rewrite Eq. (3.12) as

$$\boxed{\frac{PWV}{1 \text{ mm}} = 126.1859\tau_0 - 1.3163}. \quad (3.15)$$

Consequently, $\alpha_v = 7.9248 \times 10^{-3} \text{ mm}^{-1}$ and $\tau_{\text{dry}} = 1.0431 \times 10^{-2}$. Additionally, the zenith opacity can be described as a function of relative humidity by analyzing the line of Fig. 3.4b. So that, we write $\tau_0(RH)$ as

$$\tau_0 = 6.1668 \times 10^{-4} RH + 1.0479 \times 10^{-2} . \quad (3.16)$$

Hence, the relation between precipitable water vapor and the relative humidity can be found by combining Eq. (3.15) and Eq. (3.16). Thus,

$$\frac{PWV}{1 \text{ mm}} = 7.7816 \times 10^{-2} RH + 6 \times 10^{-3} . \quad (3.17)$$

Another approach is to derive the PWV from brightness temperature measurements as suggested by [Hiriart and Rojas \(2023\)](#). The authors use a pair of measured brightness temperatures (T_b) at different (but quite close) frequencies near the 22-GHz water vapor line to distinguish the contribution of liquid water to the continuum. The method is also based on atmospheric simulations to derive the linear relation between PWV and T_b , but they find two different relations for each selected frequency. The authors mentioned that although this method is applicable to calculate PWV at a single frequency, the main intention of their work is to estimate the path delay due to water vapor that concerns interferometric observatories.

It is worth mentioning that, since these methods are based on atmospheric simulations, it will be necessary to calibrate the equations periodically using real measurements. This can be done by running atmospheric simulations with climatic conditions as close as possible to reality, then correcting the factors of the above equations. In addition, the relations presented above only describe variables at 22.235 GHz, so simulations must be run at different frequencies to find the respective equations ([Marvil, 2010](#)). However, there are many different ways to retrieve PWV from opacity measurements, see e.g. methods presented in [Kämpfer et al. \(2013\)](#); [Karmakar \(2014\)](#); [Wiederhold \(1997\)](#).

Summarizing the last three chapters, the presence of water vapor in the Earth's atmosphere and its thermodynamic process directly affects radio astronomy observations. By measuring and characterizing the water vapor content, the atmospheric corrections can be estimated. The microwave radiometer helps to make this process possible by implementing many radiometric techniques. In addition, the current technology provides improved features to this instrument, increasing its reliability in measurements.

CHAPTER 4

RADIOMETER DESIGN

We have finally reached the most critical sections of this thesis. From this chapter onwards, we will address the technical aspect of this work, from design to implementation, and discussing the development, design criteria and construction of the radiometer. The development of this thesis revolves around the conversion of a generic K-band radio frequency receiver, provided by HartRAO, to a water vapor radiometer using high-performance electronics and state-of-the-art digital systems.

The design and experimentation was done at the Radio Astronomy Instrumentation Laboratory (LIRA) of the Institute of Radio Astronomy and Astrophysics (IRyA), which provided equipment for testing and characterization, modern computer systems, as well as substantial electronic and mechanical supplies.

4.1 Conceptual Design

The fundamental radiometer design consists of three main stages: the K-band radio frequency receiver, a down-conversion stage, and the digitization system (see Fig. 4.1). The receiver is a generic RF receiver for K-Band with both Right-Hand and Left-Hand Circular Polarization (RCP and LCP, respectively) channels. The down-conversion stage is a single heterodyne arrangement with IF amplification and the digitization system is based on a *Radio Frequency System-on-Chip* (RFSoc) board for data-acquisition and signal processing. These stages will be described in detail throughout this chapter.

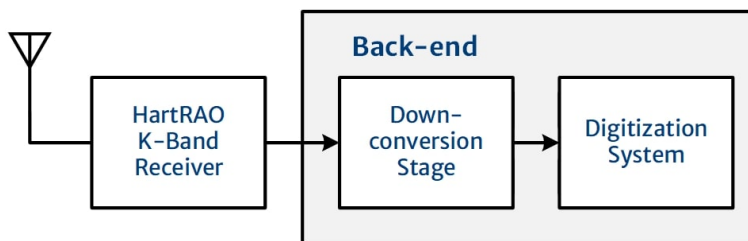


Fig. 4.1: Conceptual design of the K-band water vapor radiometer. We will focus on the design and testing of the back-end stage.

The concept shown in Fig. 4.1 and particularly the back-end, was proposed in response to two important questions:

1. What spectral resolution must the radiometer have in order to reconstruct the shape of the water vapor emission line properly?
2. Considering available technology, budget limitations and resolution parameters, what type of down-conversion and detection techniques should be implemented?

The first point refers to the integration time of the radiometer, which is an important factor to determine the signal-to-noise ratio attainable by the instrument. Regarding to second question, it refers to the spectral channels that the instrument must have to characterize the water vapor emission line. Both criteria were selected in such a way that none compromised the sensitivity of the radiometer. Finally, the third point helped to select the back-end hardware, and technique for data acquisition and processing.

4.1.1 HartRAO Receiver

The first stage of the radiometer is a dual-channel, single down-conversion superheterodyne receiver (hereafter KRx). The device operates at the K-band, centered at 22.5 GHz (see Fig. 4.2). It was designed and built by the technical staff of HartRAO, and subsequently tested and characterized by [Stander \(2021\)](#) at Carl and Emily Fuchs Institute for Microelectronics (CEFIM) of University of Pretoria, South Africa. The receiver is currently in the academic possession of the IRyA in our laboratory.

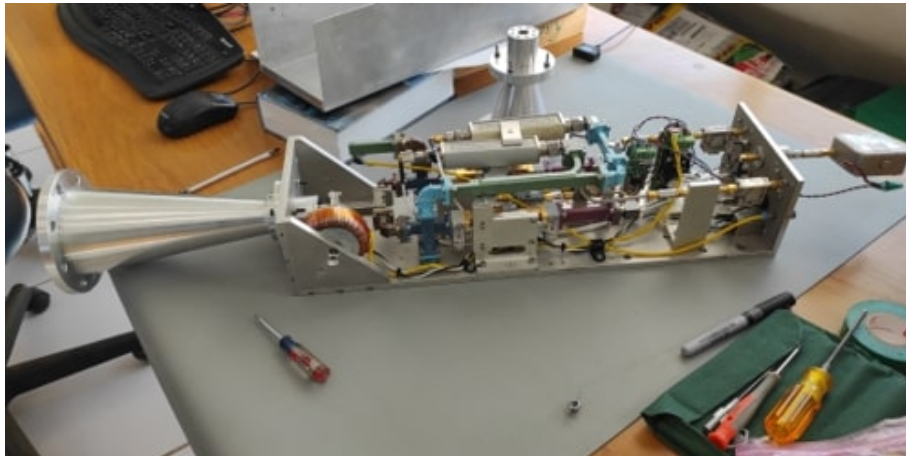


Fig. 4.2: Uncovered HartRAO K-band receiver at LIRA.

The architecture allows the simultaneous detection of both RCP and LCP signals, as shown in Fig. 4.3. Both channels share the same local oscillator (LO) signal at the heterodyne stage. Additionally, an external clock source is connected to be used as the reference clock for the LO. See Table 4.1 to consult the main features of this instrument.

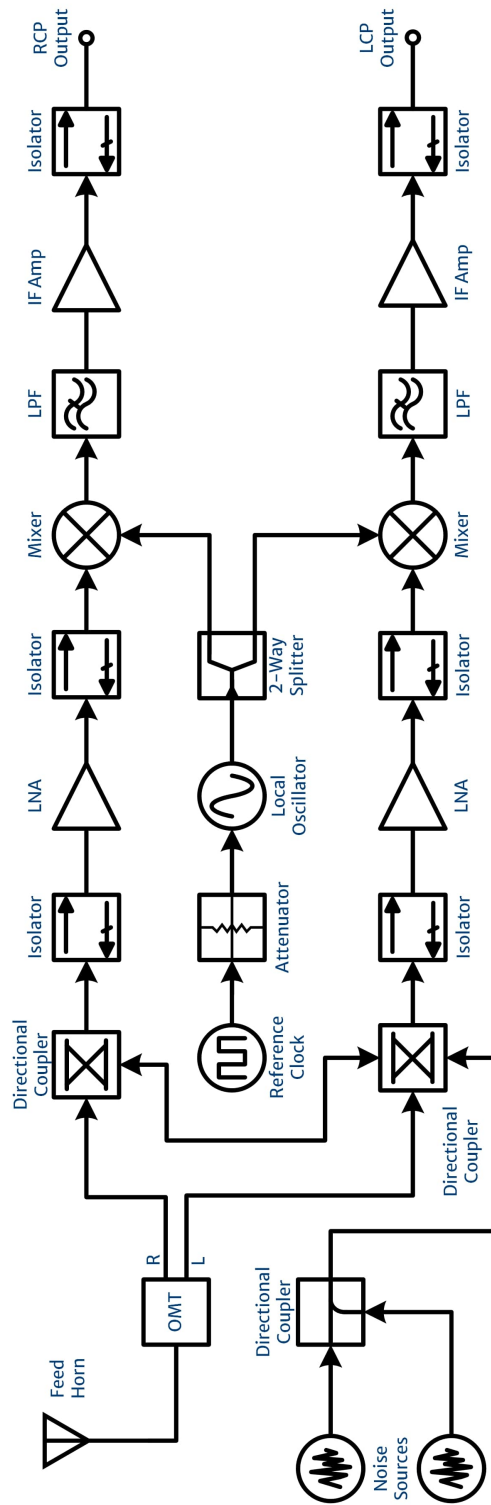


Fig. 4.3: Schematics of HartRAO receiver. Adapted from Stander (2021).

Table 4.1: Technical specifications of HartRAO receiver (Stander, 2021).

Feature	Value	Units
RF band	20.5 - 24.5	GHz
LO frequency	17.4	GHz
IF band	3.1 - 7.1	GHz
Noise Sources ENR	14.5	dB
RCP channel gain (peak)	43	dB
LCP channel gain (peak)	47	dB
RCP channel T_{rx} (@ 22.235 GHz)	~ 280	K
LCP channel T_{rx} (@ 22.235 GHz)	~ 260	K

The LCP and RCP output characteristics are the basis for designing the subsequent stages of the instrument described in the following sections. However, we arbitrarily take the RCP channel to acquire the signal: either channel can be taken for practical measurements.

4.1.2 Instrumental Integration Time and Spectral Resolution

The integration time and spectral resolution are two primordial features of a radiometer which help to plan the observations. For the instrument design, it is important to analyze these features to have an entry scenario of the instrument capabilities. Here we discuss the selection of these features to determine the architecture of the radiometer.

The radiometer consists of a heterodyne receiver which gets the signal from the sky. This signal arrives with noise from both artificial and natural sources. It is crucial to have a prominent peak of the signal or low-noise floor in order to distinguish the signal from this noise. This can be achieved by increasing the integration time τ which, consequently, increases the **Signal-to-Noise Ratio** (SNR) of the system. In a radiometer system, the SNR is given by:

$$\text{SNR} = \frac{T_A}{\sigma_T}, \quad (4.1)$$

where T_A is the antenna temperature and σ_T is the instrumental sensitivity (Marr et al., 2016). Basically, σ_T is given by the ideal radiometer equation,

$$\sigma_T = \frac{T_{\text{sys}}}{\sqrt{\Delta\nu\tau_{\text{obs}}}}, \quad (4.2)$$

where T_{sys} (defined in Eq. (3.5)) is the system noise temperature and $\Delta\nu$ is the observing bandwidth. As described in Section 2.1, T_{sys} is made up of different contributions of which we have neglected several. In the case discussed below, we suppose that T_{sys} is completely dominated by the receiver temperature.

Since we are interested in the atmospheric emission temperature T_{sky} (see Eq. (3.1)) instead of the antenna temperature (conceptually used for a source external to the atmosphere), we can replace $T_A \equiv T_{\text{sky}}$. In this sense, and combining (4.2) and (4.1) we get,

$$\boxed{\text{SNR} = \frac{T_{\text{sky}}}{T_{\text{sys}}} \sqrt{\Delta\nu\tau_{\text{obs}}}}, \quad (4.3)$$

which gives us the well-known result from the radiometer equation that the signal-to-noise ratio improves as the factor $(\Delta\nu\tau)^{1/2}$ increases. For purposes of the current experiment, it is helpful to describe the integration time as a function of SNR, since τ_{obs} is the only controllable variable during the scanning process. Hence,

$$\tau_{\text{obs}} = \frac{1}{\Delta\nu} \left(\frac{T_{\text{sys}}}{T_{\text{sky}}} \text{SNR} \right)^2. \quad (4.4)$$

The experiment described in this section executes Eq. (4.4) via a *Python* routine for given values of system noise, antenna temperature and SNR. We execute the Script B.3 in Appendix B under the following considerations:

- (a) The receiver temperature was chosen using values reported by [Stander \(2021\)](#). Between 21-24 GHz, we estimate a mean value of $T_{\text{rx}} = 275$ K in the RCP and LCP channels (see Fig. 4.4).
- (b) The sky brightness temperature due to water vapor at 22 GHz is estimated by performing an *atmosphere* tool routine¹. Executing the Script B.4 in Appendix B, we get $T_{\text{sky}} \sim 9.5$ K for winter season conditions similar to the Karl G. Jansky Very Large Array (VLA) site.
- (c) We evaluate Eq. (4.4) for signal-to-noise ratios of 10, 100 and 1000.
- (d) We arbitrarily select bandwidths of 50, 100, 250 and 500 MHz.

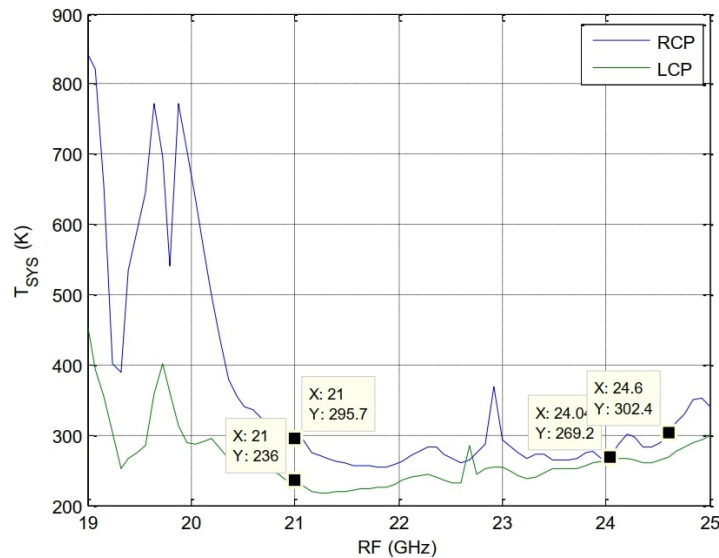


Fig. 4.4: Receiver noise temperature of KRx around 22 GHz. Taken from [Stander \(2021\)](#).

¹See Appendix A for information about CASA's *atmosphere*.

As a result, we obtained the slopes shown in Fig. 4.5.

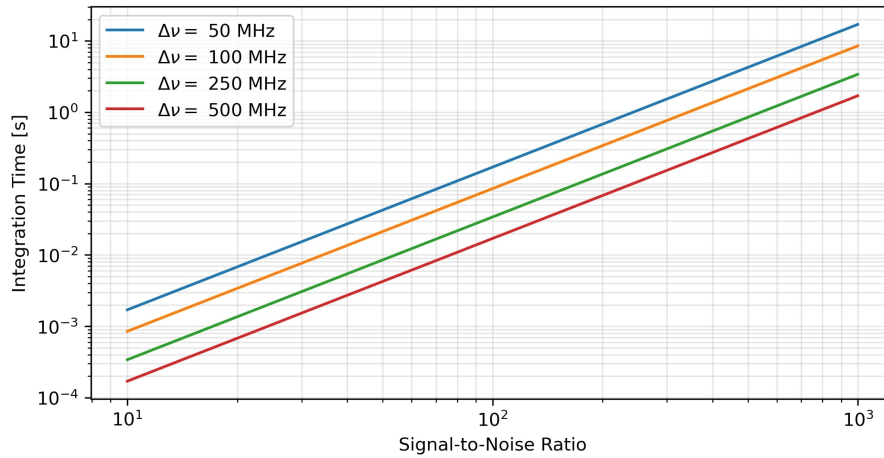


Fig. 4.5: Integration time as function of SNR. As bandwidth decreases (i.e. better resolution), it takes more integration time to reach a certain SNR.

This exercise helps to find the integration time we need to reach a certain SNR for a single observation point. Regarding the Tip-Scan procedure we discussed in Section 3.3, we will need more than a single point to characterize the atmospheric opacity, and consequently the PWV. It is recommended to have at least three measured T_{sys} points to characterize the slope of the tip-curve. This means that we will take three times the observation time to scan three different elevation angles. Let us summarize the results of Fig. 4.5 in Table 4.2 to have an idea of how long it will take to observe a single zenith angle.

Table 4.2: Integration time for given bandwidth and SNR.

Bandwidth ($\Delta\nu$)	Integration time (τ_{obs}) ⁺		
	SNR = 10	SNR = 100	SNR = 1000
50 MHz	1.7 ms	170 ms	17 s
100 MHz	0.85 ms	85 ms	8.5 s
250 MHz	0.34 ms	34 ms	3.4 s
500 MHz	0.17 ms	17 ms	1.7 s

⁺ For $T_{\text{sky}} = 9.5$ K and $T_{\text{sys}} = 277.73$ K

Inspecting the values in the table, we can conclude that:

- For a bandwidth of 50 MHz, the task of reaching an SNR = 1000 would take a quarter of a minute for a single elevation angle. Supposing we perform a tip-scan with the three minimal measuring points using a digital spectrometer, the total observation time will take 51 seconds (three elevation angles of 17 seconds each). In the case of a tunable oscillator radiometer with four spectral channels, the total observation time will increase to 3.4 minutes because the spectral channels are acquired sequentially. In other words,

17 seconds per four channels and three elevation angles equals to 204 seconds. In practice, a radiometer takes more than three elevation angles. So that the net integration time will increase as we increase the number of scan angles. This situation could be unacceptable if the timescales of atmospheric variations are shorter than the net integration time. A similar problem presents itself in the case of more channels with a tunable oscillator.

- ▶ For a bandwidth of 500 MHz, we reach a SNR of 1000 in only 1.7 seconds. In the scheme of the digital spectrometer, the total integration time will be 5.1 seconds, whereas the tunable oscillator topology will take 20.4 seconds total. Evidently, the integration time decreases ten times due to factor-of-10 increase in the bandwidth. Although this bandwidth allows for excellent SNR at acceptable timescales, we will be limited to characterizing the KRx bandwidth in only eight spectral channels since the IF is 4 GHz wide.
- ▶ Suppose that we want to achieve an SNR = 100 (which is an acceptable ratio in practice). The total observation time for a 50 MHz digital spectrometer under the same conditions as in the two preceding cases, will take only a half of a second, whereas the tunable oscillator radiometer will take two seconds. On the other hand, a 500 MHz resolution will achieve this SNR in only 51 seconds, and the tunable oscillator scheme will take 3.4 minutes. This keeps us in a middle ground between the two bandwidths mentioned above, where atmospheric and instrumental resolution repercussions could be avoided.

As can be seen, the 50 MHz and 500 MHz channels do not present a viable combination of integration time and spectral resolution: on the one hand we will reach the limits of water vapor time stability (Zeballos et al., 2016; Ferrusca et al., 2022; Hogg et al., 1981; Otárola et al., 2019) and on the other hand we will lose spectral resolution. Hence, we will consider only intermediate values between 100 and 250 MHz, bearing in mind that the narrower the bandwidth, the worse the sensitivity of the instrument. These bandwidths will be reasonable for the radiometer design, and probably represent the best combination of integration time and spectral resolution. This situation is taken as a starting point for the conceptual design of the instrument to be discussed in more detail in Section 4.3.

4.1.3 Required Spectral Resolution

The radiometer estimates the sky brightness temperature at the water vapor line by measuring the spectral power of the signal. Since the line brightness cannot be obtained for every single frequency instrumentally, it must be sampled at finite frequency intervals. Consequently, the radiometer should have a filtering stage to measure the line intensity at a certain spectral interval. Thus, a minimal spectral resolution to accurately determine the line profile must be established.

Summarizing this experiment, the brightness temperature and opacity due to water vapor around 22 GHz were simulated using the *atmosphere* tool. Then, we divided the frequency window of the brightness temperature model, simulating various channel numbers of the instrument, to fit a representative equation. Finally, we compared the fitted data against the respective model values to evaluate the goodness-of-fit. The statistics will give us an idea of how many frequency channels will be necessary to recreate the water vapor profile.

The brightness temperature and opacity profiles were calculated within the RF operative band of the KRx (see Table 4.1). We execute the Script B.4 (see Appendix B), which generates the profile and stores the data into a text file. The models are shown in Fig. 4.6.

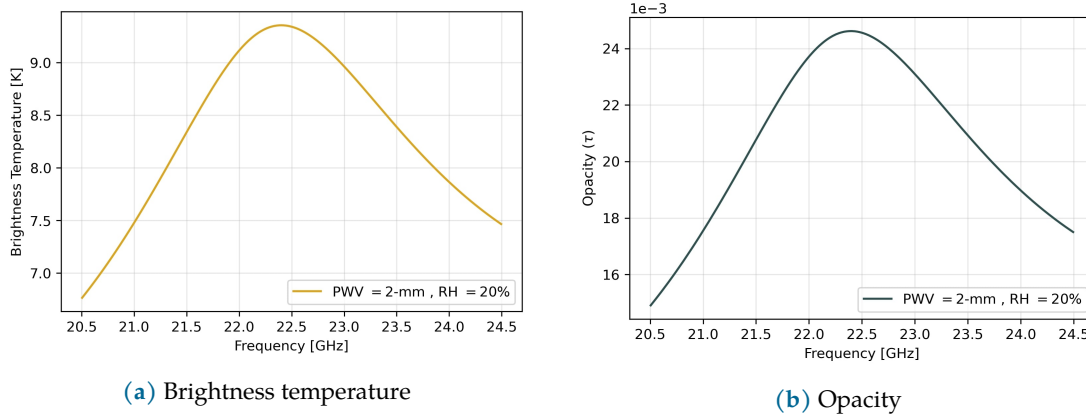


Fig. 4.6: Simulated profiles around water vapor line at 22.235 GHz.

Only the temperature profile above was used for this experiment. This profile consists of 10,000 rows of data, i.e., the algorithm solves the brightness temperature for 10,000 frequencies within the defined window using a frequency step of $f_R = 400$ kHz. In order to simulate the channels of the radiometer, the data was divided into groups of n elements, so the resulting spectral window was reduced to just

$$N = \frac{10,000}{n} \quad (4.5)$$

rows of data, where N represents the number of channels. In addition, the resulting bandwidth per channel Δv_{ch} is given by:

$$\Delta v_{ch} = \frac{\Delta v_{RF}}{N}, \quad (4.6)$$

where $\Delta v_{RF} = 4$ GHz (see Table 4.1) is the width of the RF window. This new data consists of the mean frequency (which actually refers to the center frequency of the channel) and mean temperature of each group, arranged in a new text file. This process was repeated seven times, simulating models of different n values using Script B.5. The resulting N and Δv_{ch} for each model are shown in Table 4.3.

Table 4.3: Group size, data rows and bandwidth per channel of calculated models.

Model	n	N	Δv_{ch}	Model	n	N	Δv_{ch}
a	1	10,000	400 kHz	e	1,250	8	500 MHz
b	10	1,000	4 MHz	f	1,666	6	666 MHz
c	100	100	40 MHz	g	2,500	4	1.0 GHz
d	1,000	10	400 MHz	—	—	—	—

Then, we fit a curve to each model by using the *Curve Fitter Toolbox* (CFT) provided by Matlab®. Using the shape of the collision-broadening spectral lines (Cernicharo, 2014), and

the water vapor continuum, which is proportional to v^2 (Rosenkranz, 1998), we fit a Gaussian profile plus a second-order polynomial using CFT. So, the input equation represents the brightness temperature as a function of the frequency such that,

$$T_B(v) \approx A \exp \left[- \left(\frac{v - 22.235}{c_0} \right)^2 \right] + c_1 v^2 + c_2, \quad (4.7)$$

where A , c_0 , c_1 , c_2 are coefficients estimated by CFT. As the reader may notice:

- We use a Gaussian instead of a *van Vleck-Weisskopf* profile for simplicity. It should be remembered that the difference between these profiles lies mainly in the wings and we must have a high-resolution instrument to distinguish between both profiles. This situation is outside the design considerations.
- There is not a first order polynomial term in Eq. (4.7) since it does not describe the nature of the water vapor continuum at the centimeter band (Rosenkranz, 1998).

After running CFT, we listed the obtained coefficients in Table 4.4.

Table 4.4: Estimated coefficients of fitted models.

Model	Fitted	A	c_0	c_1	c_2
a	a*	3.0190	1.6285	8.3×10^{-3}	2.1697
b	b*	3.0130	1.6285	8.3×10^{-3}	2.1696
c	c*	3.0130	1.6287	8.3×10^{-3}	2.1692
d	d*	3.0144	1.6436	8.3×10^{-3}	2.1367
e	e*	3.0166	1.6526	8.3×10^{-3}	2.1163
f	f*	3.0262	1.6738	8.4×10^{-3}	2.0651
g	g*	3.0870	1.5625	8.4×10^{-3}	2.1377

Finally, we compiled the *Root Mean Squared Error* (RMSE (Matlab, 2022)) the reduced chi-square ($\tilde{\chi}^2$) values into Matlab's workbench to evaluate the goodness-of-fit. Table 4.5 shows the statistics: the closer the *RMSE* is to zero and the smaller the $\tilde{\chi}^2$, the better the fit.

Table 4.5: Statistics of fitted models.

Fitted	N	<i>RMSE</i>	$\tilde{\chi}^2$	Fitted	N	<i>RMSE</i>	$\tilde{\chi}^2$
a*	10,000	0.05545	4.6752×10^{-4}	e*	8	0.06830	5.8049×10^{-4}
b*	1,000	0.05555	4.6902×10^{-4}	f*	6	0.07386	8.9650×10^{-4}
c*	100	0.05653	4.8451×10^{-4}	g*	4	0.12751	1.8333×10^{-3}
d*	10	0.06570	5.5616×10^{-4}	—	—	—	—

Fig. 4.7 shows a comparison between the previously obtained models and the simulated brightness temperature profile.

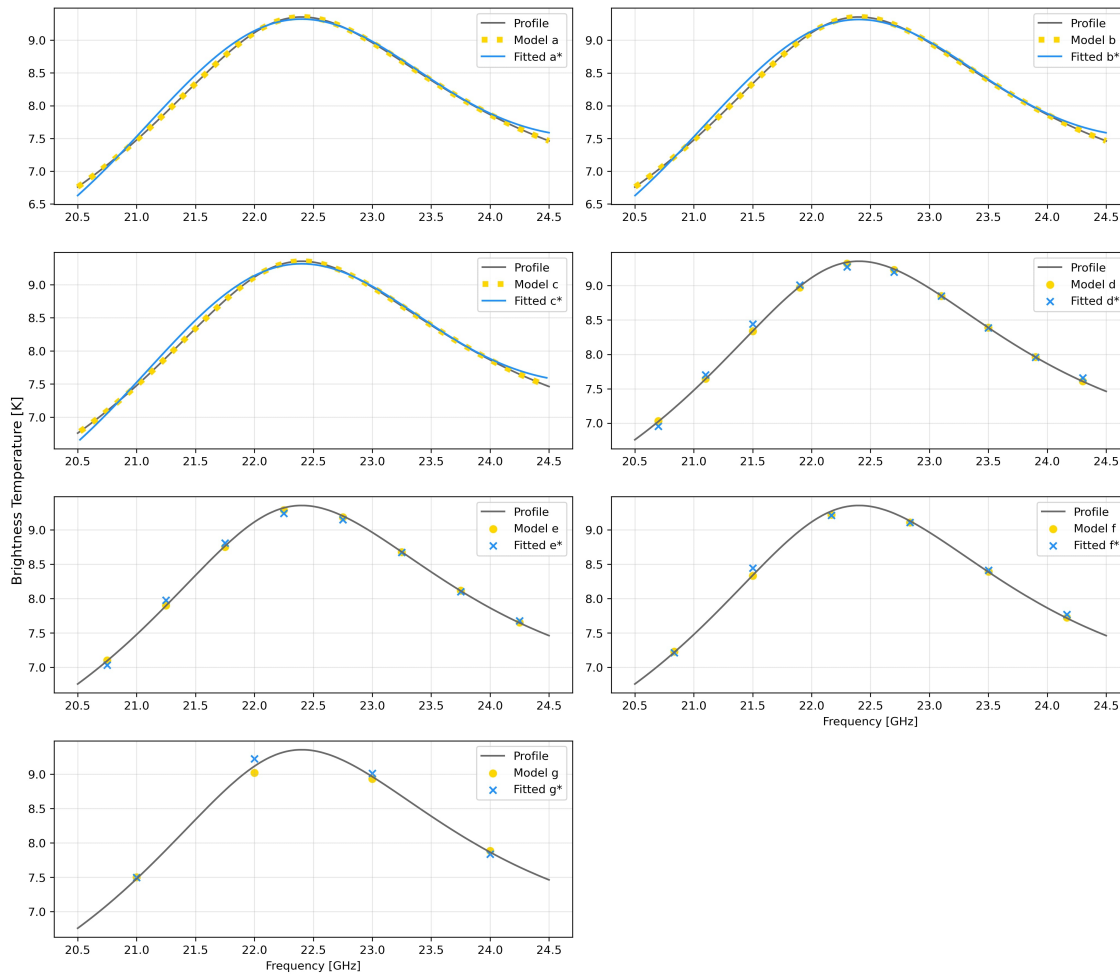


Fig. 4.7: Brightness temperature models and their respective fitted models compared to the theoretical profile.

Moving away from the profile reconstruction, we also evaluate the standard deviation between the simulated profile from Fig. 4.6a and the reduced models listed in Table 4.3. The RMSE between the profile and the models (before fitting) complement the results in Table 4.5 to finally choose the ideal number of channels. This step was done by computing the RMSE between the Model a (reference model) and the rest of the models into Matlab’s workbench. We added three extra models of 16, 32 and 64, channels (x_1 , x_2 and x_3 respectively) to the experiment to review the trend of the RMSE. The results are listed in Table 4.6.

Table 4.6: RMSE between models. Note that the $RMSE = 0$ in the ‘a - a’ row, since the model is compared to itself.

Comparison	N	$RMSE$	Comparison	N	$RMSE$
a - g	4	5.2286×10^{-2}	a - x_2	32	8.72×10^{-4}
a - f	6	2.4691×10^{-2}	a - x_3	64	2.26×10^{-4}
a - e	8	1.3797×10^{-2}	a - c	100	1.04×10^{-4}
a - d	10	8.8490×10^{-3}	a - b	1,000	5.2057×10^{-5}
a - x_1	16	3.4520×10^{-3}	a - a	10,000	0

The trend of Table 4.6 is plotted in Fig. 4.8. As can be seen, the standard deviation of the water vapor brightness temperature improves as we increase the number of channels and it gets worse as soon as we decrease the number of channels.

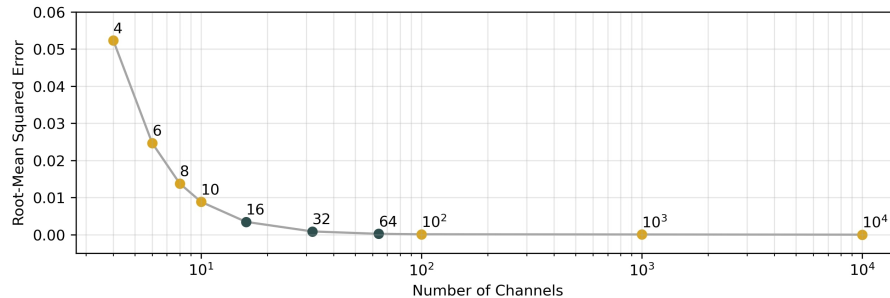


Fig. 4.8: RMSE between models as a function of number of channels.

Supposing that we are looking for an analog design, and according to Table 4.5, the high-order channel models ($N \geq 10^2$) have the best statistical features. However, they are not very affordable, since they require a voluminous design and the purchasing of many devices. Those of 10 and 8-channels have similar RMSE and χ^2 values: slightly worse than the aforementioned models but better than the 6 and 4-channel models. Regarding the latter two, although they show a low quality of fit, they may represent a budget saving for an analog design.

If we are looking to build a digital spectrometer, any of the models can be an option without hurting the budget. Nevertheless, it should be taken into account that high-order channel models may exceed the digital capabilities of the platform we use. On the other hand, having few channels results in a loss of fidelity in the profile reconstruction, since the average temperature measured in each channel probably differs from the theoretical profile, as shown in Fig. 4.7.

In addition, from Fig. 4.8 it can be seen that the deviation becomes minimal from the 10²-channel model to the densest, and increases exponentially for fewer than 10 channels. Taking this into consideration, the ideal number of channels lies between these values. Thus, we will avoid both the low-quality of fit for low-channel numbers and the high-cost of a high-channel number instrument. The selected number of channels is addressed in Section 4.3.4 where we relate it to the spectrometer implementation.

4.2 Back-end Stage

The back end of the radiometer is composed of two stages, as shown in Fig. 4.1 at the beginning of this chapter. It consists of an analog *down-conversion* circuit, and the *digitization system*. Following the conclusions of Sections 4.1.2 and 4.1.3, we propose three possible designs for the back-end: an analog filter bank, a tunable oscillator, and a digital spectrometer-based architecture. In this section, the features, capabilities, and design considerations of the three architectures are discussed. It should be noted that the following topologies presume the features of KRx presented in Table 4.1.

4.2.1 Analog Filter Bank

A filter bank is a classic design for measuring spectral power across a given frequency band. This back-end proposal is shown in Fig. 4.9, and for practical purposes, we add additional stages in the basic architecture. This architecture consists of a 16-channel filter bank in a 4 GHz intermediate frequency bandwidth. A Single-Board Computer (SBC) is implemented to acquire, process and store the measurements.

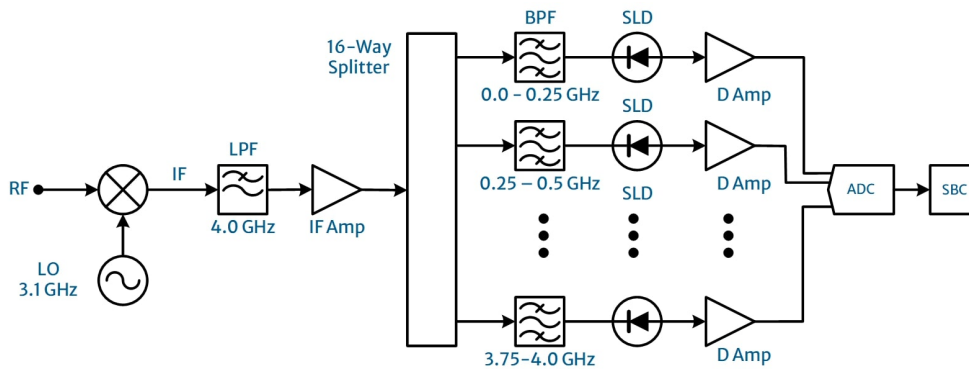


Fig. 4.9: Proposal of a filter-bank radiometer.

The RF band of 3.1 – 7.1 GHz is down-converted to an IF of 0 – 4 GHz using an LO of 3.1 GHz. After that, the IF is filtered using a Low Pass Filter (LPF) and the resulting band is amplified using the IF Amp. Then, the signal is split into 16 nodes of the filter-bank. Narrow-band Band Pass Filters (BPF) are used to divide the 4 GHz IF into sixteen 250 MHz channels. The signals are passed through Square-Law Detectors (SLD) and the resulting DC signals are amplified by the D-Amp. An Analog-to-Digital Converter (ADC) digitizes all signals to be finally processed by the SBC

This scheme has a reliable, practical design, and it is straight-forward to implement. In addition, the signal read-out and processing can be done simultaneously by the SBC. However, the implementation of the narrow-band filters represents an expense of time and a considerable increase in overall cost due the rigorous and delicate manufacturing process.

4.2.2 Tunable Oscillator

The tunable oscillator architecture is an alternative to the filter-bank spectrometer which reduces the number of devices to be used. By sweeping the frequency of the local oscillator, a single channel can be tuned across the entire 4 GHz bandwidth. The proposed architecture (see Fig. 4.10) measures the power in sixteen 250 MHz channels, but this time the channels are read sequentially, and there is a single IF bandwidth (and hence a low-pass filter) of 0 – 250 MHz.

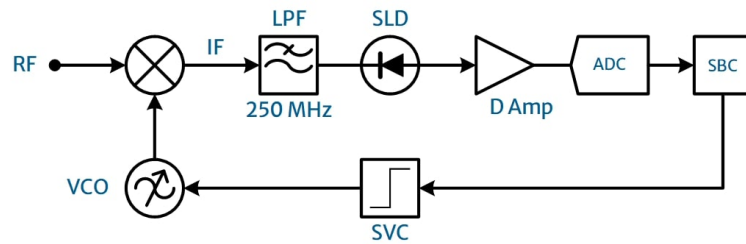


Fig. 4.10: Proposal of a tunable-oscillator radiometer.

The RF band is sequentially down-converted to a 250 MHz band using a tunable oscillator at 16 frequencies: from 2.85 to 6.85 GHz. The IF band is low-pass filtered with a 250 MHz cutoff: the power is obtained by the SLD and amplified by the D Amp. Later, an ADC digitizes the signal and an SBC acquires it. The computer synchronizes the read-out process with by tuning the Voltage Controlled Oscillator (VCO) using the Step Voltage Controller (SVC).

As may be noted, this architecture uses fewer components compared to the filter bank, which means a physically compact design and a lower manufacturing cost. This also reduces the assembly and testing time. Nevertheless, it increases the observation time since the signal read-out is performed sequentially, unlike the filter bank.

4.2.3 Digital Spectrometer

Digital stages in modern scientific instruments provide many high-end features to the devices. Under this philosophy, a third architecture for the radiometer is proposed (see Fig. 4.11). This topology is based on an RFSoc, a digital platform that can be configured according to the user's needs. The architecture implements an analog down-conversion stage and the resulting signal is acquired by the RFSoc to be processed by a digital spectrometer.

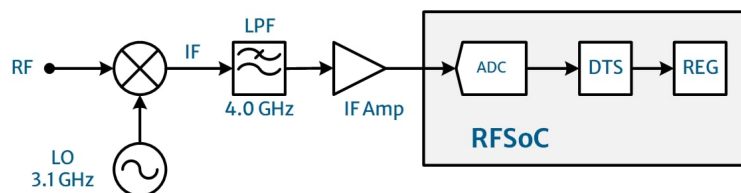


Fig. 4.11: Proposal of a digital spectrometer.

The IF signal processing in this scheme is the same as the filter-bank architecture but up to the splitter. The signal is acquired by the RFSoc after the IF Amp. Internally, the RFSoc's ADC digitizes the IF signal, and a Discrete-Time Spectrometer (DTS) processes the signal to give us the IF power spectrum. Finally, the spectrum is stored in a Digital Register (REG).

This scheme provides signal processing versatility because the RFSoc is based on a *Field-Programmable Gate Array* (FPGA), a powerful acquisition and processing tool. Besides the compactness of this architecture, it also has an interesting feature: since the spectral power measurement is digitally done by the DTS, the topology allows us to have as many frequency

channels as possible. This seems to indicate that there is no resolution limit in implementing this scheme, but in practice the limit is compromised by the hardware capabilities of the digital board, basically by the number of *Configurable Logic Blocks* (CLB) available. Despite these features, the digital design of discrete-time spectrometers using these platforms can be complex, and it requires many hours of description and synthesis and a high-level knowledge of digital electronics, which represent a challenge to the designer.

The analog filter bank and the tunable architectures are definitely straight-forward to implement and the manufacturing costs are similar in both cases. However, we will be limited to measuring the water vapor line intensity in a few spectral windows, which means a low-resolution profile reconstruction. Although this is enough to obtain basic atmospheric parameters, we will lose the ability to characterize the emission profile in detail (as we mentioned in Section 4.1.3), and also the possibility of developing other types of atmospheric profiles. By contrast, the digital topology can provide a better spectral resolution and many signal processing possibilities, and it is not only constrained to measuring the power of the water vapor line spectrum. This means that we can retrieve complex atmospheric profiles if necessary. Furthermore, this architecture allows the processing to be transferred to an external and much more powerful platform such as an *Integrated Development Environment* (IDE) compatible with *Software-Defined Radio* (SDR) systems. Taking this into consideration, we lean towards the digital spectrometer architecture for the various benefits it provides.

4.3 Prototype

Following the conclusions of the above sections, we design a radiometer prototype to be implemented with the KRx. We discuss the technical aspects, design and assembly considerations of the radiometer in this section. It is important to remember that this work is focused only on the design and the implementation of the back-end stage in such a way that the KRx does not require any hardware modification.

4.3.1 Architecture

The prototype is based on the digital scheme we presented in Fig. 4.11 above, but we customize the final design. The prototype architecture consists of an analog down-conversion section and a digital acquisition and processing stage, as anticipated in Fig. 4.1. The down-conversion output was designed to be compatible with the acquisition specifications of the digital platform. The prototype topology is shown in Fig. 4.12.

Following Fig. 4.12, the output signal of the KRx's RCP channel (4 GHz wide) is split in two. Then, each signal is mixed with one of the two different LO signals tuned at two different frequencies, which gives two different IF bands. These IF bands are low-pass filtered using their respective LPF, and then they are amplified by the Amps to be finally sent to the Digitization system. The signals are then acquired by the ADCs of the RFSoc board. After acquisition, the Digital Signal Processor (DSP) computes the power spectrum of the signals. Next, the spectrum is buffered and sent through a Data Transfer Interface (DTI) to the Data Visualisation and Monitoring (DVM) stage. The DVM is basically an external personal computer where a virtual *Python* environment plots the complete spectrum.

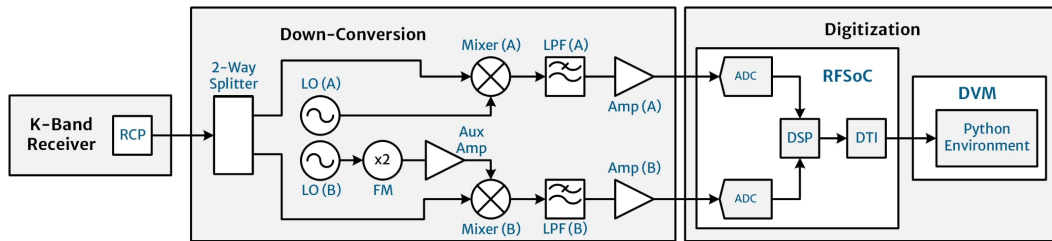


Fig. 4.12: Prototype's architecture.

4.3.2 Down-Conversion Stage

The down-conversion stage is responsible for lowering the frequency of the KRx band in order to condition the signal with respect to the input stage of the Digitization System. Referring back to Table 4.1, the input frequency band (RCP node) is 4 GHz wide, covering from 3.1 to 7.1 GHz. The stage is shown in Fig. 4.13. As can be seen, we use a dual-output Local Oscillator Module which provides two independent frequencies. At the end of the chain, CHA and CHB allow us to cover the full 4 GHz IF, separating it into two 2-GHz IF bands.

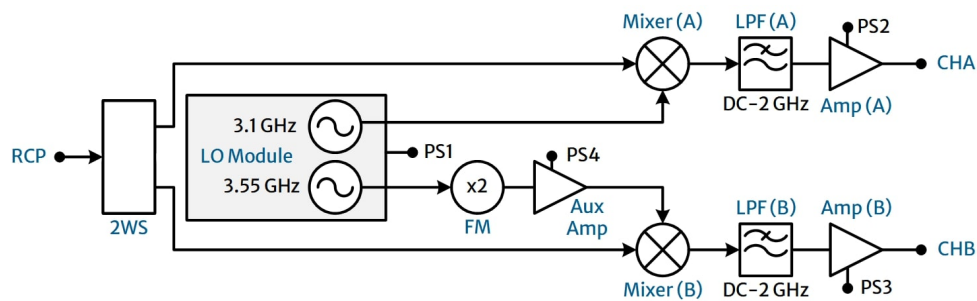


Fig. 4.13: Schematics of down-conversion stage.

Follow the down-conversion process by analyzing Fig. 4.13 and Fig. 4.14. The RCP signal (v_{RF}) is split in two-ways by the 2-way splitter (2WS) block and after that, the resulting signals are mixed with local oscillator signals (v_{LO}) of 3.1 and 7.1 GHz as

$$v_{IF} = v_{RF} - v_{LO} . \quad (4.8)$$

In this way,

- By mixing the RCP band (3.1-7.1 GHz) with a 3.1 GHz tone, we obtain an IF band from 0 to 4 GHz. After the Low-Pass Filter (LPF) this band is reduced to 0-2 GHz and so, CHA contains information within 3.1-5.1 GHz of the input band (see Fig. 4.14a). As can be seen, the LO tone is directly injected into the Mixer (A).
- By mixing the RCP band with a 7.1 GHz tone, we obtain an IF from -4 to 0 GHz, which is naturally inverted to 0-4 GHz. We also reduce this band to 0-2 GHz with a LPF to get the information from 5.1-7.1 GHz of the input band (see Fig. 4.14b). Unlike CHA, the

LO signal of channel B is tuned to 3.55 GHz instead of 7.1 GHz because the LO Module has an upper limit of 6 GHz. This was solved by adding a Frequency Multiplier (FM, factor-of-two) to the chain. In this sense, by using a LO of 3.55 GHz and doubling it with the FM, we reach the desired 7.1 GHz. To compensate the loss added by the FM, we connect an auxiliary amplifier (Aux Amp) between the FM and the Mixer (B) in this chain.

After the LPFs, both channels are amplified by their respective amplifier (Amp) to compensate for the loss of the chain. Finally, CHA and CHB are sent to the Digitization System for acquisition and processing.

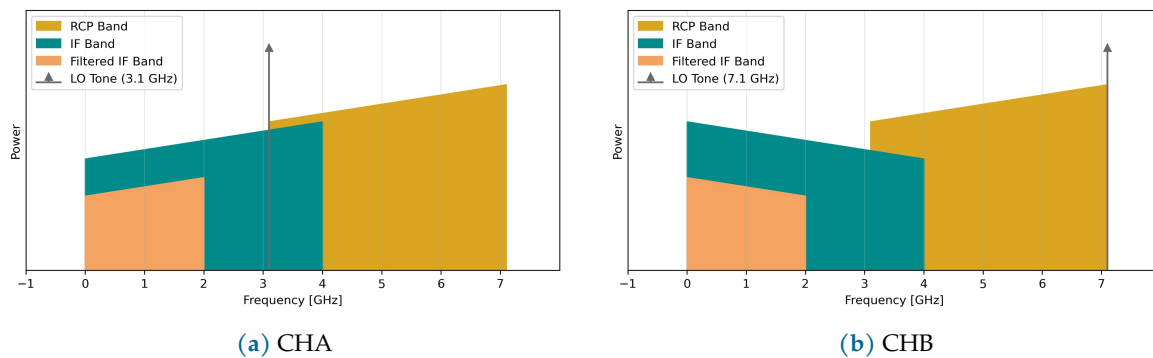


Fig. 4.14: Frequency conversion maps.

The down-conversion circuit is assembled with commercially available RF devices, manufactured by Mini-Circuits® and Valon Technology®, which are listed in Table 4.7. In addition, the amplifiers Amp (A), (B), Aux Amp and the local oscillator module are supplied with power provided by the PS1, PS2, PS3 and PS4 modules (see Section 4.3.5)

Table 4.7: RF devices used for the down-conversion stage.

Label	Model	Feature	Value	Datasheet
2WS	ZFRSC-123-S+	Total Loss	9.67 dB	Mini-Circuits (2023a)
		Bandwidth	0 – 12 GHz	
LO Module	Valon 5009	Output Power	±15 dBm	Valon Technology (2020)
		Bandwidth	0.025 – 6 GHz	
Mixer (A)	ZMX-10G+	Conversion Loss	5.0 dB	Mini-Circuits (2023b)
Mixer (B)		Bandwidth	3.7 – 10 GHz	
LPF (A)	VLF-2250+	Insertion Loss	0.51 dB	Mini-Circuits (2023c)
LPF (B)		Bandwidth	0 – 2.2 GHz	
Amp (A)	ZX60-P33ULN+	Gain	14.8 dB	Mini-Circuits (2023d)
Amp (B)		Bandwidth	0.4 – 3 GHz	
FM	ZX90-2-24-S+	Conversion Loss	24 dB	Mini-Circuits (2023e)
		Bandwidth	5 – 10 GHz	
Aux Amp	ZX60-83LN-S+	Gain	21.9 dB	Mini-Circuits (2023f)
		Bandwidth	0.5 – 8 GHz	

4.3.3 Digitization System

The digitization system consists of the digital platform and data monitoring process. The first one refers to the *RFSoc 2x2* development board, manufactured by HiTech Global® and supported by the Xilinx® University Program. The second one refers to the *Python* environment used to display the power spectrum on a personal computer.

Following the scheme shown in Fig. 4.15, the resulting signals from the down-conversion stage, CHA and CHB, are respectively acquired by the RFSoc’s on-board Analog-to-Digital Converters ADC1 and ADC2. Once digitized, both signals are processed by the DSP which calculates the power spectrum. After that, the spectrum is sent via Gigabit Ethernet (GbE) to *casperfpga* environment, installed on the Personal Computer (PC). Here the spectrum is visualized using *Python* commands.

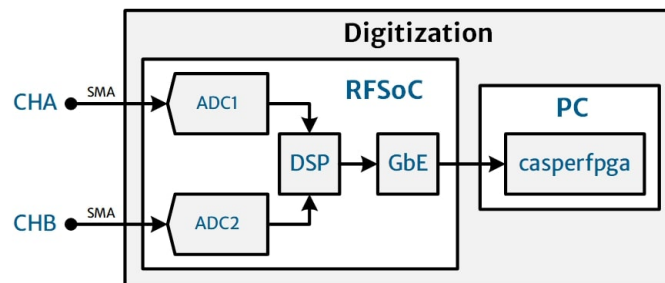


Fig. 4.15: Digitization system topology.

The RFSoc 2x2 is a development board with capabilities for radio frequency signal acquisition, processing and generation. The RFSoc is an FPGA-based system combined with high-precision and fast Analog-to-Digital and Digital-to-Analog converters and programmable heterogeneous computing engines (Xilinx, Inc., 2023). Substantial features of the RFSoc 2x2 are listed in Table 4.8, and a detailed overview can be found in PYNQ Project (2023).

Table 4.8: RFSoc key features (Xilinx, Inc., 2023).

Feature	Description	Capability
FPGA Chip	ZYNQ UltraScale+ RFSoc XCZU28DR	—
	System Logic Cells	930,000
	2x Radio Frequency ADC	12-bit @ 4.096 GSPS
	2x Radio Frequency DAC	14-bit @ 6.554 GSPS
I/O Interfaces	1x USB 2.0	UART/JTAG
	3x USB 2.0	2 Host / 1 Slave
	Ethernet	up to 1 GbE
	Serial Comms Interfaces	I2C/SPI/CAN
Memory	2x DDR4	4 GB, 64-bit
	1x Micro SD slot	up to 128 GB
Clock Sources	Processing System	33 MHz
	Programmable Logic	128 MHz
	Radio Frequency	12.288 MHz

CASPER The *Collaboration for Astronomy Signal Processing and Electronics Research* is a community of scientists and engineers who develop digital resources and design hardware for various fields of astronomy (CASPER, 2018a). This group has provided open-source software and hardware tools as an aid to astronomy research since the early 2000s (Hickish et al., 2016). Among these tools is the *CASPER Toolflow* which generates Simulink libraries for digital signal processing and hardware interfaces. We take advantage of this tool to develop the signal processing system of this work.

The PC is a laptop with the *Ubuntu* distribution of *Linux* operating system installed. This unit is used for two purposes: to program the RFSoc and to communicate with it for displaying the processed data. To accomplish this, we installed three essential software packages on the system:

- (a) The Matlab Simulink® environment for graphical block design.
- (b) The Xilinx *Vivado* Design Suite for hardware description of the RFSoc.
- (c) The *CASPER Toolflow* (hereafter CTF) with a virtual *Python* environment, which provides all digital interfaces between (a),(b) and the RFSoc.

The versions of the software installed on the PC are shown in Table 4.9. This set is recommended in CASPER (2018b) and ensures the correct functioning of the ecosystem.

Table 4.9: Compatibility of software versions for the RFSoc 2x2.

Ubuntu	Matlab	Vivado	CTF	Python
20.04	2021a	2021.1	m2021a	3

CTF allows the design of signal processing blocks using Simulink graphical programming, and subsequently describe them into the RFSoc. For this purpose, it is extremely important to follow instructions provided by CASPER (2018c) to avoid errors, incompatibilities and gaps in CTF installation. If successful, the CTF repositories appear in the `mllib_devel` folder, which includes three primordial repositories:

- (a) `casper_library` — Contains the source code of simulink blocks for digital signal processing.
- (b) `xps_library` — Contains the source code of Simulink blocks for hardware interfaces.
- (c) `jasper_library` — Contains the source code to generate the RFSoc’s description files from the Simulink block diagram.

Once all the software is installed, the user can start designing with Simulink workbench. An example of design is shown in Fig. 4.16: the green blocks are provided by the `casper_library`, the yellow blocks by the `xps_library`, and the blue blocks by the Xilinx Blockset, which are generated when Vivado is installed.

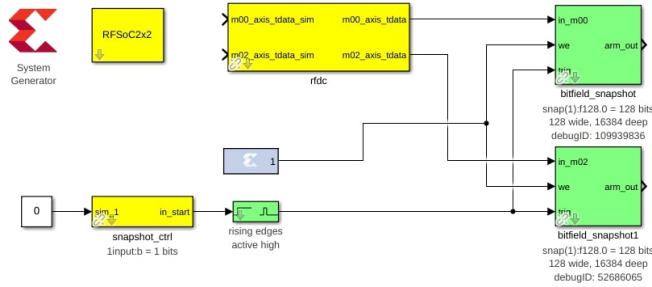


Fig. 4.16: Simple implementation of CASPER rfdc acquisition block for the RFSoc 2x2 board.

Finally `casperfpga` is the virtual *Python* environment which allows interaction with the RFSoc from the PC. In our case, `casperfpga` is used for data acquisition and loading of description files as bit-streams via GbE, to and from the RFSoc. It is worth mentioning that this environment is installed at the same time CTF is installed.

Using CASPER tools, we can program, validate and communicate with the RFSoc. First, let's discuss the RFSoc programming and validation process following the flowchart in Fig. 4.17. The communication process will be addressed in Section 4.3.4.

1. Start the session and execute Simulink using the `startsg` script from the CTF folder.
2. Design the block diagram in Simulink.
3. Run a simulation to ensure the virtual functioning of the diagram.
4. If simulation successful, start the subsequent subprocesses. Else, return to block diagram designing.
 - (a) Inside the Matlab workspace, execute the `jasper` routine to compile the block diagram.
 - i. After compilation, the `fpg` file is generated. This is the final bitstream file.
 - ii. Move the `fpg` file to the `casperfpga` folder.
 - (b) Activate the `casperfpga` environment.
 - i. Try to connect to the RFSoc via GbE.
5. If both subprocesses are done successfully, load the `fpg` file to the RFSoc using `casperfpga` commands within this environment. Immediately, the block diagram executes on the RFSoc. Else, check again if the `fpg` file is in the `casperfpga` folder, or retry connecting to the board.
6. If the behavior of the RFSoc matches the block diagram's, the programming is done. Otherwise, return to block diagram designing.

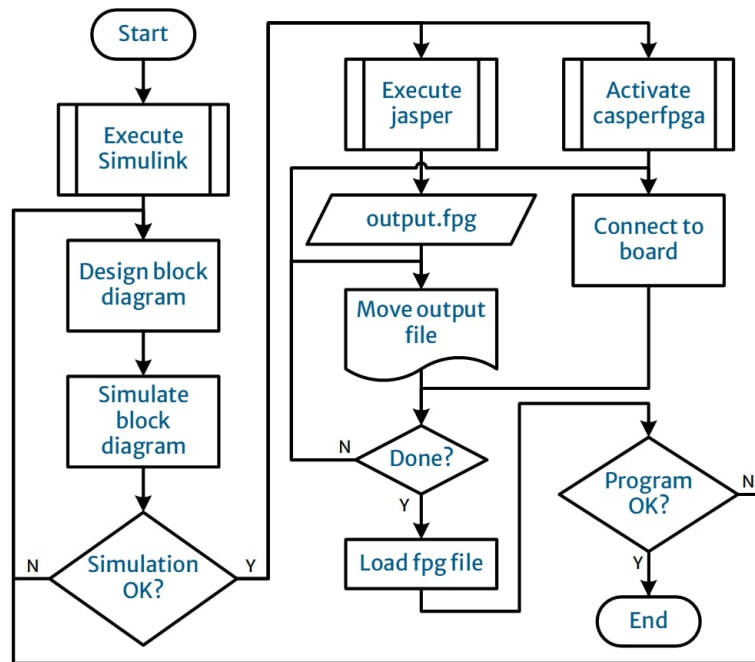


Fig. 4.17: RFSoc programming process.

4.3.4 Implemented Spectrometer

As discussed in Section 4.2.3, the digital architecture provides programming and processing versatility. By using the RFSoc, we are free to implement an algorithm to obtain the power spectrum of the input signal. In our case, we select the classic scheme, which consists of a Polyphase Filter-Bank (PFB) plus a channelized Fast Fourier Transform (FFT) algorithm. The implemented topology and its stages are shown in Fig. 4.18.

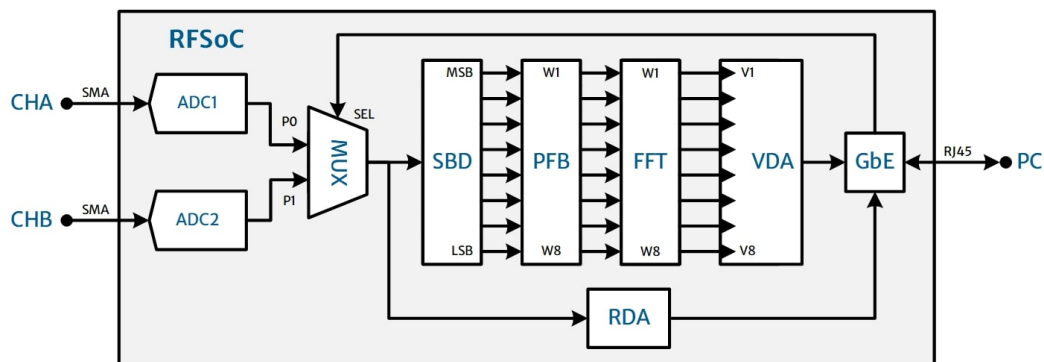


Fig. 4.18: Digital architecture of the spectrometer.

The signals are acquired by the ADC1 and ADC2 (packaged in 256-bit vectors each), and upon user instruction via GbE, a multiplexer (MUX) selects the acquisition port: the ADC1 is connected to Port 0 (P0), whereas the ADC2 is connected to Port 1 (P1). At this point, the signal is split for both the FFT processing stage and the Raw Data Acquisition (RDA) block;

the latter acquires the signal in the time domain and then sends it to the GbE data transmission block. On the other path, a Serial Bus Divider (SBD) parallelizes the incoming 256-bit data on eight channels of 32-bit length each. The PFB divides the incoming signal on 64 digital channels using digital band-pass filters of 31.25 MHz, giving a total of 128-channels for the entire 4 GHz bandwidth. After that, the signal is processed by a 64-point FFT algorithm to obtain the power spectrum. This output spectrum is stored in 8 data registers, using the Vector Data Accumulator (VDA). Finally, these packages are serially transmitted to the PC via GbE. The Simulink's block diagram with references to this scheme is shown in Fig. 4.19. Additionally, other sections can be found: the *Software Registers* and *Sync Control*, which configure the parameters for acquisition and synchronizes them with the data transmission².

Since this topology allows us to reduce the net number of spectral components, the FFT processing time will be reduced considerably (Crockett et al., 2023). Likewise, aliasing is significantly reduced, as the high-frequency components processed by the FFT are attenuated, and sometimes eliminated (Proakis and Manolakis, 2006). Nevertheless, the digital windowing function and the sampling process decrease the effective bandwidth in processing (Crockett et al., 2023). In our case, the expected 2 GHz bandwidth is digitally reduced to ~ 1.96 GHz, as reported in CASPER (2018d).

²See clean version in Fig. C.1, Appendix C.

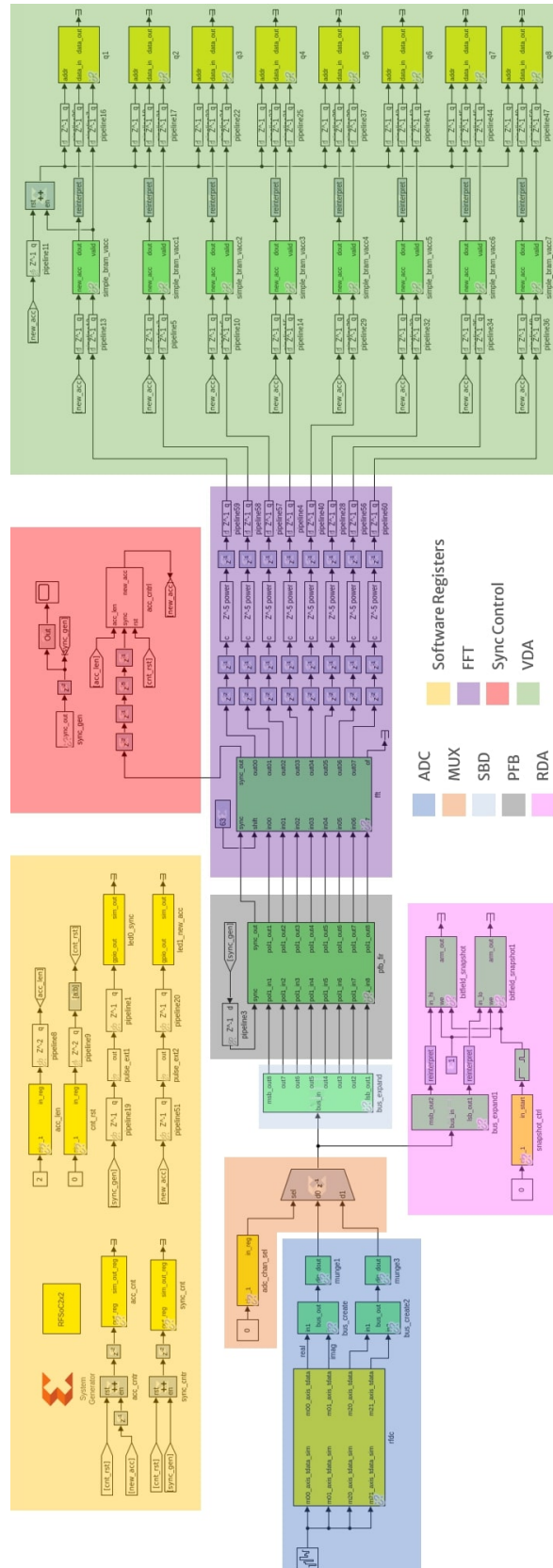


Fig. 4.19: Design of the digital spectrometer: Simulink's block diagram and its sections.

4.3.5 Assembly

The back-end system is enclosed in a rack-type box, which also has integrated power supplies and external connection lines. The mounting scheme is shown in Fig. 4.20.

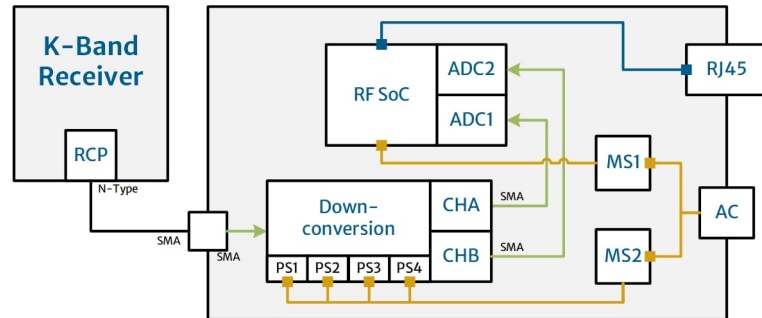


Fig. 4.20: Mounting scheme of the back-end.

The connection between the KRx and the back-end is done via coaxial cable. From the KRx side, the cable-end is N-type connector, and from the back-end side, the cable-end is SMA connector. This cable is connected to an SMA connector receptacle from outside the enclosure. All analog signals inside the enclosure travel through coaxial cables (green lines) with SMA connectors on both ends. On the other hand, the yellow lines refer to power supply lines, whereas the blue line refers to the communication line between the RFSoc and the external computer. This is an Ethernet cable with RJ45 connectors on both ends, and an RJ45 receptacle provides the connection from the outside of the enclosure.

Two main power sources supply the system: MS1 is connected directly to the RFSoc board, and MS2 is connected to the PS1, PS2, PS3 and PS4 in the down-conversion stage. Both MS1 and MS2 supplies are connected to a power AC receptacle mounted on the chassis. The DC and AC features of power supplies are listed in Table 4.10 and Table 4.11, respectively.

Table 4.10: DC features of power supplies.

Label	Model	Output (DC)	Value	Datasheet
MS1	CJ-1206 (AC supplied)	Voltage	+12 V	Generic
		Current	6 A	
MS2	TDK LS25-15 (AC supplied)	Voltage	+15 V	TDK-Lambda (2023)
		Current	1.7 A	
PS1	LM2596 Module	Voltage	+6 V	OnSemi (2022)
		Power	3.6 W	
PS2	LM317 Module	Voltage	+3 V	OnSemi (2021)
		Power	168 mW	
PS3	LM317 Module	Voltage	+3 V	—
		Power	168 mW	
PS4	LM2596 Module	Voltage	+6 V	—
		Power	462 mW	

Table 4.11: AC features of the power supplies.

Label	Model	Input (AC)	Value	Units
MS1	CJ-1206	Voltage	120	V
		Current	1.6	A
MS2	TDK LS25-15	Voltage	120	V
		Current	0.7	A

Following the values of Table 4.10, the DC power consumption results in 97.5 W by only considering the main sources MS1 and MS2, which supplies the entire back-end. On the other hand, the AC features of these power supplies gives an AC power consumption of 276 W total at maximum load.

The prototype was mounted on a phenolic type plate, whose conductive plane was used as the general ground plane and heat sink. The assembled back-end is shown in Fig. 4.21: as can be seen, the entire back-end fits on the 30x30 cm plate area, and for aesthetic reasons only, the PS1, PS2, PS3 and PS4 sources were placed on the same board as the rest of the components. On the other hand, the MS1 and MS2 sources were placed outside the main plate.

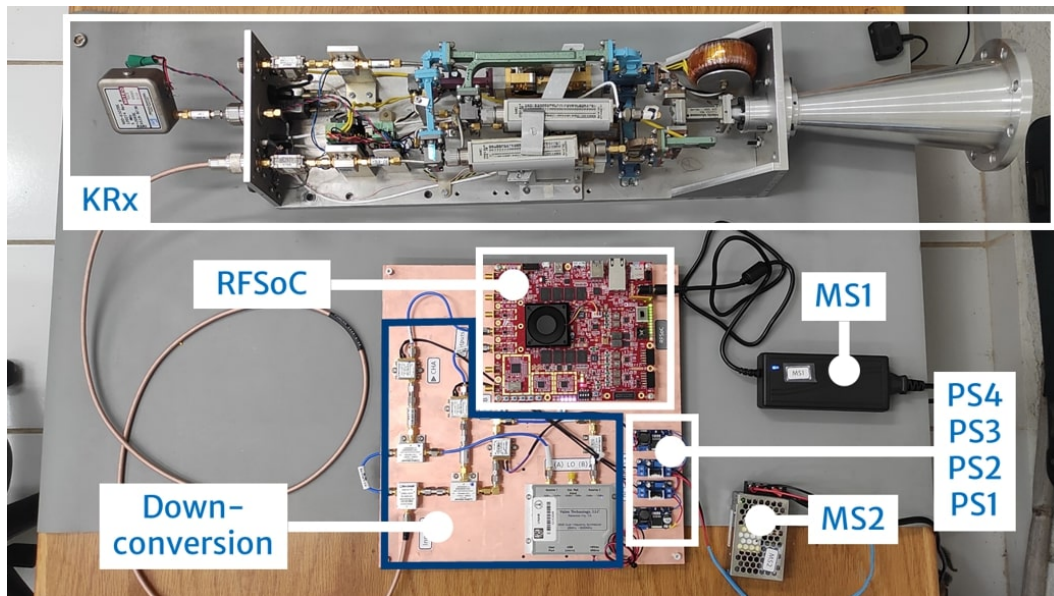


Fig. 4.21: Final assembly of the back-end (bottom) and the KRx(top). Several other components are also indicated.

4.3.6 Costs

We present the prototype budget table. The following table only shows the back-end costs since the KRx is an academic loan from HartRAO. Note that the grand total of the quotation does not include shipping costs or commercial taxes.

Table 4.12: Back-end budget.

Device Model	Description	Items	Unit Price (USD) ⁺	Total Price (USD)
RFSoc 2x2 Kit	FPGA platform	1	\$ 2,149.00	\$ 2,149.00*
ZFRSC-123-S+	2-way splitter	1	\$ 94.81	\$ 94.81
Valon 5009	Frequency synthesizer	1	\$ 699.00	\$ 699.00
ZMX-10G+	Frequency mixer	2	\$ 103.66	\$ 207.32
VLF-2250+	Low-pass filter	2	\$ 31.56	\$ 63.12
ZX60-P33ULN+	Low-noise amplifier	2	\$ 145.41	\$ 290.82
ZX90-2-24+	Frequency multiplier	1	\$ 94.81	\$ 94.81
ZX60-83LN-S+	Low-noise amplifier	1	\$ 208.66	\$ 208.66
TDK LS25-15	Switching power supply	1	\$ 21.33	\$ 21.33
LM2596 Module	Voltage regulator	2	\$ 2.50	\$ 5.00
LM317 Module	Voltage regulator	2	\$ 3.35	\$ 6.70
086-3SW+ / 6SW+	SMA Flex interconnect	5	\$ 14.96	\$ 74.8
SM-SM50+	M/M SMA adapter	5	\$ 7.52	\$ 37.60
132172	M/F SMA adapter RA	3	\$ 14.53	\$ 43.59
Miscellaneous	Screw sets, soldering supplies, etc.	—	\$ 40.00	\$ 40.00
			Total	\$ 4,036.56

⁺ Prices effective until October 2023.

* Academic price.

RADIOMETER FEATURES

The current chapter deals with the technical aspects of the prototype, including both analog and digital characterization of the back-end. In addition, we present the results of the measurements and snapshots of the spectrometer during bench tests to pre-validate the functionality of our proposal.

5.1 Analog Features

In this section we describe the main analog features of the back-end. These technical characteristics refer only to the down-conversion stage.

5.1.1 Bandwidth

As discussed in Section 4.3.2, the down-conversion stage takes the 3.1 to 7.1 GHz output band of the KRx and translates it to 0 - 2 GHz in two separated bands, i.e., the analog bandwidths of each channel are

$$\Delta\nu_{\text{CHA}} = 2 \text{ GHz} ,$$

$$\Delta\nu_{\text{CHB}} = 2 \text{ GHz} ,$$

giving a total of $\Delta\nu = 4$ GHz, but acquired sequentially.

5.1.2 Gain

For gain characterization, we use a bench Vector Network Analyzer (VNA, Keysight N5242A) to measure the dispersion parameter S_{21} , which directly gives the gain of a 2-port system (Pozar, 2011). For this purpose, we used the following procedure:

1. We connected the VNA's Port 1 to the back-end input (RCP node of Fig. 4.13) and the Port 2 to the output of channel A (CHA node of Fig. 4.13), as shown in Fig. 5.1a.
2. We select the S21 measurement, setting a -30 dBm output signal swept from 0 – 6 GHz on the VNA and stored the data.

3. We repeat the steps 1 and 2 for channel B, but taking the CHB node of Fig. 4.13 as the output. See Fig. 5.1b.

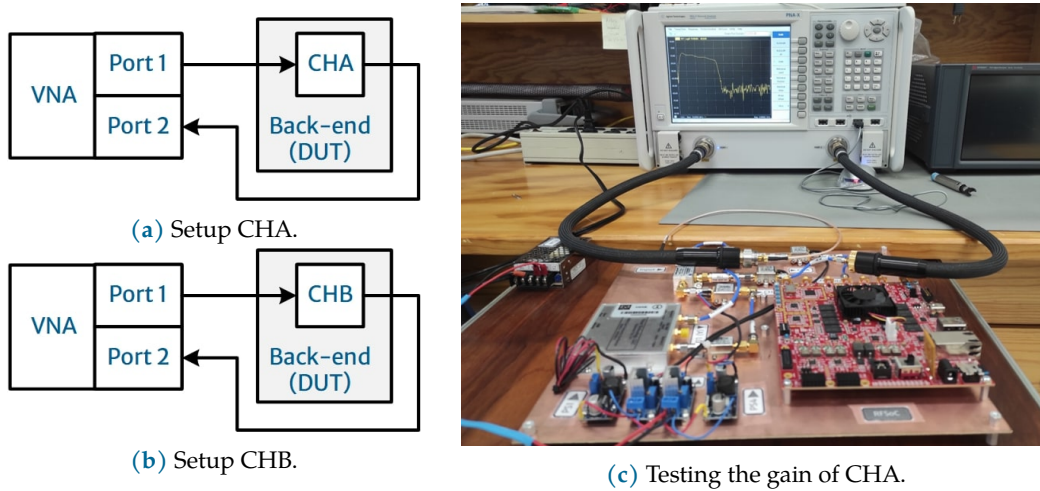


Fig. 5.1: Back-end gain measurements.

The resulting data are shown in Fig. 5.2: as expected, the gain decreases as we increase the frequency. From the curves it may be noted that the cutoff frequency in both channels is ~ 2.5 GHz, and the gain decay of CHA is greater than that of CHB over the pass-band.

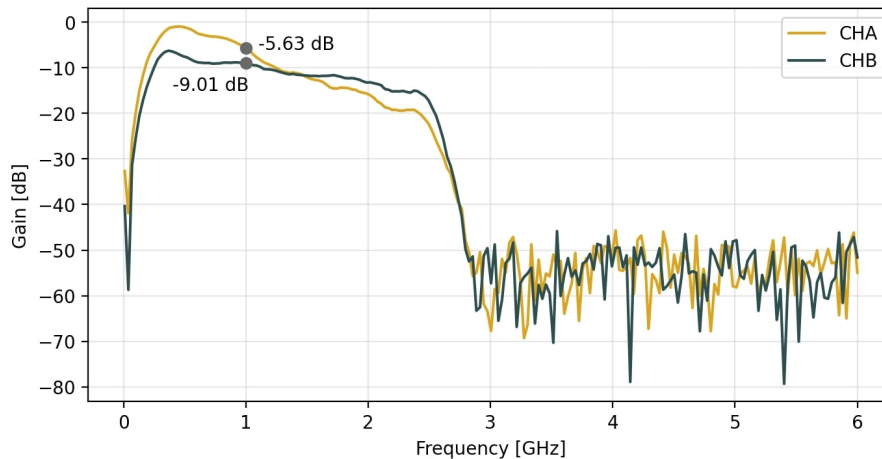


Fig. 5.2: Gains of the back-end channels. The gains of each channel at 1 GHz are labeled.

Averaging over the passband, the mean gains within the IF band (0 – 2 GHz) are

$$G_{\text{CHA}} = -9.53 \text{ dB} \quad \text{and} \quad G_{\text{CHB}} = -12.10 \text{ dB} .$$

5.1.3 Noise Figure

It is clearly seen from Fig. 5.2 that the down-conversion stage presents a negative gain. As a result, the chains behaved like a passive device and hence, it was quite difficult to estimate the noise factor using the Y-factor method, because the noise injection will be undetectable by the spectrum analyzer (Reeve, 2014). However, the noise figure can still be found with analytical methods supported with gain measurements.

The *equivalent noise temperature* of a passive device is given by

$$T_e = (A - 1)T_0, \quad (5.1)$$

where $A = G^{-1}$ is the attenuation (or insertion loss) of the device, and $T_0 = 290$ K is the reference temperature. On the other hand, the noise factor is defined as

$$NF = 10 \log \left(1 + \frac{T_e}{T_0} \right). \quad (5.2)$$

Combining Eq. (5.1) and Eq. (5.2) we find that $NF = 10 \log(A)$, i.e., the noise figure of a passive device is completely defined by its attenuation. In this sense, we estimate the noise figure of CHA and CHB using the gain measurements of the previous section. First, we take the gain of the channels to find their attenuation as

$$A = 10^{-(G_{dB}/10)}. \quad (5.3)$$

From this attenuation, we calculate the noise figure along the pass-band for each channel using Eq. (5.3), obtaining the plots of Fig. 5.3.

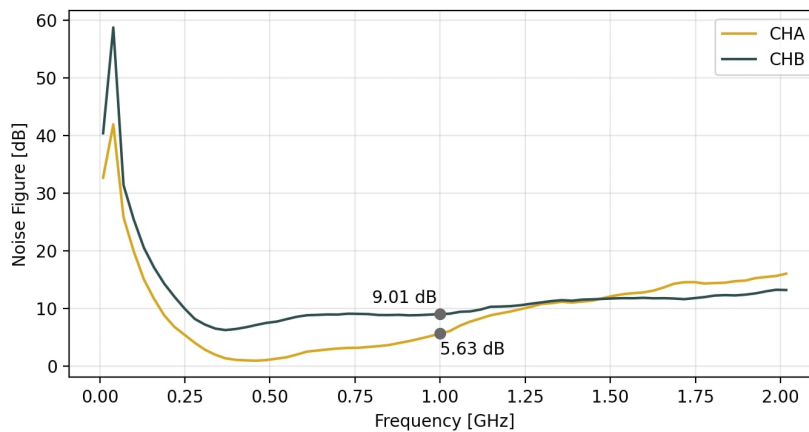


Fig. 5.3: Noise figure of the back-end channels. The noise figures of each channel at 1 GHz are labeled.

Averaging values across the passband, the mean noise figures within the IF band (0 – 2 GHz) are

$$NF_{CHA} = 9.53 \text{ dB} \quad \text{and} \quad NF_{CHB} = 12.10 \text{ dB},$$

which are equivalent to noise temperatures of

$$T_{e,CHA} = 2312 \text{ K} \quad \text{and} \quad T_{e,CHB} = 4413 \text{ K}.$$

5.1.4 Sensitivity

Let us estimate the sensitivity of the instrument by using the ideal radiometer equation (Eq. (4.2)), following the considerations we discussed in Section 4.1.2 and using the results of Section 5.1.1 and Section 5.1.3:

- (a) The brightness temperature due to the water vapor line is $T_{\text{sky}} = 9.5$ K.
- (b) The system noise temperature consists of the KRx and back-end noise temperatures (per channel). We have $T_{\text{KRx}} = 280$ K, $T_{\text{e,CHA}} = 2312$ K and $T_{\text{e,CHB}} = 4413$ K.
- (c) The bandwidth of each channel is $\Delta\nu = 2$ GHz and the observing time is $\tau_{\text{obs}} = 1$ s.

First, the equivalent noise temperatures of the KRx (T_{KRx}) and the back-end channels ($T_{\text{e,CH}}$) as a cascade system are given by

$$T_{\text{rx}} = T_{\text{KRx}} + \frac{T_{\text{e,CH}}}{G_{\text{KRx}}}, \quad (5.4)$$

where G_{KRx} is the gain of the RCP channel. Since $G_{\text{KRx}} = 43$ dB $\equiv 19,953$, we found that

$$T_{\text{rx,CHA}} = (280 \text{ K}) + \left(\frac{2312 \text{ K}}{19,953} \right) = 280.1 \text{ K},$$

$$T_{\text{rx,CHB}} = (280 \text{ K}) + \left(\frac{4413 \text{ K}}{19,953} \right) = 280.2 \text{ K},$$

i.e., a mean noise temperature of $T_{\text{rx}} = 280.15$ K. Hence, the sensitivity of the system achieves

$$\sigma_T = \frac{T_{\text{sky}} + T_{\text{rx}}}{\sqrt{\Delta\nu\tau_{\text{obs}}}} = \frac{(9.5 \text{ K}) + (280.15 \text{ K})}{\sqrt{(2 \times 10^9 \text{ Hz})(1 \text{ s})}} \quad (5.5)$$

$$\boxed{\sigma_T = 6.5 \times 10^{-3} \text{ K}} \quad (5.6)$$

As discussed in Section 1.2.3, the 22 GHz water vapor emission line requires a high-sensitivity instrument to detect the changes per millimeter of water vapor content. Considering the sensitivity of ~ 0.4 K mm⁻¹ reported by Wiedner (1998), the result of Eq. (5.6) indicates that we can easily detect the change of 1 mm with ~ 60 times more sensitivity. Alternatively, with a 6.5 mK rms we can detect a change of 0.16 mm with a signal-to-noise ratio of 10 in PWV.

5.1.5 Spurs

The third-order intermodulation products (IP3, see Appendix D) for the down-conversion stage were calculated for the RF band (3.1 – 7.1 GHz) and local oscillators of 3.1 and 7.1 GHz. From Table D.1 we can observe that for $\nu_{LO} = 3.1$ GHz and $\nu_{RF} = [4.2, 7.1]$ GHz these terms fall in

$$\nu_{IP3,CHA} = [0.0, 2.0] \text{ GHz} .$$

From Table D.2 we found that for $\nu_{LO} = 7.1$ GHz and $\nu_{RF} = [3.1, 4.5]$ GHz the IP3 terms fall in

$$\nu_{IP3,CHB} = [0.1, 1.9] \text{ GHz} ,$$

which means that both channels contain this type of spurs along the entire pass-band. This is not necessarily a serious problem. When dealing with low input powers, IP3 components can be negligible (even smaller than the receiver noise floor). However, it should be kept in mind that their magnitude will rise rapidly with increasing input power because their power increases as the cube of the input (Gustrau, 2012).

To verify the intermodulation spurs, we analyze the back-end response to a 50-Ohm input load. We connect the load to the back-end, then we measure the output spectrum for each channel using the Keysight N9010B spectrum analyzer, as shown in Fig. 5.4.

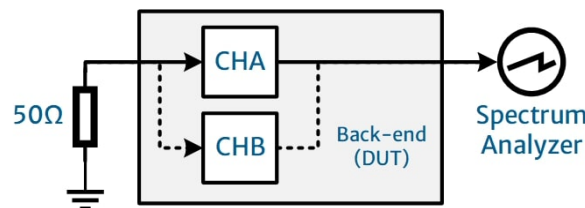


Fig. 5.4: Setup to measure the response to a 50-Ohm load.

Then, we find the spurs of Table 5.1 for the back-end channels.

Table 5.1: Analog spurs of the back-end.

Spur		1	2	3	4
CHA	Frequency	450 MHz	900 MHz	1.35 GHz	1.75 GHz
	Power	-42.26 dBm	-50.63 dBm	-55.51 dBm	-56.38 dBm
CHB	Frequency	450 MHz	900 MHz	1.35 GHz	—
	Power	-43.10 dBm	-26.43 dBm	-51.64 dBm	—

Spurs in the spectra are shown in Fig. 5.5. Note that the fourth spur in CHB is so weak that it falls on the noise floor of the analyzer. In fact, these spurs also appear in the digitized spectra, see Fig. 5.7.

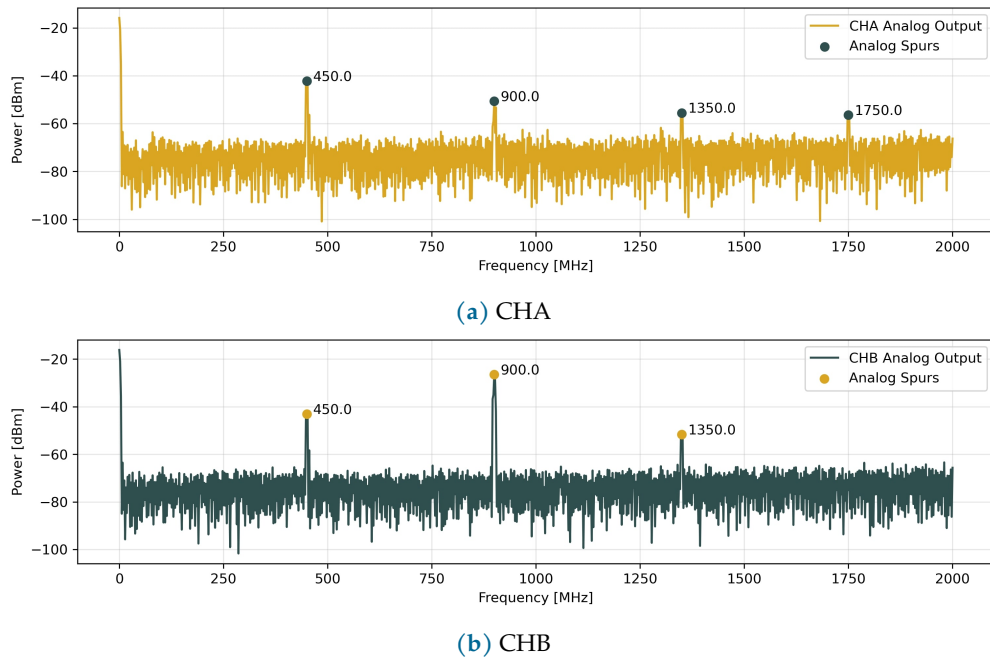


Fig. 5.5: Output spectra and spurs captured with the analyzer.

Regarding the digitization spurs, we use the *Frequency Planner* application provided by [PYNQ Project \(2023\)](#). This tool is dedicated to the FPGA platforms supported by PYNQ, including the RFSoc 2x2. We used this tool to calculate the Digital Down-Converter (DDC) spurs which fall in the passband. First, we set the parameters of Table 5.2 in the tool following the configuration of the programmed `rfdc` block.

Table 5.2: Input parameters of Frequency Planner tool.

Sampling Rate	Input Tone	PLL Clock	NCO Frequency	Decimation	Interleaving
3932.16 MSPS	1.0 GHz	245.76 MHz	-983.04 MHz	1	8

Table 5.3 lists the predicted spurs within the effective digital bandwidth (0–1966.08 MHz): the *Interleaving* spur due to the analog-to-digital conversion, the *Phase-Locked Loop* (PLL) spurs of the DDC, and the frequencies resulting from the mixing between the Sampling Rate and the respective *harmonics* of the Input Tone.

Table 5.3: Spurs due to the DDC.

Spur	Label ⁺	Location	Spur	Label	Location
Interleaving spur	OIS	491.52 MHz	Input Tone	Fc	1000.0 MHz
PLL Clock	PLL Mix Down	754.24 MHz	PLL Clock	PLL Mix Up	1245.76 MHz
3 rd harmonic	HD3	932.16 MHz	2 nd harmonic	HD2	1932.16 MHz

⁺ Labels as given in Fig. 5.6.

Fig. 5.6 shows the simulated DDC response for a 1 GHz input tone. All spurs will be frequency shifted with a shift of the input tone. Additionally, the ordinate axis indicates the spur power with respect to the full-scale signal power. We chose a power level 70 dB weaker for spurs of Table 5.4, as suggested by the manufacturer (Xilinx, Inc., 2020); e.g., the HD3 power is 70 dB weaker than the signal power.

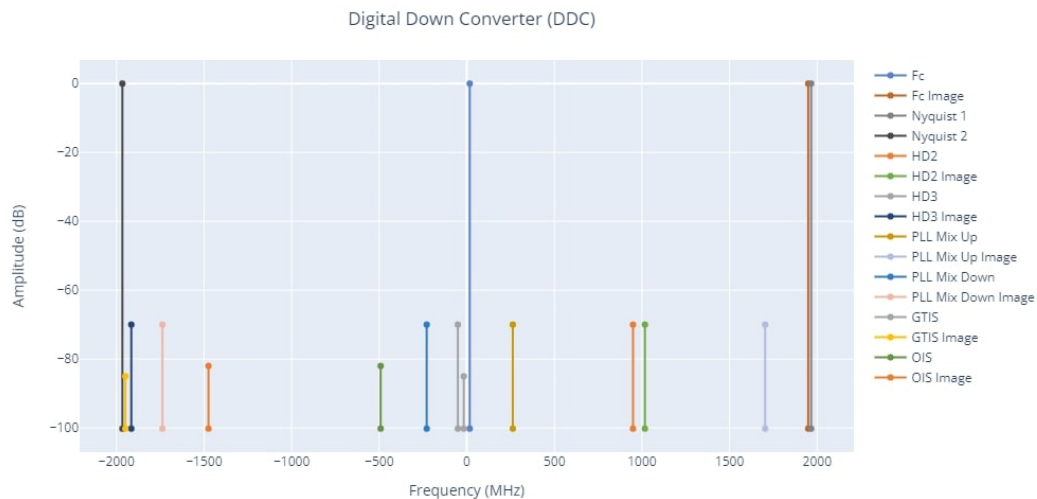


Fig. 5.6: Spur spectrum due to the DDC. Only components between ± 1000 MHz appear in the output spectrum.

Note that Fig. 5.6 shows negative frequencies because of the natural response of the digital converters and processing in discrete-time domain. The real input frequency is shifted by the Numeric Controller Oscillator (NCO) of the converter as

$$v_{\text{digital}} = \begin{cases} v_{\text{analog}} + v_{\text{NCO}}, & \text{if } v_{\text{NCO}} < 0 \\ v_{\text{analog}} - v_{\text{NCO}}, & \text{if } v_{\text{NCO}} > 0 \end{cases}$$

DDC spurs are not a serious problem as long as the power of the desired signal does not increase significantly. It is important to note that the power difference between them remains constant regardless of the change in frequency of the input signal. Assuming that we have well-located this type of spurs, mitigation techniques can be applied to improve the performance of the acquisition (Lin, 2018).

To experimentally locate the spurs after digitization, we obtain the spectra using the configuration of Fig. 5.4 but disconnecting the analyzer and directly acquiring with the RFSoc with high and low-resolution modes. Fig. 5.7 shows the measured spurs. Components of Table 5.1 (dots) and other spurs (diamonds) appear in the acquired spectra.

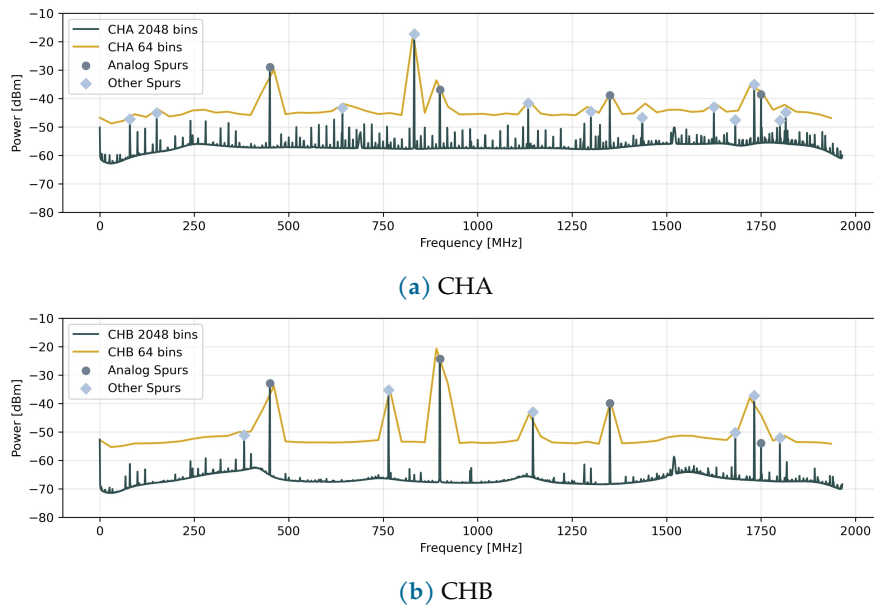


Fig. 5.7: Spurs in the channels of the back-end. We plot both the low and high-resolution modes.

Note how the noise floor rises when we decrease the spectral resolution. This is a typical behavior of spectrum analyzers: the resolution bandwidth behaves like a filter, and narrower filters require more time to stabilize and yield a consistent result compared to broader filters. In practice, increasing the spectral resolution by a factor of 10 results in a 10 dB reduction in the noise floor, approximately. In this sense, to detect signals in proximity to the noise floor, a narrower resolution bandwidth (higher spectral resolution) should be implemented (Denisowski, 2023).

Table 5.4 lists the spurs found in CHA and CHB, whose power lies between

$$-50 \text{ dBm} \leq P_{\text{CHA}} \leq -15 \text{ dBm} \quad \text{and} \quad -55 \text{ dBm} \leq P_{\text{CHB}} \leq -20 \text{ dBm} .$$

Table 5.4: Spurs observed after digitization.

CHA	Analog Spurs	1	2	3	4	—	—
	Frequency [MHz]	450.24	900.48	1349.76	1750.08	—	—
	Power [dBm]	-28.99	-36.89	-38.85	-38.61	—	—
	Other Spurs	1	2	3	4	5	6
	Frequency [MHz]	79.68	150.72	642.24	832.32	1133.76	1299.84
	Power [dBm]	-47.24	-45.10	-43.30	-17.33	-41.64	-44.58
	Other Spurs	7	8	9	10	11	12
	Frequency [MHz]	1435.2	1625.28	1681.92	1731.84	1800.0	1815.36
Power [dBm]	-46.69	-42.99	-47.50	-35.09	-47.76	-44.88	
CHB	Analog Spurs	1	2	3	4	—	—
	Frequency [MHz]	450.24	900.48	1349.76	1750.08	—	—
	Power [dBm]	-32.89	-24.33	-39.87	-53.87	—	—
	Other Spurs	1	2	3	4	5	6
	Frequency [MHz]	382.08	764.16	1146.24	1681.92	1731.84	1800.0
	Power [dBm]	-51.14	-35.27	-42.98	-50.24	-37.28	-52.09

Comparing and analyzing data of Tables 5.1, 5.3 and 5.4 we found that:

- ▶ All analog spurs appear in both channels of the back-end when digitized, and now spur 4 of CHB is detectable.
- ▶ We investigated further¹ and it turned out that all Analog Spurs in both channels are intermodulation products of order higher than 3, from fourth to tenth. The point is that the respective LO signal of the current channel is mixed with the reflected LO signal of the other channel.
- ▶ None of the listed DDC spurs appear in the acquired spectra, at least not with detectable power. But we found interactions between the RFSoc's sampling rate frequency and the local oscillator frequencies of each channel. Specifically, this digital intermodulation occurs with the *Nyquist* frequency F_N . Given that the sampling rate is $F_s = 3932.16$ MHz, we have an $F_N = 1966.08$ MHz.

In this sense, we reorganized the data of Table 5.4 and reclassified them in Table 5.5 as analog intermodulation products (AIP) and digital intermodulation products (DIP). We indicate only the frequency and omit the power in this table.

Table 5.5: Significant spurs of the back-end.

CHA	Spur	1	2	3	4	5	6
	AIP [MHz]	450.24	900.48	1299.84	1349.76	1750.08	1800.00
	Spur	1	2	3	4	5	6
	DIP [MHz]	150.72	832.32	1133.76	1435.2	1625.28	—
CHB	Spur	1	2	3	4	5	6
	AIP [MHz]	450.24	900.48	—	1349.76	1750.08	1800.00
	Spur	1	2	3	4	5	6
	DIP [MHz]	382.08	764.16	1146.24	—	—	—

5.2 Digital Features

5.2.1 Power Calibration

CASPER's interfaces help to acquire data from hardware (in our case the RFSoc) but without absolute power units. By default, the acquired power is displayed in arbitrary units since CASPER supports various boards with different capabilities and the implemented analog stages for these boards have different specifications. Thus, the designer must configure the power conversion factor in the CASPER's interfaces according to the hardware. For completeness, we present the method to characterize the power conversion factor of our design.

In this experiment, we made a frequency sweep of a -10 dBm signal along the RF band (3.1-7.1 GHz) and captured the power at the output of the analog channels and the respective

¹For the analysis of high-order intermodulation products, we rely on the *Spur Calculator* tool provided by Marki Microwave (2023).

read-out in the digital stage. The setup is shown in Fig. 5.8: we used our spectrum analyzer to capture the analog power and *Python* interfaces to capture the digital power read-out.

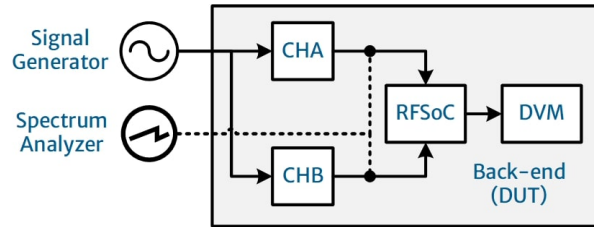


Fig. 5.8: Measurement setup for power calibration.

Then, we analyzed the trend of the curve given by the digital versus analog power to apply linear regression. Fig. 5.9 shows the measured points and the linear fits for both channels.

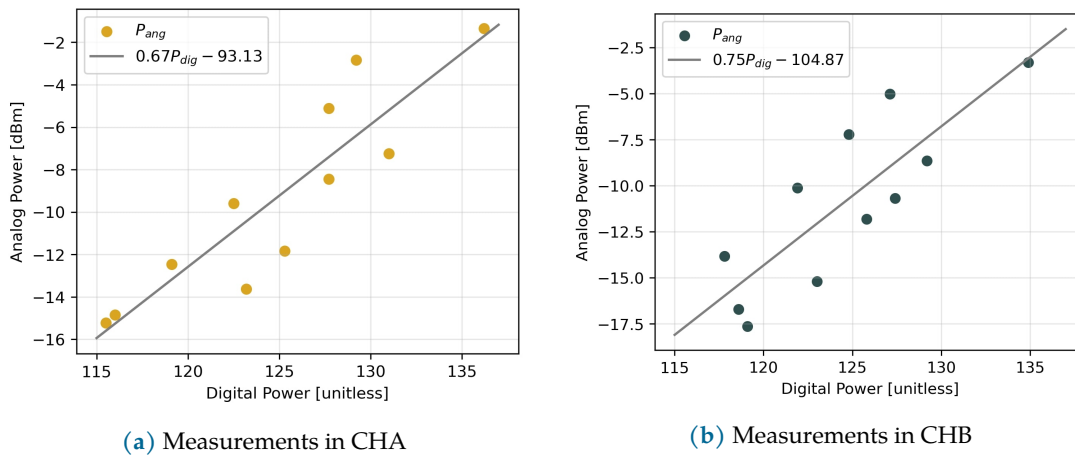


Fig. 5.9: Power calibration for the digital stage.

The lines in Fig. 5.10 are described by the following expressions:

$$\frac{P_{CHA}}{\text{dBm}} = 0.67P_{\text{dig}} - 93.13 ,$$

$$\frac{P_{CHB}}{\text{dBm}} = 0.75P_{\text{dig}} - 104.87 ,$$

so that, the P_{dig} read-out can be converted to dBm. These equations were implemented in Scripts B.6 and B.7 to visualize the acquired spectrum.

5.2.2 Spectral Resolution

The implemented PFB is divided into 64-channels, from which the FFT produces the acquired spectrum.. From Eq. (4.6) we find the spectral resolution $\Delta\nu_{\text{ch}}$ of the instrument is

given by the input bandwidth Δv_{RF} , divided by the number of spectral channels N . The input bandwidth is given by the passband of each channel in the back-end, $\Delta v_{\text{RF}} = 2 \text{ GHz}$, and from the FFT we have $N = 64$. In this way, we reach an ideal spectral resolution of

$$\Delta v_{\text{ch}} = \frac{2 \text{ GHz}}{64} = 31.25 \text{ MHz} .$$

However, (CASPER, 2018d) indicates that the CTF configuration for the RFSoc 2x2 digitally reduces the input spectral window to 1966.08 MHz, which is half of the maximum sampling rate (3932.16 MSPS). Thus, the effective spectral resolution for 64 channels results in

$$\Delta v_{\text{ch}} = 30.72 \text{ MHz} .$$

5.2.3 Spectrum Acquisition and Visualization

As discussed in Section 4.3.1, the Data Visualization and Monitoring stage consists of a PC with the `casperfpga` environment, which contains the interfaces for description and communication with the hardware. Although these interfaces are provided by the CTF, the designer must customize them according to the user needs and the capabilities of the RFSoc. In this sense, we modify the *Python* interfaces that interact with the RFSoc in order to communicate with the board and visualize data on the PC.

The flowchart in Fig. 5.10 describes the process of acquiring and displaying the input spectra with the back-end, and executes as follows:

1. Activate the `casperfpga` environment. Go to the CTF installation folder and run the following in command prompt:

```
» python3.8 -m /cfpga_venv
» source /cfpga_venv/bin/activate
```

Immediately, the virtual environment is created and activated. Here we can implement the CASPER interfaces to communicate with the RFSoc.

2. Run the visualization interface. The Scripts B.6 and B.7 correspond to CHA and CHB interfaces, respectively. Execute the programs by typing the name of the script, the IP address of the board and the acquisition mode (real or complex), e.g.:

```
» python3 rad_CHA.py '192.168.1.4' cx
```

This new sub-process performs the following:

- (a) Reset the PLL reference clocks of the `rfdc` block (uses Script B.8).
- (b) Load the respective fpg images to the board. There is an image for each acquisition mode, real and complex.
- (c) Request and capture the data of the VDA blocks in a variable called `spectrum`.
- (d) Plot `spectrum` versus the bins of the FFT (64-channels). The plot refreshes in approximately one second.

- (e) The script saves the last acquired spectrum in a text file for offline processing.
 - (f) The user can interrupt the acquisition by typing `Ct r l+Z` on the keyboard or closing the plot window.
 - (g) On user interrupts, the system returns to the `casperfpga` environment. Otherwise, the process continues plotting the spectrum.
3. Once the acquisition is interrupted, the user decides whether to execute another acquisition round (e.g., on the other channel). If so, control returns to point (2). If not, the user can deactivate the `casperfpga` environment to finish the overall process by typing
- » deactivate

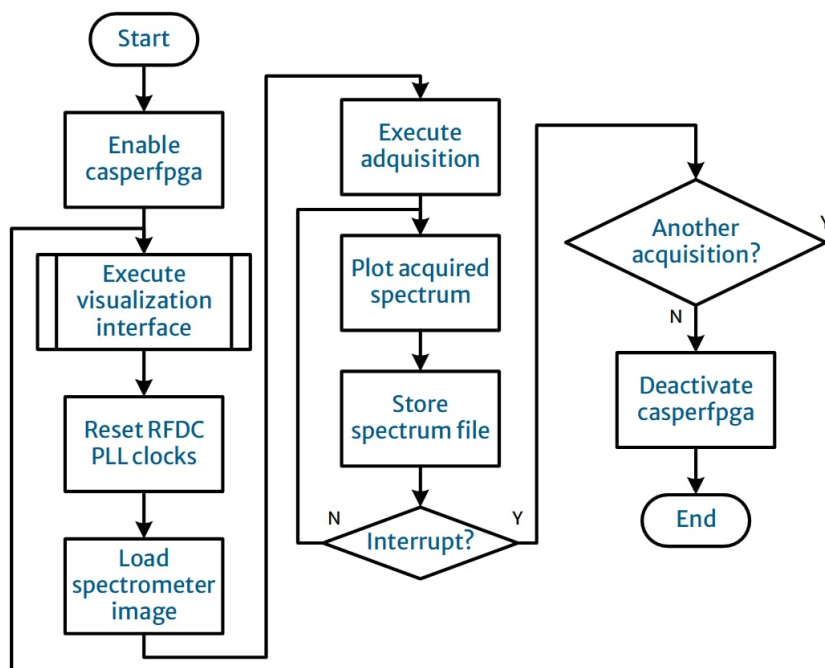


Fig. 5.10: Spectrum acquisition and visualization flowchart.

As a test of the above process, we inject a -20 dBm signal at different frequencies to capture the digital response of the instrument, and as a result we obtain the plots of Fig. 5.11. It can be noted that as we increase the input frequency of CHB, the output is shifted downwards because of the frequency inversion effect. Additionally, power read-out follows the gain curve of Fig. 5.2, and the frequency read-out is shifted because of the width of the bins. The expected IP3 components are also visible in both channels in the presence of the input signal.

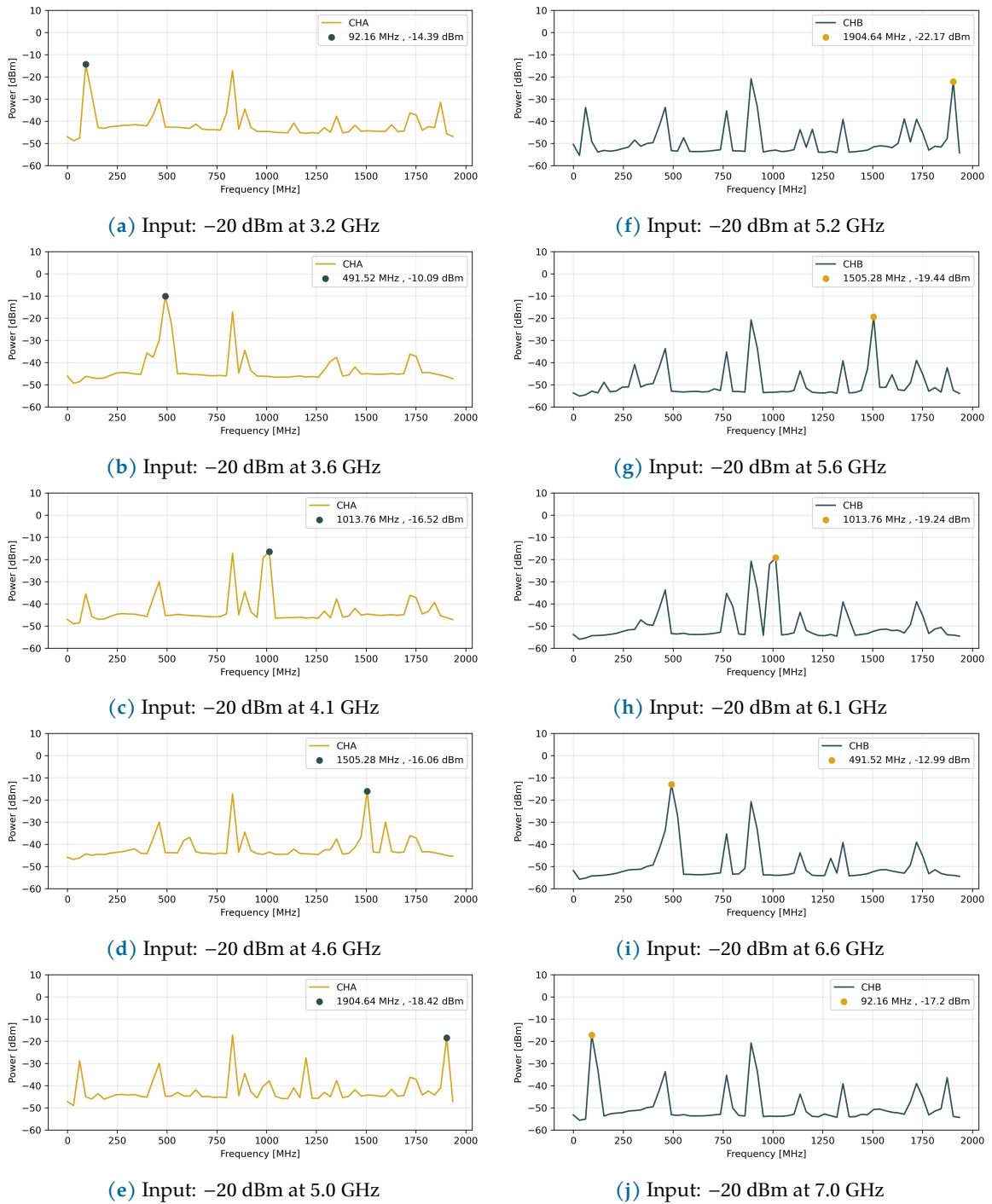


Fig. 5.11: Response spectra in the channels of the back-end.

5.3 Summary

Finally, we summarize the results of each experiment: Table 5.6 presents the main features of the down-conversion stage, and Table 5.7 the main features of the instrument, i.e., the KRx and the back-end connected together.

Table 5.6: Back-end main analog features.

Feature	Value		Units
	CHA	CHB	
RF Band	3.1 - 5.1	5.1 - 3.1	GHz
LO Frequency	3.1	7.1	GHz
IF Band	0 - 2	0 - 2	GHz
Gain ⁺	-9.53	-12.10	dB
Noise Figure ⁺	9.53	12.10	dB
Noise Temperature ⁺	2312	4413	K

⁺ Mean value in the passband.

Table 5.7: Instrument features.

Feature	Value	Units
Radiometric⁺		
Sensitivity	6.5×10^{-3}	K
Gain	32.18	dB
Noise Figure	2.94	dB
Noise Temperature	280.15	K
Spectrometer		
Digital Bandwidth	1966.08	MHz
Spectral Resolution	30.72	MHz
Acquisition Time	40	ms
Consumption		
Input Voltage (AC)	120	V
Power Consumption (AC)	276	W

⁺ For the KRx-Back-end chain.

FINAL DISCUSSION

6.1 Instrument Performance

In the first instance, the prototype acquires and processes the power spectrum using the scheme outlined in Chapter 5. In this chapter, we review the analog and digital behavior we observed during construction and bench testing of the prototype.

From the analog stage we found that:

1. As seen in Section 4.3.2, the down-conversion allows us to cover the 4 GHz bandwidth of the KRx, in two separated channels of 0–2 GHz each. This means that we can adequately retrieve the water vapor profile around 22.235 GHz with our back-end.

- Since the output band of the KRx is 3.1 – 7.1 GHz, the center of the band at $\nu_{\text{RF}} = 5.1$ GHz falls in the upper cutoff of each analog channel. In the case of CHA with $\nu_{\text{LO}} = 3.1$ GHz,

$$\nu_{\text{IF}} = \nu_{\text{RF}} - \nu_{\text{LO}} = (5.1 - 3.1) \text{ GHz} = 2 \text{ GHz} .$$

In the case of CHB with $\nu_{\text{LO}} = 7.1$ GHz,

$$\nu_{\text{IF}} = (5.1 - 7.1) \text{ GHz} = -2 \text{ GHz} ,$$

which is frequency-inverted to $\nu_{\text{IF}} = 2$ GHz.

- By analyzing the down-conversion of the KRx (see Fig. 4.14), we found that the peak of the water vapor line (22.235 GHz) will be processed by CHA at 1.735 GHz. Since we have $\nu_{\text{RF,KRx}} = 22.235$ GHz, and from Table 4.1 we know that $\nu_{\text{LO,KRx}} = 17.4$ GHz, the peak is down-converted to

$$\nu_{\text{IF,KRx}} = (22.235 - 17.4) \text{ GHz} = 4.835 \text{ GHz}$$

at the output of KRx, which is within the CHA input band: for the external down-conversion stage, the input ν_{RF} is the $\nu_{\text{IF,KRx}}$, and converting it with the CHA local oscillator $\nu_{\text{LO}} = 3.1$ GHz we found that

$$\nu_{\text{IF}} = (4.835 - 3.1) \text{ GHz} = 1.735 \text{ GHz}$$

2. From the results of Section 5.1.2 we can conclude that although the down-conversion attenuates the KRx signal, it will be compensated by the +43 dB KRx gain. This means that the overall gains are ~ 33 dB in CHA and ~ 31 dB in CHB because their mean attenuations are -9.53 dB and -12.1 dB, respectively. Using the latter values, we estimate a mean attenuation of -10.8 dB for the back-end system.
3. The net attenuation of the back-end channels we found in Section 5.1.3, causes a high system noise figure and consequently high noise temperature, which is outside the typical values for a good receiver system. However, when connecting the KRx to the system chain, the overall noise temperature is dominated by the KRx since the contribution of the back-end is decreased by the KRx gain (see Eq. (5.4)). Given that the overall noise temperature is $T_{\text{rx}} = 280$ K, we achieve a noise figure $NF_{\text{rx}} = 2.94$ dB.
4. Since the magnitude of the product $\Delta\nu\tau_{\text{obs}}$ is much greater than the term $T_{\text{sky}} + T_{\text{rx}}$ (see Eq. (5.5)), the back-end sensitivity is on the order of 10^{-3} K. This is mainly because of the broad band we use in the analog system. This situation favors the detection of the water vapor line in K-band when changes in PWV occur. As mentioned in Section 1.2.3, changes of 1 mm in PWV lead to a ~ 0.4 K change in brightness temperature. Hence, a high-sensitivity radiometer is required to operate in this band, and our architecture allows us to reach this regime.
5. In a general case, IP3 spurs can be avoided as long as the input signal power to the back-end is low. In our case, the typical input powers are quite low. For instance, a -20 dBm input signal results in IP3 powers of -60 dBm. According to our measurements (see Fig. 5.11), the noise floor of our back-end is approximately -60 dBm, which means that signals with lower powers are not detectable by the system. But in practice we found that despite the low noise floor, spurs are detectable in the system, as in the case of the measurement of Fig. 5.11e: the IP3 spur resulting of a -18 dBm input signal at 5.0 GHz is detected with -27.5 dBm at 1.2 GHz.
6. Judging by the power of the spurs found in Fig. 5.11, none of them seem to belong to the DDC spurs listed in Table 5.3, and perhaps we should not be so concerned about them. According to the manufacturer, typical DDC spur powers are ~ 70 dB weaker than the desired signal power. In this way, a DDC spur becomes significant for our system if we have a 30 dBm input signal because we will have a $(30 - 70)$ dBm = -40 dBm spur power. However, from Fig. 5.7 and Table 5.4 we found that the sampling rate (3932 MHz) and its Nyquist frequency (1966 MHz) causes aliasing of frequencies above 2 GHz coming out of the down-conversion stage, mainly because the cut-off frequency of the LPF is at 2.2 GHz, allowing frequencies above the Nyquist frequency to pass through.
7. Regarding the rest of the spurs, we conclude that the analog channels present reflection from one to another. So that, when reading one of the channels, analog or digitally, the fundamental and harmonics of the local oscillator of the other channel interact in the mixing stage of the channel in operation, causing spurs in this pass-band as high-order intermodulation products. We confirm these leakages in bench tests by measuring the spectra at both outputs of the splitter: we acquired the spectrum of the channel of interest while the LO of the other channel was disconnected and noticed that the spurs in Fig. 5.5 disappeared.

8. We detect, by measuring the CHA spectrum in narrower windows, that spurs 1, 3, and 12 of Table 5.4 are produced analogically, but we have not determined their origin. According to our calculations, they do not belong to either digital or analog intermodulation products. On the other hand, spurs 9, 10 of CHA and 4, 5 of CHB are detected at the same frequencies, and they are the under-sampled signals which come from the analog 2.2 and 2.25 GHz signals of the down-conversion stage. These last two frequencies are aliased into the pass-band because they exceed the Nyquist sampling criterion.
9. It is clearly seen that the analog and digitally-caused spurs reflect into the digital spectrum. First of all, we must attend to and eliminate the spurs coming from the down-conversion stage, and we can implement the solutions mentioned in Section 6.2.

On the other hand, the digital stage presents the following behavior:

1. The power calibration works for the purpose of this work. However, another method must be implemented to improve accuracy in measurements. The equations that we found in Section 5.2.1, which describe the analog power as function of the digital power, present standard errors of the estimated slope of $\sigma_{\text{CHA}} = 0.1093$ and $\sigma_{\text{CHB}} = 0.1682$ for channels A and B, respectively.
2. From Fig. 5.11 we found that the digital power read-out follows the behavior of the analog gain in the pass-band of the channels. Hence, this gain curve must be accounted for in the digital acquisition.
3. The design of the spectrometer we discussed in Section 4.3.4 allows us to digitize the 1966 MHz input bandwidth into 64 bins (digital channels) of 30.72 GHz each. Even using this reduced bandwidth, we can still characterize the line profile using the method presented in Section 4.1.3.
4. The acquisition process discussed in Section 5.2.3 allows us to visualize and store the spectral data in real time. In this way, we maintain the interaction with the user and open the possibility of post-acquisition data processing. By placing flags in the processing algorithm, we found that it takes ~ 20 ms to sample the spectrum over the entire bandwidth of a single channel. This means that we can sequentially acquire the 4 GHz KRx band in ~ 40 ms. This acquisition time is still within the time stability of the atmospheric water vapor we discuss at the end of Section 4.1.2.
5. The acquisition algorithms (Scripts B.6 and B.7) provide the data as a text file when the acquisition is done. This allows the user to apply post-processing algorithms for data reduction, analysis and calibration. In our case, we can implement the water vapor profile reconstruction (see Section 4.1.3) or a PWV retrieval algorithm (see Section 3.4) once a radiometer calibration method is implemented.

Regarding the atmospheric characterization at remote sites:

1. According to values of Table 4.11, we estimate a total AC power consumption of 276 W for the back-end. Although this consumption is acceptable under laboratory conditions, it is excessive for remote site conditions.

2. The power consumption of the back-end should be minimized. The AC power consumption may be reduced if we implement other power sources with higher efficiency. We cannot reduce the DC power consumption since the power sources MS1 and MS2 fit the requirements of their respective devices. Moreover, it is not possible to significantly reduce AC consumption by more than 30% because MS1 fits the power requirements of the RFSoc board and represents 70% of the total AC power consumption of the prototype.
3. For both established and remote sites, there must be implemented a discharge protection stage. We suggest to connect MS1 and MS2 to a protected AC power source to avoid electrical discharges and even noise interferences in the power line.
4. Regardless of the area assigned for monitoring, a radiation-isolating enclosure should be implemented to prevent external radio interference from entering the back-end and the same radiation from the back-end from affecting other surrounding devices.

The overall architecture of the prototype provides several capabilities such as scalability and customization for other purposes:

- With respect to the digital implementation of the spectrometer, the width of each PFB band-pass filter and the size of the FFT can be modified at the designer's discretion when programming the FPGA. This suggests that other approaches can be implemented in the prototype, e.g., observation of spectral lines with high resolution using a balance between the number of channels and the total bandwidth. Taking the work of [González \(2019\)](#) or [Contreras \(2023\)](#) as a reference, our RFSoc may involve many improvements given its state-of-the-art performance.
- The use of CASPER tools and the RFSoc allowed us to save significant time in developing the platform. Nevertheless, the CASPER blocks and their interfaces only achieve maximum spectral resolutions of $\Delta v_{\text{ch}} = 960$ kHz and $\Delta v_{\text{ch}} = 480$ kHz for bandwidths of $\Delta v = 1966.08$ MHz and $\Delta v = 983.04$ MHz, respectively, which represent the maximum input bandwidth. The designer must consider these limitations when implementing the back-end as a spectral-line receiver, and there must be a balance to achieve good spectral resolution without compromising SNR.
- Our digital architecture may partially cover the need of [Márquez-Méndez \(in prep\)](#) and [Rojas-Méndez \(in prep\)](#) work for water vapor radiometry in radio interferometers since our RFSoc 2x2 scheme (see Fig. C.1) is scalable to the 4x2 board version. It is important to mention that the 4x2 version can cover 4 GHz per channel, doubling the analog capabilities of the 2x2 board.

Leaving aside the spurs found, the radiometer proves to be an attractive, versatile and low-cost solution for water vapor radiometry at radio astronomical observatories. The current capabilities are sufficient for basic operation: the instrument is efficient under laboratory conditions, similar to the Tulancingo-I station.

Due to the hardware limitations of the prototype, we conclude that this instrument is not physically suitable for commissioning at remote sites because improvement of several capabilities would be needed for such sites like the ngVLA locations in Northern Mexico. However, the conceptual design of our instrument can be directly implemented for remote site instrument proposals, such as presented by Rojas-Méndez (in prep). For this particular case (see Fig. 6.1), one of the outputs of their front-end can be analogically conditioned to be acquired by our RFSoc.

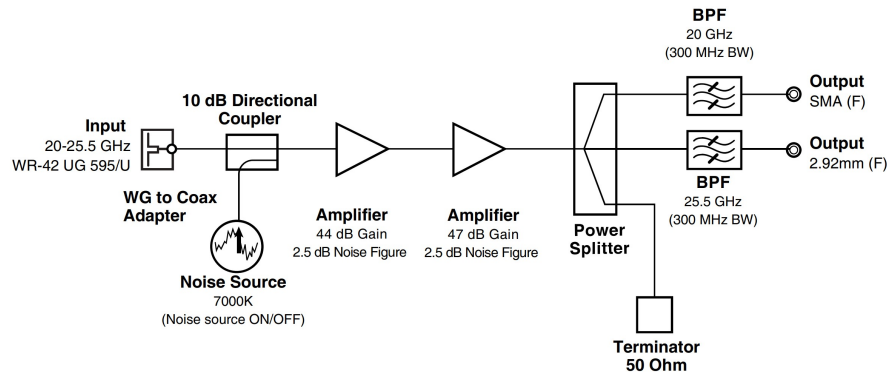


Fig. 6.1: Schematics of the water vapor radiometer designed by Rojas-Méndez (in prep).

6.2 Future Work

At this time, the prototype has shown good performance in bench tests, and both the acquisition and processing algorithms recover the KRx band as expected. Before testing the instrument at Tulancingo, some hardware and digital processing details must be attended to in the prototype.

Analog spurs must be removed to clean the acquired spectrum. There are various ways to solve this issue, such as isolators at both outputs of the splitter, but to completely avoid the reflection in the channels we suggest changing from a splitter to a mechanical switch. This would ensure that only one electrical path is acquired at a time, avoiding leakage from the other channel. Of course, this will require the implementation of an extra control script for switching between channels. As an alternative, we can filter and reduce the output bandwidth of the KRx, which would require a re-design of the analog architecture of the prototype. In this way, we would be able to avoid most of the spurs reported in Section 5.1.5.

In order to commission the back-end at Tulancingo, we intend to place the back-end board, power supplies and receptacles in a box-type enclosure. Given the physical dimensions of the back-end, all devices will fit into a standard 19-inch rack mount enclosure. Additionally, the use of our back-end in Tulancingo will save us the need to build a pointing system to perform the tip-scan, and the connection of communication systems, since this facility has the necessary infrastructure for this purpose.

The gain curve of the down-conversion stage in the current acquisition algorithm must be incorporated in the analysis. Then, radiometric calibration of the instrument must be performed to have correct measurements and to properly implement the retrieval algorithms. After that, we will use the method discussed in Section 3.4 to retrieve the PWV from the obtained zenith opacity.

Moreover, although the acquisition process allows us to visualize and store the spectral data in real time, the process is done manually. We also intend to implement scripts commanded by a background process (so-called *daemon software*) to completely control the RF-SoC with the host computer.

The main benefit of testing our back-end at Tulancingo is to evaluate the hardware, processing, control and performance. This consequently will ensure the overall functionality of the prototype and will validate the retrieval algorithms under observatory conditions.

In the long-term, we intend to perform continuum and spectral-line observations in the 20.5 - 24.5 GHz band to evaluate the behavior and capabilities of the back-end as a radio astronomical receiver. First we need to have a particular use case to modify the digital architecture and adapt it to the observational needs and scientific purposes for observing in this band. This, of course, will provide an extra capability to the instrument. In other words, we could use the instrument as a water vapor radiometer and as an astronomical receiver: the former providing the atmospheric opacity and the latter making astronomical observations with the corrected attenuation. This means a saving in the construction of two instruments to only one and also the versatility of having accurate astronomical observations in real time.

6.3 Scientific Products

A secondary approach to the prototype was presented in poster mode at the *LXVI Congreso Nacional de Física 2023* in Morelia, Mexico: this work focused on the implementation of the PYNQ scheme (mentioned in Section 4.3.3) and also our analog back-end at the bench test level.

In the poster we evaluate the behavior of our proposed back-end with the PYNQ platform, which is based on a browser computing environment. A spectrum analyzer was implemented in this environment to measure and visualize the power of artificially generated signals. PYNQ provides an intuitive graphical interface, high-resolution and modification of the spectrum analyzer controls in real time. We found that, despite these features, the web platform does not allow a level of code customization or transfer of raw data for post-acquisition processing. Although the approach was functional, and proved to be an option for radiometry, we would be limited to capturing spectral data manually. See the poster in Fig. 6.2.



RFSoc-based digital back-end for water vapor radiometry at radio observatories

Jetzael Cuazon¹, Stan Kurtz¹, Daniel Ferrusca²
¹ Institute of Radio Astronomy and Astrophysics
² National Institute of Astrophysics, Optics and Electronics



- Water vapor is one of the main atmospheric constituent affecting radio wave propagation (see Fig. 1), and it must be characterized for atmospheric corrections in regard to radio astronomy observations.
- A microwave radiometer is an effective and versatile solution to monitor and characterize the water vapor content in the atmosphere.
- The sky characterization using radiometers helps to evaluate the short and long-term atmospheric variations.
- We present an FPGA-based back-end for K-band water vapor radiometry for radio astronomy observatories.
- The instrument measures the power spectrum of the receiver signal, from which several retrieval methods can be implemented to estimate the zenith opacity and precipitable water vapor (PWV).
- The system architecture (see Fig. 2) consists of an analog Down-Conversion stage, a Digitization system, and the Data Visualization and Monitoring (DVM) environment.
- The prototype is shown in Fig. 3: the analog system is made of Mini-Circuits® devices, and the digitization stage is based on the RFSoc 2x2 platform developed by HiTech Global® and supported by Xilinx®.
- We perform a bench test to evaluate the functionality of the instrument using the measured power spectrum (see Fig. 4): an artificially generated signal was injected to the back-end in order to estimate the system gain and validate the frequency conversion of the analog stage.

Summary

- The **prototype** acquires and **processes** the **power spectrum adequately** so that **retrieval algorithms** for **opacity** and **PWV** can be **implemented**.
- We estimate a **gain of 20 dB** for the **back-end** chain. Following technical reports of the K-band receiver, the entire **system gain** results in **63 dB**.
- Given its **programming versatility**, the **instrument** can also be used for **continuum** or **spectral line** radio astronomical **observations** by **implementing** other **FPGA description schemes**.
- The instrument is an **attractive option** for **atmospheric characterization** at **astronomical sites**, for both short and long-term evaluation.
- Field tests must be performed** to ensure the correct **functionality** of the instrument, as well as the **validation of the retrieval algorithms** under **real conditions**.
- PYNQ** is a **viable solution** for signal processing, but **we intend to implement** other description **environments** that **will allow further customization** of the prototype.

Further information:



Contact:

j.cuazon@irya.unam.mx

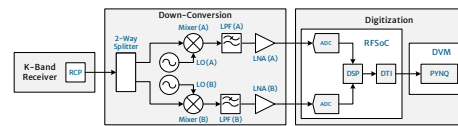


Fig. 2: Radiometer architecture.

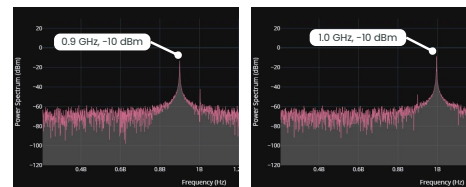


Fig. 4: Power spectra measured in bench test. Left: The input 4.1 GHz signal translates to 1 GHz since the local oscillator frequency was 3.1 GHz. Right: The input 6.0 GHz signal translates to 0.9 GHz for a 5.1 GHz local oscillator.

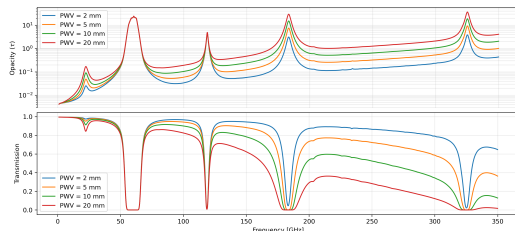


Fig. 1: Atmospheric opacity (top) and transmission (bottom) for different values of PWV at an arbitrary central Mexico site.

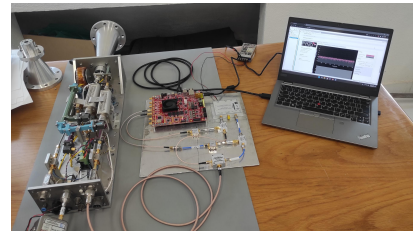


Fig. 3: Bench test setup: K-band radiometer (left), back-end(center), and the DVM (right)

Fig. 6.2: Poster presented at the LXVI CNF.

REFERENCES

- Backes, M., et al. (2017). The African Millimetre Telescope. *Proceedings of Science, HEASA 2016*, 029, <https://doi.org/10.22323/1.275.0029>.
- Behrens, M. T. & Stander, T. (2020). Preliminary design of a dual 22/31 GHz single-chip water vapour radiometer. *Ground-based and Airborne Telescopes VIII*, 11445, <https://doi.org/10.1117/12.2561999>.
- Bevis, M., Businger, S., Herring, T., Rocken, C., Anthes, R., & Ware, R. (1992). GPS Meteorology: Remote Sensing of Atmospheric Water Vapor Using the Global Positioning System. *Journal of Geophysical Research*, 97, <https://doi.org/10.1029/92JD01517>.
- Burke, B. F., Graham-Smith, F., & Wilkinson, P. N. (2019). *An Introduction to Radio Astronomy*. Cambridge University Press, 4th edition.
- Carramiñana, A. (2016). *Sierra Negra: the Site of the Large Millimetre Telescope Alfonso Serrano*, (pp. 69–79). United Nations Educational, Scientific and Cultural Organization.
- CASA (2021). CASA Tools API: atmpsphere. <https://casadocs.readthedocs.io/en/v6.5.3/api/tt/casatools.atmosphere.html#casatools.atmosphere>.
- CASA (2023). CASA Releases. https://casa.nrao.edu/casa_obtaining.shtml.
- CASPER (2018a). (a) CASPER: The Collaboration for Astronomy Signal Processing and Electronics Research. <https://casper.berkeley.edu/>.
- CASPER (2018b). (b) CASPER Toolflow. <https://casper-toolflow.readthedocs.io/en/latest/>.
- CASPER (2018c). (c) Installing the Toolflow. <https://casper-toolflow.readthedocs.io/en/latest/src/Installing-the-Toolflow.html>.
- CASPER (2018d). (d) Tutorial 3: Example Spectrometer. https://casper-toolflow.readthedocs.io/projects/tutorials/en/latest/tutorials/rfsoc/tut_spec.html.
- Cernicharo, J. (2014). *Water, Vibrational and Rotational Transitions*, (pp. 1–4). Springer.
- Condon, J. J. & Ransom, S. M. (2016). *Essential Radio Astronomy*. Princeton University Press.
- Contreras, L. P. (2023). A 22 GHz Pseudo-correlation Water Vapor Radiometer. Master's thesis, Universidad de Concepción.

- Corlay, G., Arnolfo, M.-C., Bret-Dibat, T., Lifferman, A., & Pelon, J. (2017). The infrared imaging radiometer for PICASSO-CENA. *International Conference on Space Optics — ICSSO 2000*, 10569, 105690O, <https://doi.org/10.1117/12.2307903>.
- Crockett, L., Northcote, D., & Stewart, R. W. (2023). *Software Defined Radio with Zynq Ultra-Scale+ RFSoc*. Strathclyde Academic Media, 1 edition.
- Cruz-Pol, S. L., Ruf, C. S., & Keihm, S. J. (1998). Improved 20- to 32-GHz atmospheric absorption model. *Radio Science*, 33(5), 1319–1333, <https://doi.org/10.1029/98RS01941>.
- Cuazon, J., Ferrusca, D., Contreras, J., Ibarra-Medel, E., Velázquez, M., Kurtz, S., & Hiriart, D. (2021). Single-Board Computer based Architecture and Firmware for Radiometers with Radio Astronomy applications. *2021 18th International Conference on Electrical Engineering, Computing Science and Automatic Control (CCE)*, (pp. 1–6)., <https://doi.org/10.1109/CCE53527.2021.9633063>.
- Denisowski, P. (2023). Understanding basic spectrum analyzer operation. https://www.rohde-schwarz.com/us/products/test-and-measurement/essentials-test-equipment/spectrum-analyzers/understanding-basic-spectrum-analyzer-operation_256005.html.
- Dicke, R. H. (1946). The Measurement of Thermal Radiation at Microwave Frequencies. *Review of Scientific Instruments*, 17(7), 268–275, <https://doi.org/10.1063/1.1770483>.
- Dicke, R. H., Beringer, R., Kyhl, R. L., & Vane, A. B. (1946). Atmospheric Absorption Measurements with a Microwave Radiometer. *Phys. Rev.*, 70, 340–348, <https://doi.org/10.1103/PhysRev.70.340>.
- Elsässer, H. (2004). *An Inter-African Astronomical Observatory and Science Park on the Gamsberg in Namibia?*, (pp. 195–201). Springer Netherlands.
- England, M. N., Ferrare, R. A., Melfi, S. H., Whiteman, D. N., & Clark, T. A. (1992). Atmospheric water vapor measurements: Comparison of microwave radiometry and lidar. *Journal of Geophysical Research: Atmospheres*, 97(D1), 899–916, <https://doi.org/10.1029/91JD02384>.
- Ferrusca, D. & Contreras, J. (2014). Weather monitor station and 225 GHz radiometer system installed at Sierra Negra: the Large Millimeter Telescope site. *Ground-based and Airborne Instrumentation for Astronomy V*, 9147, 914730, <https://doi.org/10.1117/12.2055005>.
- Ferrusca, D., Contreras, J., Cuazon, J., Hiriart, D., Ibarra-Medel, E., Kurtz, S., Rojas, D., & Velázquez, M. (2022). A review of the atmospheric opacity at the Large Millimeter Telescope site and 210 GHz opacity measurements comparison. *Ground-based and Airborne Telescopes IX*, 12182, 121824F, <https://doi.org/10.1117/12.2629610>.
- Ferrusca, D., Cuazon, J., Contreras, J., Hiriart, D., Ibarra, E., Kurtz, S., Stander, T., & Velázquez, M. (2020). Embedded system upgrade based on Raspberry Pi computer for a 23/31 GHz dual-channel water vapor radiometer. *Ground-based and Airborne Telescopes VIII*, 11445, <https://doi.org/10.1117/12.2561733>.

-
- Frans, L. N. (2020). Determination of the suitability of MT Gamsberg in Namibia for millimetre wave astronomy by measurements of the precipitable water vapour. Master's thesis, University of Namibia.
- Fujisawa, K., et al. (2022). The Yamaguchi Interferometer. *Publications of the Astronomical Society of Japan*, 74(6), 1415–1420, <https://doi.org/10.1093/pasj/psac078>.
- Gaut, N. E. (1968). *Studies of atmospheric water vapor by means of passive microwave techniques*. Technical report, Massachusetts Institute of Technology.
- González, D. J. D. (2019). Implementación de un espectrómetro de alta resolución. Master's thesis, Universidad Nacional Autónoma de México.
- Granato, F. (2010). Transparency of the atmosphere. https://www.eso.org/public/images/atm_opacity/.
- Groumpas, E., Koutsoupidou, M., Karanasiou, I. S., Papageorgiou, C., & Uzunoglu, N. (2020). Real-Time Passive Brain Monitoring System Using Near-Field Microwave Radiometry. *IEEE Transactions on Biomedical Engineering*, 67(1), 158–165, <https://doi.org/10.1109/TBME.2019.2909994>.
- Guiraud, F. O., Howard, J., & Hogg, D. C. (1979). A Dual-Channel Microwave Radiometer for Measurement of Precipitable Water Vapor and Liquid. *IEEE Transactions on Geoscience Electronics*, 17(4), 129–136, <https://doi.org/10.1109/TGE.1979.294639>.
- Gustrau, F. (2012). *RF and Microwave Engineering: Fundamentals of Wireless Communications*. Wiley, 1 edition.
- Gutiérrez-Guzmán, U. N., Castellanos-Perez, E., Serrato-Corona, J. S., Martínez-Ríos, J. J., & Chairez-Hernández, I. (2017). Satellite and field radiometry for the estimation of biomass production in a grassland site in state of Durango, Mexico. *Range Management and Agroforestry*, (pp. 158–164).
- Haefele, A. & Kämpfer, N. (2010). Tropospheric Water Vapor Profiles Retrieved from Pressure-Broadened Emission Spectra at 22 GHz. *Journal of Atmospheric and Oceanic Technology*, 27(1), 167 – 172, <https://doi.org/10.1175/2009JTECHA1334.1>.
- Han, Y. & Westwater, E. (2000). Analysis and improvement of tipping calibration for ground-based microwave radiometers. *IEEE Transactions on Geoscience and Remote Sensing*, 38(3), 1260–1276, <https://doi.org/10.1109/36.843018>.
- Hickish, J., et al. (2016). A Decade of Developing Radio-Astronomy Instrumentation using CASPER Open-Source Technology. *Journal of Astronomical Instrumentation*, 5(4), <https://doi.org/10.1142/S2251171716410014>.
- Hills, R. & Richer, J. (2000). ALMA Memo 303 Water Vapour Radiometers for ALMA. <https://library.nrao.edu/public/memos/alma/main/memo303.pdf>.
- Hiriart, D. & Rojas, J. D. (2023). *HartRAO dual frequency radiometer data pipeline*. Technical report, Instituto de Astronomía UNAM.

- Hogg, D. C., Guiraud, F. O., & Sweezy, W. B. (1981). The Short-Term Temporal Spectrum of Precipitable Water Vapor. *Science*, 213(4512), 1112–1113, <https://doi.org/10.1126/science.213.4512.1112>.
- Ibarra-Medel, E., Velázquez, M., Ferrusca, D., & Kurtz, S. (2022). Design and construction of a Low-Noise L-Band Amplifier for the Tulancingo I radio Telescope. In *2022 IEEE Latin American Electron Devices Conference (LAEDC)* (pp. 1–4).
- Indermuhle, B. T., Burton, M. G., & Crofts, J. (2013). Water Vapour Radiometers for the Australia Telescope Compact Array. *Publications of the Astronomical Society of Australia*, 30, e035, <https://doi.org/10.1017/pas.2013.013>.
- Janssen, M. A. (1993). *Atmospheric remote sensing by microwave radiometry*. Wiley.
- Kämpfer, N., Nedoluha, G., Haefele, A., & Wachter, E. D. (2013). *Monitoring Atmospheric Water Vapour: Ground-Based Remote Sensing and In-situ Methods*, volume 10. Springer.
- Karmakar, P. K. (2012). *Microwave Propagation and Remote Sensing: Atmospheric Influences with Models and Applications*. CRC Press.
- Karmakar, P. K. (2014). *Ground-Based Microwave Radiometry and Remote Sensing: Methods and Applications*. CRC Press.
- Kurtz, S. E., Taylor, A. C., Jones, M. E., Gale, D. M., Ibarra Medel, E., Pollak, A., & Liu, C. (2022). A born again 32-meter radio telescope for Mexico. In H. K. Marshall, J. Spyromilio, & T. Usuda (Eds.), *Ground-based and Airborne Telescopes IX*, volume 12182 of *Society of Photo-Optical Instrumentation Engineers (SPIE) Conference Series* (pp. 121822T).
- Liljegren, J. C. (2002). Studies of atmospheric water vapor by means of passive microwave techniques. https://radiometrics.com/wp-content/uploads/2021/10/mwrp_handbook.pdf.
- Lin, X. (2018). SLAA824: Spurs Analysis in the RF Sampling ADC. <https://www.ti.com/lit/an/slaa824/slaa824.pdf>.
- Liu, Q. M., Cao, C., Grassotti, C., & Lee, Y.-K. (2021). How Can Microwave Observations at 23.8 GHz Help in Acquiring Water Vapor in the Atmosphere over Land? *Remote Sensing*, 13(3), <https://doi.org/10.3390/rs13030489>.
- Lutz, R., Wilheit, T., Wang, J., & Kakar, R. (1991). Retrieval of atmospheric water vapor profiles using radiometric measurements at 183 and 90 GHz. *IEEE Transactions on Geoscience and Remote Sensing*, 29(4), 602–609, <https://doi.org/10.1109/36.135822>.
- Marki Microwave (2023). Technical Resources: Spur Calculator. <https://markimicrowave.com/technical-resources/tools/spur-calculator/>.
- Marr, J. M., Snell, R. N., & Kurtz, S. E. (2016). *Fundamentals of Radio Astronomy: Observational Methods*. CRC Press.
- Marvil, J. (2010). EVLA Memo 143: Improving the frequency resolution of the default atmospheric opacity model. https://library.nrao.edu/public/memos/evla/EVLAM_143.pdf.

-
- Matlab (2022). Matlab R2022b Documentation: Evaluating Goodness of Fit. <https://www.mathworks.com/help/curvefit/evaluating-goodness-of-fit.html>.
- Miacci, M. & Angelis, C. F. (2018). Ground-Based Microwave Radiometer Calibration: an Overview. *Journal of Aerospace Technology and Management*, 10, <https://doi.org/10.5028/jatm.v10.927>.
- Mini-Circuits (2023a). (a) ZFRSC-123-S+ Coaxial Power Splitter/Combiner. <https://www.minicircuits.com/pdfs/ZFRSC-123-S+.pdf>.
- Mini-Circuits (2023b). (b) ZMX-10G Coaxial Frequency Mixer. <https://www.minicircuits.com/pdfs/ZMX-10G.pdf>.
- Mini-Circuits (2023c). (c) VLF-2250 Coaxial Low Pass Filter. <https://www.minicircuits.com/pdfs/VLF-2250.pdf>.
- Mini-Circuits (2023d). (d) ZX60-P33ULN+ Coaxial Low Noise Amplifier. <https://www.minicircuits.com/pdfs/ZX60-P33ULN+.pdf>.
- Mini-Circuits (2023e). (e) ZX90-2-24+ Coaxial X2 Frequency Multiplier. <https://www.minicircuits.com/pdfs/ZX90-2-24+.pdf>.
- Mini-Circuits (2023f). (f) ZX60-83LN-S+ Coaxial Low Noise Amplifier. <https://www.minicircuits.com/pdfs/ZX60-83LN-S+.pdf>.
- Márquez-Méndez, I. F. (in prep.). Un radio interferómetro para medir retardos de fase de señales que se propagan en la atmósfera. Master's thesis, Instituto de Astronomía UNAM.
- Nagasaki, T., Araki, K., Ishimoto, H., Kominami, K., & Tajima, O. (2016). Monitoring System for Atmospheric Water Vapor with a Ground-Based Multi-Band Radiometer: Meteorological Application of Radio Astronomy Technologies. *Journal of Low Temperature Physics*, 184(3-4), 674–679, <https://doi.org/10.1007/s10909-015-1412-9>.
- Neufeld, D. A., Wu, Y., Kraus, A., Menten, K. M., Tolls, V., Melnick, G. J., & Nagy, Z. (2013). Herschel*/hifi observations of a new interstellar water maser: The 532–441 transition at 620.701 ghz. *The Astrophysical Journal*, 769(1), 48, <https://doi.org/10.1088/0004-637X/769/1/48>.
- ngVLA (2023). The Next Generation Very Large Array. <https://ngvla.nrao.edu/>.
- OnSemi (2021). LM317 Voltage Regulator – Adjustable Output. <https://www.onsemi.com/download/data-sheet/pdf/lm317-d.pdf>.
- OnSemi (2022). LM2596 Step-Down Switching Regulator. <https://www.onsemi.com/pdf/datasheet/lm2596-d.pdf>.
- Otárola, A., Breuck, C. D., Travouillon, T., Matsushita, S., Nyman, L. A., Wootten, A., Radford, S. J. E., Sarazin, M., Kerber, F., & Pérez-Beaupuits, J. P. (2019). Precipitable Water Vapor, Temperature, and Wind Statistics At Sites Suitable for mm and Submm Wavelength Astronomy in Northern Chile. *Publications of the Astronomical Society of the Pacific*, 131(998), 045001, <https://doi.org/10.1088/1538-3873/aafb78>.

- Otárola, A., Hiriart, D., & Pérez-León, J. E. (2009). Statistical Characterization of Precipitable Water Vapor at San Pedro Martir Sierra in Baja California. *Revista Mexicana de Astronomía y Astrofísica*, 45(2), 161–169.
- Paine, S. (2022). The am atmospheric model. <https://doi.org/10.5281/zenodo.6774376>.
- Pardo, J., Cernicharo, J., & Serabyn, E. (2001). Atmospheric transmission at microwaves (ATM): an improved model for millimeter/submillimeter applications. *IEEE Transactions on Antennas and Propagation*, 49(12), 1683–1694, <https://doi.org/10.1109/8.982447>.
- Pazmany, A. L. (2007). A Compact 183-GHz Radiometer for Water Vapor and Liquid Water Sensing. *IEEE Transactions on Geoscience and Remote Sensing*, 45(7), 2202–2206, <https://doi.org/10.1109/TGRS.2006.888104>.
- Pozar, D. M. (2011). *Microwave Engineering*. Wiley, 4th edition.
- Proakis, J. G. & Manolakis, D. G. (2006). *Digital Signal Processing : Principles, Algorithms, and Applications*. Prentice Hall international editions. Prentice-Hall, 4 edition.
- PYNQ Project (2023). RFSoc 2x2 Overview. http://www.rfsoc-pynq.io/rfsoc_2x2_overview.html.
- Reeve, W. D. (2014). Noise Tutorial Part VI: Noise Measurements with a Spectrum Analyzer. https://reeve.com/Documents/Noise/Reeve_Noise_6_NFMeasSpecAnalyz.pdf.
- Ricaud, P., Gabard, B., Derrien, S., Chaboureau, J.-P., Rose, T., Mombauer, A., & Czekala, H. (2010). HAMSTRAD-Tropo, A 183-GHz Radiometer Dedicated to Sound Tropospheric Water Vapor Over Concordia Station, Antarctica. *IEEE Transactions on Geoscience and Remote Sensing*, 48(3), 1365–1380, <https://doi.org/10.1109/TGRS.2009.2029345>.
- Rojas-Méndez, J. D. (in prep.). *Desarrollo de un receptor en banda K para determinar el retardo de fase en ondas de radio*. PhD thesis, Instituto de Astronomía UNAM.
- Rosenkranz, P. W. (1998). Water vapor microwave continuum absorption: A comparison of measurements and models. *Radio Science*, 33(4), 919–928, <https://doi.org/10.1029/98RS01182>.
- Sarazin, M. (1995). Astroclimatology of Gamsberg, Namibia. <https://www.eso.org/gen-fac/pubs/astclim/espas/gamsberg/>.
- Schilling, G. (2017). The Incredible Skies of Namibia. <https://skyandtelescope.org/astronomy-news/people-places-and-events/incredible-skies-namibia/>.
- Schnitt, S., Lönert, U., & Preusker, R. (2020). Potential of Dual-Frequency Radar and Microwave Radiometer Synergy for Water Vapor Profiling in the Cloudy Trade Wind Environment. *Journal of Atmospheric and Oceanic Technology*, 37(11), 1973 – 1986, <https://doi.org/10.1175/JTECH-D-19-0110.1>.
- Sholley, M., et al. (2003). 183-GHz InP MMIC based radiometer. *Millimeter and Submillimeter Detectors for Astronomy*, 4855, <https://doi.org/10.1117/12.459200>.

-
- Skou, N. & Vine, D. L. (2006). *Microwave Radiometer Systems: Design and Analysis*. Artech House, 2nd edition.
- Solheim, F., Godwin, J. R., Westwater, E. R., Han, Y., Keihm, S. J., Marsh, K., & Ware, R. (1998). Radiometric profiling of temperature, water vapor and cloud liquid water using various inversion methods. *Radio Science*, 33(2), 393–404, <https://doi.org/10.1029/97RS03656>.
- Stander, T. (2021). *HartRAO K-Band Receiver: Preliminary Measurements and Upgrade Planning*. Technical report, University of Pretoria.
- Stander, T., Villiers, D. I. L. d., Witt, A. d., Rodríguez, D. F., Hiriart, D., Kurtz, S. E., Heever, F. v. D., & Becerra, M. V. d. L. R. (2022). A Retrospective of the SA-Mexico Bilateral Programme on Water Vapour Radiometry. In *2022 International Conference on Electromagnetics in Advanced Applications (ICEAA)* (pp. 282–286).
- Suparta, W., Alauddin, M., Ali, M., Yatim, B., & Misran, N. (2007). Remote Sensing of Antarctic Atmospheric Water Vapour using Ground-Based GPS Meteorology. In *2007 5th Student Conference on Research and Development* (pp. 1–8).
- TDK-Lambda (2023). Single Output General Purpose Power Supplies. https://product.tdk.com/system/files/dam/doc/product/power/switching-power/ac-dc-converter/catalog/ls25-150_e.pdf.
- Thompson, A. R., Moran, J. M., & Jr., G. W. S. (2017). *Interferometry and Synthesis in Radio Astronomy*. Astronomy and Astrophysics Library. Springer, 3 edition.
- Torres, V., Davydova, V., Carrasco, L., & Guzmán, I. (1997). *Technical Report LMT-97-18: Evaluation of the long term behavior of sites for mm-wavelength radio-astronomy: the quest for a site for the Large Millimetre Telescope*. . Technical report, National Institute of Astrophysics, Optics and Electronics.
- Ulaby, F. T. & Long, D. G. (2014). *Microwave Radar and Radiometric Remote Sensing*. The University of Michigan Press.
- Valon Technology (2020). 6GHZ DUAL FREQUENCY SYNTHESIZER MODULE. https://www.valonrf.com/uploads/1/1/7/3/117370920/5009_datasheet_v1_4_20211004_ljr.pdf.
- Velázquez, M., Ibarra-Medel, E., Villiers, D. D., Ferrusca, D., Gale, D. M., Hiriart, D., Huerta, A. L., Kurtz, S. E., Rojas, D., & Stander, T. (2022). Optical characterization of the Tulancingo-I radio telescope and site: the potential for K-band operation. In H. K. Marshall, J. Spyromilio, & T. Usuda (Eds.), *Ground-based and Airborne Telescopes IX*, volume 12182 (pp. 121822U).: International Society for Optics and Photonics SPIE.
- Wang, J., Sun, C., Wang, G., Zou, M., Tan, T., Liu, K., Chen, W., & Gao, X. (2020). A fibered near-infrared laser heterodyne radiometer for simultaneous remote sensing of atmospheric CO₂ and CH₄. *Optics and Lasers in Engineering*, 129, <https://doi.org/10.1016/j.optlaseng.2020.106083>.

- Wang, J. R., Wilheit, T. T., & Chang, L. A. (1989). Retrieval of Total Precipitable Water Using Radiometric Measurements Near 92 and 183 GHz. *Journal of Applied Meteorology* (1988-2005), 28(2), 146–154, [https://doi.org/10.1175/1520-0450\(1989\)028<0146:R0TPWU>2.0.CO;2](https://doi.org/10.1175/1520-0450(1989)028<0146:R0TPWU>2.0.CO;2).
- Westwater, E. (1978). The accuracy of water vapor and cloud liquid determination by dual-frequency ground-based microwave radiometry. *URSI Radio Science Bulletin*, 13(4), 677–685, <https://doi.org/10.23919/URSIRSB.2004.7909438>.
- Westwater, E., Crewell, S., & Mätzler, C. (2004). A review of surface-based microwave and millimeter-wave radiometric remote sensing of the troposphere. *URSI Radio Science Bulletin*, 2004(310), 59–80, <https://doi.org/10.23919/URSIRSB.2004.7909438>.
- Wiederhold, P. R. (1997). *Water Vapor Measurement: Methods and Instrumentation*. CRC Press.
- Wiedner, M. C. (1998). *Atmospheric Water Vapour and Astronomical Millimetre Interferometry*. PhD thesis, University of Cambridge.
- Wikipedia (2023). Volcanes Sierra Negra y Pico de Orizaba. https://es.m.wikipedia.org/wiki/Archivo:Volcanes_Sierra_Negra_y_Pico_de_Orizaba_-_panoramio.jpg.
- Wilson, T. L., Rohlfs, K., & Hüttemeister, S. (2013). *Tools of Radio Astronomy*. Astronomy and Astrophysics Library. Springer, 6 edition.
- Xilinx, Inc. (2020). Zynq UltraScale+ RFSoc RF Data Converter v2.4 Gen 1/2/3 Product Guide. <https://docs.xilinx.com/v/u/2.4-English/pg269-rf-data-converter>.
- Xilinx, Inc. (2023). RFSoc 2x2 Kit. <https://www.xilinx.com/support/university/xup-boards/RFSoc2x2.html>.
- Zeballos, M., Ferrusca, D., Contreras, J., & Hughes, D. H. (2016). Reporting the first 3 years of 225-GHz opacity measurements at the site of the Large Millimeter Telescope Alfonso Serrano. *Ground-based and Airborne Telescopes VI*, 9906, 99064U, <https://doi.org/10.1117/12.2232168>.

APPENDIX A

CASA TOOLS: ATMOSPHERE

In this appendix we discuss the use of *atmosphere* tool to obtain atmospheric profiles for a certain observatory. A brief description of the CASA package is presented followed by an explanation of the computing process. Finally, we provide an example script to get atmospheric opacity and transmission at a given site.

The *Common Astronomy Software Applications* (CASA) is a set of virtual libraries provided by National Radio Astronomy Observatory (NRAO). CASA is the main data processing software for the NRAO's sites, the VLA and ALMA. This software is intended to perform data reduction and imaging for both single-dish and aperture-synthesis telescopes.

Among all CASA's tools is *atmosphere*, an algorithm which allows to generate practical Earth's atmosphere models in radio frequency bands. *atmosphere* is based on the *Atmospheric Transmission at Microwaves* (ATM) originally developed by Pardo et al. (2001). Both *atmosphere* and ATM perform radiative transfer algorithms to get atmospheric variables for a given atmospheric profile and spectral window. In this way, several atmospheric variables can be obtained.

First of all, the user must install the complete CASA package¹ on a local computer (see CASA (2023)). We highly suggest consulting the complete atmosphere documentation in CASA (2021), where detailed information about the commands used here can be found. So, the construction of the desired atmospheric model is based on three basic steps:

1. Generate the *atmospheric profile* for the desired site. Weather and thermodynamic parameters of the site are required in this step.
2. Set up the desired *spectral window* to characterize the model parameters. Bandwidth, center frequency and resolution must be known.
3. Request the *atmospheric variables* solved at the spectral window.

Then, the user can process and analyze the resulting data into the CASA local environment or a third-party processing software. We detail these steps in the following.

¹It should be noted that CASA only supports Linux distributions and MacOS® systems.

A.1 Atmospheric Profile

The atmospheric profile is generated using weather and thermodynamic variables of the site. Such variables are computed in defined atmospheric layers with the method `initAtmProfile()`. The arguments of this method and their statements are shown in Table A.1.

Table A.1: Arguments requested by `initAtmProfile` method.

Statement	Default value	Units	Definition
<code>altitude</code>	—	m	Altitude of the site (above sea level)
<code>temperature</code>	—	K	Temperature at the ground
<code>pressure</code>	—	mbar	Pressure at the ground
<code>humidity</code>	20.0	%	Relative humidity at the ground
<code>maxAltitude</code>	48.8	km	Top height of atmospheric profile
<code>dTem_dh</code>	-5.6	K km ⁻¹	Tropospheric temperature lapse rate
<code>dP</code>	10	mbar	Initial step of pressure
<code>dPm</code>	1.2	—	Multiplicative factor of pressure steps
<code>h0</code>	2	km	Scale height of water vapor
<code>atmType</code>	3	—	Atmosphere type

Note that ‘ground’ arguments are strictly user-defined variables (except for the relative humidity parameter) and so, there are not default values set by the algorithm. On the other hand, the available atmosphere types can be any of the following: Tropical (1); Mid latitude summer (2); Mid latitude winter (3); Subarctic summer(4); Subarctic winter (5).

The user can modify the current atmospheric profile by updating all or single arguments using `updateAtmProfile()` in the same way as `initAtmProfile()`. Additionally, the method `getProfile()` returns the current values of the atmospheric profile.

A.2 Spectral Window

The spectral window is used to compute sky parameters on the defined atmospheric profile. In this step, the user defines the number of spectral windows with their respective central frequency, bandwidth, and the step frequency (resolution). The `initSpectralWindow()` method is used for this purpose, and Table A.2 describes its arguments. If the user needs to append another spectral window, the `addSpectralWindow()` method should be called with the above arguments modified at the user’s discretion. Additionally, if the user calls the `getSpectralWindow()` method, the frequency values of the current window will be shown.

Table A.2: Arguments requested by `initSpectralWindow` method.

Statement	Default value	Units	Definition
<code>nbands</code>	—	—	Number of spectral windows to construct
<code>fCenter</code>	—	GHz	central frequency of the window
<code>fWidth</code>	—	GHz	Bandwidth centered at <code>fCenter</code>
<code>fRes</code>	—	GHz	Resolution frequency for <code>fWidth</code>

A.3 Atmospheric Variables

Once the atmospheric profile and the spectral window are defined, the user can request the variables shown in Table A.3. The results are given for a specified window.

Table A.3: Some *atmosphere's* variables on demand by the user.

Method	Returns	Units
<code>getTebbSkySpec()</code>	Sky brightness temperature	K
<code>getDryOpacity()</code>	Dry opacity	—
<code>getWetOpacity()</code>	Wet opacity	—
<code>getGroundWH20()</code>	Precipitable water vapor column	mm
<code>getAirMass()</code>	Airmass	—

The table only shows methods related to this work. However, various methods can be found in the *atmosphere's* API, which can compute Rayleigh-Jeans temperature, phase delay, absorption coefficients, among others. Some of these methods calculate the respective variables independently or due to molecular species such as H₂O, O₂, O₃, CO, NO₂ and SO₂.

A.4 Practical Example

Radio astronomical observatories have a well-known transmission profile, which describes the quality of the atmosphere in a certain spectral window. This profile is another crucial tool that helps the astronomer to plan observations and calibrate the data within the operating frequency bands of the telescope or interferometer. Lets see an example which computes atmospheric transmission at the VLA site. The script has been developed based on the three steps mentioned before and the transmission is calculated for the VLA's frequency band under mean weather values at a winter season.

First, we call the *atmosphere* class as `at` for every method mentioned in this section. Then, the atmospheric profile and the spectral window are constructed using the values of Table A.4 and some default values of Table A.1 (see Appendix A.1). As a result, a text file that contains the frequency step, opacity and transmission is generated.

Table A.4: VLA's weather conditions and spectral window arguments.

Statement	Value	Units	Description
<code>altitude</code>	2124	masl	Altitude
<code>temperature</code>	290	K	Temperature at the ground
<code>pressure</code>	780	mbar	Pressure at the ground
<code>humidity</code>	20	%	Relative humidity at the ground
<code>atmType</code>	3	—	Mid latitude winter atmosphere
<code>nbands</code>	1	—	Spectral windows
<code>fCenter</code>	25.5	GHz	central frequency
<code>fWidth</code>	49	GHz	Bandwidth
<code>fRes</code>	100	MHz	Spectral resolution

By default, opacity calculations are computed at the zenith of the site (i.e. $X = 1$), which is the case in this example. If the user prefers to compute at another airmass, the `setAirMass()` method with the desired value must be used. In addition, we set a simulated water vapor column of 2 mm using the method `setUserWH20("2mm")`.

atmosphere performs radiative transfer calculations by atmospheric layers. In this way, the background temperature $T_{b,0}$ is the input temperature of the current atmospheric layer. If there is only one atmospheric layer in the model, $T_{b,0}$ is the temperature of the outer space, obviously. Since this example executes a single atmospheric layer, the input temperature should be the cosmic microwave background temperature $T_{\text{cmb}} = 2.73$ K.

All sky parameters are calculated by a radiative transfer algorithm. So, it is important to have defined the background temperature and the spectral window before a sky parameter is required. The method `setSkyBackgroundTemperature()` helps to define the background temperature and the method `getSpectralWindow()` creates the spectral window.

The atmospheric transmission is not natively computed by *atmosphere*. However, the user can estimate it using the `getDryOpacity()` and `getWetOpacity()` methods, which give the dry and wet opacity respectively. The example script computes the transmission \mathcal{T} we have defined Section 3.2 as

$$\mathcal{T} = e^{-\tau_0}, \quad (\text{A.1})$$

where τ_0 is the zenith opacity given by the sum of opacities of a *dry* and a *wet* atmosphere as

$$\tau_0 = \tau_{\text{dry}} + \tau_{\text{wet}}. \quad (\text{A.2})$$

It can be noted that Eq. (A.2) is practically the same expression as Eq. (3.13), from which we can assume that

$$\tau_{\text{wet}} = \alpha_v PWV. \quad (\text{A.3})$$

atmosphere does not include methods for creating text files, but CASA does, since this package is a *Python*-based environment. So that, the user can get the parameter in a register using any *Python* package for such task. This is the last process done by the script.

The code of this example is shown in Script B.9 is executed within a CASA session by typing `execfile('script.py')`. The resulting text file is saved in the local CASA's folder on the user's computer. Finally, the user can analyze and plot the data with a software of his choice. For illustrative purposes, transmission and opacity profiles were plotted using *Matplotlib* library. Fig. A.1 shows the results.

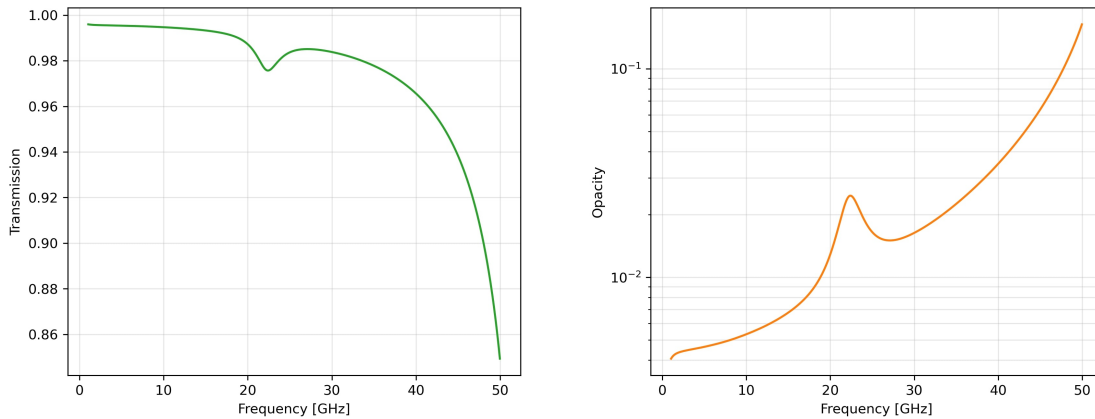


Fig. A.1: Left: Transmission at the VLA site. Right: Zenith opacity. The PWV was 2 mm.

The user can go further and generate transmission curves for several values of PWV as reported by many radio astronomy observatories. Fig. A.2 shows an example for the VLA site.

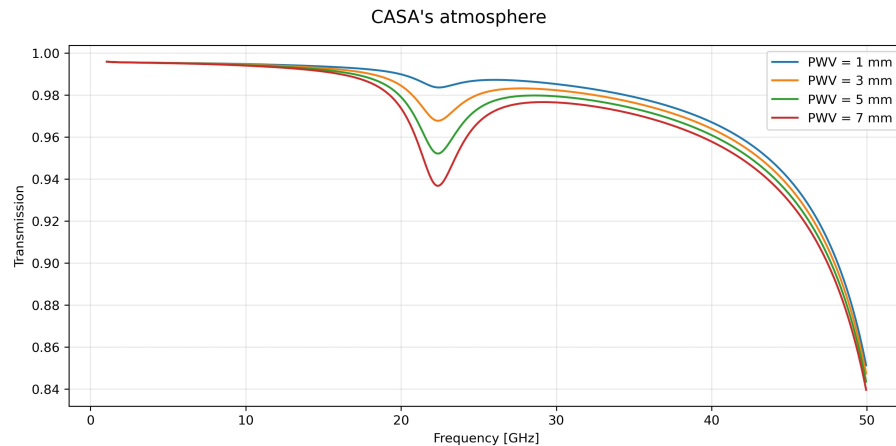


Fig. A.2: Atmospheric transmission for different PWV values at VLA.

As can be seen, *atmosphere* is a useful tool for sky characterization, providing several methods to compute substantial parameters. Due to *Python* support, the user can develop scripts with native language dependencies as well as third-party libraries within the CASA environment.

APPENDIX B

SCRIPTS

Script B.1: Generate tip-curves from atmospheric scan.

```
1 import numpy as np
2 import matplotlib.pyplot as plt
3
4 Trx = 80
5 Tatm = 277
6 Tcmb = 2.73
7 tau0 = [0.1,0.3,0.5,0.7,1.0]
8 zangle = np.arange(0,72,1)
9 am = 1/(np.cos(np.deg2rad(zangle)))
10
11 plt.figure(1,figsize=(10,4))
12 plt.xlabel('Air Mass')
13 plt.ylabel(r'$T_{sys}$')
14
15 for t in tau0:
16     Tsys = Tcmb + Trx + (t*am)*Tatm
17     plt.plot(am, Tsys, label=r'$\tau_0 = $ ' + str(t))
18
19 plt.grid(True, which='both',alpha=0.3)
20 plt.legend()
21 plt.savefig('tip_curve.png', dpi=300, bbox_inches = 'tight')
22 plt.show()
```

Script B.2: Generate atmospheric profiles with relative humidity as parameter.

```

1 import numpy as np
2
3 rhum = np.array(np.linspace(10,100,10,dtype=float))
4
5 open('tau_rh.txt','w').close()
6 for rh in rhum:
7     print('RH = ' + str(rh))
8     at.initAtmProfile(humidity=rh, temperature="270K", altitude="2124m", pressure="
9     790mbar", atmType=3, maxAltitude="18km")
10    at.initSpectralWindow(1,fCenter="22.235GHz", fWidth="1MHz", fRes="1MHz")
11    at.setAirMass(1.0)
12    at.setSkyBackgroundTemperature(qa.quantity(2.73,'K'))
13    at.getSpectralWindow()
14    freq = at.getChanFreq(0,0)['value'][0]
15    pwv = at.getGroundWH20()['value'][0]
16    tauD = at.getDryOpacity(0,0)
17    tauW = at.getWetOpacity(0,0)['value'][0]
18    tot_tau = tauD + tauW
19    data = open('tau_rh.txt','a')
20    data.write("{:0.3f},{:0.1f},{:0.2f},{:0.6f}".format(freq,rh,pwv,tot_tau) + "\n")
21    data.close()
22 print("Model generated successfully!")

```

Script B.3: Calculate integration time for given values of SNR.

```

1 import numpy as np
2 import matplotlib.pyplot as plt
3
4 fr = np.loadtxt('sim_vla.txt',delimiter=',',usecols=0)
5 tb = np.loadtxt('sim_vla.txt',delimiter=',',usecols=3)
6
7 Tsky = np.round(np.mean(tb),4)
8 bw = [50,100,250,500]
9 Trx = 275
10 Tcmb = 2.73
11 SNR = np.arange(10,1e3,1)
12 Tsys = Trx + Tcmb
13
14 plt.figure(1,figsize=(8,4))
15 plt.ylabel('Integration Time [s]')
16 plt.xlabel('Signal-to-Noise Ratio')
17 plt.xscale('log')
18 plt.yscale('log')
19
20 for dnu in bw:
21     t = (SNR*(Tsys/Tsky))**2 / (dnu*1e6)
22     plt.plot(SNR,t,label=r'$\Delta\nu = $ ' + str(dnu) + ' MHz')
23
24 plt.grid(True, which='both',alpha=0.3)
25 plt.legend()
26 plt.savefig('snr_t.png', dpi=300, bbox_inches = 'tight')
27 plt.show()

```

Script B.4: Generate atmospheric profile around the 22 GHz band.

```
1 import numpy as np
2
3 vla = at.initAtmProfile(humidity=20, temperature="290K", altitude="2124m", pressure="
    780mbar", atmType=3, maxAltitude="18km")
4 spw = at.initSpectralWindow(1,fCenter="22.5GHz", fWidth="4GHz", fRes="0.4MHz")
5 at.setAirMass(1.0)
6 at.setUserWH20("2mm")
7 at.setSkyBackgroundTemperature(qa.quantity(2.73,'K'))
8 at.getSpectralWindow()
9
10 open('krx_atm.txt','w').close()
11
12 for i in range(spw):
13     freq = at.getChanFreq(i,0)['value'][0]
14     tauD = at.getDryOpacity(i,0)
15     tauW = at.getWetOpacity(i,0)['value'][0]
16     tot_tau = tauD + tauW
17     Tr = np.exp(-(tot_tau))
18     Tatm = at.getTebbSky(i,0)['value'][0]
19
20     data = open('krx_atm.txt','a')
21     data.write("{:0.6f},{:0.6f},{:0.6f},{:0.6f}".format(freq,tot_tau,Tr,Tatm) + "\n")
22     data.close()
23
24 print("Model generated successfully!")
```

Script B.5: Data divider by groups of n elements

```
1 with open("krx_atm_10k.txt", "r") as file:
2     lines = file.readlines()
3
4 group_size = 10
5 subdivided_data = []
6
7 for i in range(0, len(lines), group_size):
8     group = lines[i:i+group_size]
9     subdivided_data.append(group)
10
11 column0_averages = []
12 column3_averages = []
13
14 for group in subdivided_data:
15     values_column0 = []
16     values_column3 = []
17
18     for line in group:
19         values = line.strip().split(",")
20         value_column0 = float(values[0])
21         value_column3 = float(values[3])
22         values_column0.append(value_column0)
23         values_column3.append(value_column3)
24
25     average_column0 = round(sum(values_column0) / len(values_column0),4)
26     average_column3 = round(sum(values_column3) / len(values_column3),4)
27
28     column0_averages.append(average_column0)
29     column3_averages.append(average_column3)
30
31 with open("promedios_columnas_1.txt", "w") as output_file:
32     for avg_col0, avg_col3 in zip(column0_averages, column3_averages):
33         output_file.write(f"{avg_col0},{avg_col3}\n")
```

Script B.6: Spectrum acquisition on CHA.

```
1 import sys, time, struct
2 import numpy as np
3 from numpy import fft
4 import matplotlib.pyplot as plt
5 import matplotlib.animation as anim
6 import casperfpga
7 from adc_utils import *
8
9 def get_vacc_data(fpga, nchannels=8, nfft=64):
10     acc_n = fpga.read_uint('acc_cnt')
11     chunk = nfft//nchannels
12
13     raw = np.zeros((nchannels, chunk))
14     for i in range(nchannels):
15         raw[i,:] = struct.unpack('>{:d}Q'.format(chunk), fpga.read('q{:d}'.format((i+1)),
16             chunk*8,0))
17     interleave_q = []
18     for i in range(chunk):
19         for j in range(nchannels):
20             interleave_q.append(raw[j,i])
21     return acc_n, np.array(interleave_q, dtype=np.float64)
22
23 def plot_spectrum(fpga, cx=True, num_acc_updates=None):
24     fig = plt.figure(figsize=(12,5))
25     ax = fig.add_subplot(111)
26     ax.grid();
27
28     fs = 3932.16/2
29     if cx:
30         print('complex design')
31         Nfft = 2**6
32         fbins = np.arange(-Nfft//2, Nfft//2)
33         nchannels = 8
34         df = fs/Nfft
35         faxis = fbins*df + fs/2
36     else:
37         print('real design')
38         Nfft = 2**6
39         fbins = np.arange(0, Nfft//2)
40         df = fs/Nfft
41         nchannels = 4
42         faxis = fbins*df
43
44     if cx:
45         acc_n, spectrum = get_vacc_data(fpga, nchannels=nchannels, nfft=Nfft)
46         power = 0.6712*(10*np.log10(fft.fftshift(spectrum))) -93.1318
47         line, = ax.plot(faxis,power, color='darkslategray')
48         data = np.column_stack((faxis,power))
49         np.savetxt('spectrum_CHA.txt', datos, delimiter=',', fmt='%f')
50     else:
51         acc_n, spectrum = get_vacc_data(fpga, nchannels=nchannels, nfft=Nfft//2)
52         power = 0.6712*(10*np.log10(fft.fftshift(spectrum))) -93.1318
53         line, = ax.plot(faxis,power, color='darkslategray')
```

```

54
55 ax.set_ylim(-100,10)
56 ax.set_xlabel('Frequency [MHz]')
57 ax.set_ylabel('Power [dBm]')
58
59 def update(frame, *fargs):
60     if cx:
61         acc_n, spectrum = get_vacc_data(fpga, nchannels=nchannels, nfft=Nfft)
62         power = 0.6712*(10*np.log10(fft.fftshift(spectrum))) -93.1318
63         line.set_ydata(power)
64     else:
65         acc_n, spectrum = get_vacc_data(fpga, nchannels=nchannels, nfft=Nfft//2)
66         power = 0.6712*(10*np.log10(fft.fftshift(spectrum))) -93.1318
67         line.set_ydata(power)
68     ax.set_title('Acquiring on CHA || %d' % acc_n)
69
70 v = anim.FuncAnimation(fig, update, frames=1, repeat=True, fargs=None, interval
71                        =1000)
72 plt.show()
73
74 if __name__ == "__main__":
75     from optparse import OptionParser
76
77     p = OptionParser()
78     p.set_usage('rfsoc4x2_tut_spec.py <HOSTNAME_or_IP> cx|real [options]')
79     p.set_description(__doc__)
80     p.add_option('-l', '--acc_len', dest='acc_len', type='int', default=2*(2**28)//2048,
81                help='Set the number of vectors to accumulate between dumps. default is
82                    2*(2^28)/2048')
83     p.add_option('-s', '--skip', dest='skip', action='store_true',
84                help='Skip programming and begin to plot data')
85     p.add_option('-b', '--fpg', dest='fpgfile', type='str', default='',
86                help='Specify the fpg file to load')
87     p.add_option('-a', '--adc', dest='adc_chan_sel', type=int, default=1,
88                help='adc input to select values are 0 or 1')
89
90     opts, args = p.parse_args(sys.argv[1:])
91     if len(args) < 2:
92         print('Specify a hostname or IP for your casper platform. And either cx|real to
93             indicate the type of spectrometer design.\n'
94             'Run with the -h flag to see all options.')
95         exit()
96     else:
97         hostname = args[0]
98         mode_str = args[1]
99         if mode_str=='cx':
100             mode = 1
101         elif mode_str=='real':
102             mode = 0
103         else:
104             print('operation mode not recognized, must be "cx" or "real"')
105             exit()
106
107     if opts.fpgfile != '':
108         bitstream = opts.fpgfile
109     else:

```

```

107     if mode == 1:
108         fpg_prebuilt = '/home/jetzael/Casper/mlib_devel/projects_4/rad_spec/outputs/
rad_spec_2023-10-07_1725.fpg'
109     else:
110         fpg_prebuilt = '/home/jetzael/Casper/mlib_devel/projects_3/espectrometro2/
outputs/espectrometro2_2023-10-06_1555.fpg'
111     print('using prebuilt fpg file at %s' % fpg_prebuilt)
112     bitstream = fpg_prebuilt
113
114     if opts.adc_chan_sel < 0 or opts.adc_chan_sel > 3:
115         print('adc select must be 0,1,2, or 3')
116         exit()
117
118     print('Connecting to %s... ' % (hostname))
119     fpga = casperfpga.CasperFpga(hostname)
120     time.sleep(0.2)
121
122     print('Inizializing RFDC blocks...')
123     fpga.upload_to_ram_and_program('/home/jetzael/Casper/mlib_devel/projects_3/read_adc
/outputs/read_adc_ultimate.fpg')
124     rfdc_fpga = fpga.adcs['rfdc']
125     rfdc_fpga.init()
126     reloj = rfdc_fpga.show_clk_files()
127     rfdc_fpga.progpll('lmk', reloj[0])
128     rfdc_fpga.progpll('lmx', reloj[1])
129     print("done!")
130
131     if not opts.skip:
132         print('Programming FPGA with %s...'% bitstream)
133         fpga.upload_to_ram_and_program(bitstream)
134         print('done!')
135     else:
136         fpga.get_system_information()
137         print('skip programming fpga...')
138
139     print('Configuring accumulation period...')
140     fpga.write_int('acc_len',opts.acc_len)
141     time.sleep(0.1)
142     print('done!')
143
144     print('setting capture on adc port %d (CHA)' % opts.adc_chan_sel)
145     fpga.write_int('adc_chan_sel', opts.adc_chan_sel)
146     time.sleep(0.1)
147     print('done!')
148
149     print('Resetting counters...')
150     fpga.write_int('cnt_rst',1)
151     fpga.write_int('cnt_rst',0)
152     time.sleep(5)
153     print('done!')
154
155     try:
156         plot_spectrum(fpga, cx=mode)
157     except KeyboardInterrupt:
158         exit()

```


Script B.7: Spectrum acquisition on CHB.

```

1 import sys, time, struct
2 import numpy as np
3 from numpy import fft
4 import matplotlib.pyplot as plt
5 import matplotlib.animation as anim
6 import casperfpga
7 from adc_utils import *
8
9 def get_vacc_data(fpga, nchannels=8, nfft=64):
10     acc_n = fpga.read_uint('acc_cnt')
11     chunk = nfft//nchannels
12
13     raw = np.zeros((nchannels, chunk))
14     for i in range(nchannels):
15         raw[i,:] = struct.unpack('>{:d}Q'.format(chunk), fpga.read('q{:d}'.format((i+1)),
16             chunk*8,0))
17
18     interleave_q = []
19     for i in range(chunk):
20         for j in range(nchannels):
21             interleave_q.append(raw[j,i])
22     return acc_n, np.array(interleave_q, dtype=np.float64)
23
24 def plot_spectrum(fpga, cx=True, num_acc_updates=None):
25     fig = plt.figure(figsize=(12,5))
26     ax = fig.add_subplot(111)
27     ax.grid();
28
29     fs = 3932.16/2
30     if cx:
31         print('complex design')
32         Nfft = 2**6
33         fbins = np.arange(-Nfft//2, Nfft//2)
34         nchannels = 8
35         df = fs/Nfft
36         faxis = fbins*df + fs/2
37     else:
38         print('real design')
39         Nfft = 2**6
40         fbins = np.arange(0, Nfft//2)
41         df = fs/Nfft
42         nchannels = 4
43         faxis = fbins*df
44
45     if cx:
46         acc_n, spectrum = get_vacc_data(fpga, nchannels=nchannels, nfft=Nfft)
47         power = 0.7545*(10*np.log10(fft.fftshift(spectrum))) -104.8735
48         line, = ax.plot(faxis,power, color='goldenrod')
49         data = np.column_stack((faxis,power))
50         np.savetxt('spectrum_CHB.txt', datos, delimiter=',', fmt='%f')
51     else:
52         acc_n, spectrum = get_vacc_data(fpga, nchannels=nchannels, nfft=Nfft//2)
53         power = 0.7545*(10*np.log10(fft.fftshift(spectrum))) -104.8735
54         line, = ax.plot(faxis,power, color='goldenrod')

```

```

54
55 ax.set_ylim(-100,10)
56 ax.set_xlabel('Frequency [MHz]')
57 ax.set_ylabel('Power [dBm]')
58
59 def update(frame, *fargs):
60     if cx:
61         acc_n, spectrum = get_vacc_data(fpga, nchannels=nchannels, nfft=Nfft)
62         power = 0.7545*(10*np.log10(fft.fftshift(spectrum))) -104.8735
63         line.set_ydata(power)
64     else:
65         acc_n, spectrum = get_vacc_data(fpga, nchannels=nchannels, nfft=Nfft//2)
66         power = 0.7545*(10*np.log10(fft.fftshift(spectrum))) -104.8735
67         line.set_ydata(power)
68     ax.set_title('Acquiring on CHB || %d' % acc_n)
69
70 v = anim.FuncAnimation(fig, update, frames=1, repeat=True, fargs=None, interval
71                        =1000)
72 plt.show()
73
74 if __name__ == "__main__":
75     from optparse import OptionParser
76
77     p = OptionParser()
78     p.set_usage('rfsoc4x2_tut_spec.py <HOSTNAME_or_IP> cx|real [options]')
79     p.set_description(__doc__)
80     p.add_option('-l', '--acc_len', dest='acc_len', type='int', default=2*(2**28)//2048,
81                 help='Set the number of vectors to accumulate between dumps. default is
82                      2*(2^28)/2048')
83     p.add_option('-s', '--skip', dest='skip', action='store_true',
84                 help='Skip programming and begin to plot data')
85     p.add_option('-b', '--fpg', dest='fpgfile', type='str', default='',
86                 help='Specify the fpg file to load')
87     p.add_option('-a', '--adc', dest='adc_chan_sel', type=int, default=0,
88                 help='adc input to select values are 0 or 1')
89
90     opts, args = p.parse_args(sys.argv[1:])
91     if len(args) < 2:
92         print('Specify a hostname or IP for your casper platform. And either cx|real to
93               indicate the type of spectrometer design.\n'
94               'Run with the -h flag to see all options.')
95         exit()
96     else:
97         hostname = args[0]
98         mode_str = args[1]
99         if mode_str=='cx':
100             mode = 1
101         elif mode_str=='real':
102             mode = 0
103         else:
104             print('operation mode not recognized, must be "cx" or "real"')
105             exit()
106
107     if opts.fpgfile != '':
108         bitstream = opts.fpgfile
109     else:

```

```
107     if mode == 1:
108         fpg_prebuilt = '/home/jetzael/Casper/mlib_devel/projects_4/rad_spec/outputs/
rad_spec_2023-10-07_1725.fpg'
109     else:
110         fpg_prebuilt = '/home/jetzael/Casper/mlib_devel/projects_3/espectrometro2/
outputs/espectrometro2_2023-10-06_1555.fpg'
111     print('using prebuilt fpg file at %s' % fpg_prebuilt)
112     bitstream = fpg_prebuilt
113
114     if opts.adc_chan_sel < 0 or opts.adc_chan_sel > 3:
115         print('adc select must be 0,1,2, or 3')
116         exit()
117
118     print('Connecting to %s... ' % (hostname))
119     fpga = casperfpga.CasperFpga(hostname)
120     time.sleep(0.2)
121
122     print('Initializing RFDC blocks...')
123     fpga.upload_to_ram_and_program('/home/jetzael/Casper/mlib_devel/projects_3/read_adc
/outputs/read_adc_ultimate.fpg')
124     rfdc_fpga = fpga.adcs['rfdc']
125     rfdc_fpga.init()
126     reloj = rfdc_fpga.show_clk_files()
127     rfdc_fpga.progppll('lmk', reloj[0])
128     rfdc_fpga.progppll('lmx', reloj[1])
129     print("done!")
130
131     if not opts.skip:
132         print('Programming FPGA with %s...' % bitstream)
133         fpga.upload_to_ram_and_program(bitstream)
134         print('done!')
135     else:
136         fpga.get_system_information()
137         print('skip programming fpga...')
138
139     print('Configuring accumulation period...')
140     fpga.write_int('acc_len',opts.acc_len)
141     time.sleep(0.1)
142     print('done!')
143
144     print('setting capture on adc port %d (CHB)' % opts.adc_chan_sel)
145     fpga.write_int('adc_chan_sel', opts.adc_chan_sel)
146     time.sleep(0.1)
147     print('done!')
148
149     print('Resetting counters...')
150     fpga.write_int('cnt_rst',1)
151     fpga.write_int('cnt_rst',0)
152     time.sleep(5)
153     print('done!')
154
155     try:
156         plot_spectrum(fpga, cx=mode)
157     except KeyboardInterrupt:
158         exit()
```

Script B.8: RFDC utilities for spectrum acquisition.

```
1 def toSigned(v, bits):
2     mask = 1 << (bits-1)
3     return -(v & mask) | (v & (mask-1))
4
5 def capture_snapshots(fpga):
6     snapshot_data = {}
7     for ss in fpga.snapshots:
8         ss.arm()
9     fpga.registers.snapshot_ctrl.write(start='pulse')
10    for ss in fpga.snapshots:
11        dat = ss.read(arm=False)['data']
12        for (k,v) in dat.items():
13            snapshot_data[k] = v
14    return snapshot_data
15
16 def deinterleave_dual(I, Q, bits=16):
17     x = []
18     for (i, q) in zip(I, Q):
19         I0 = toSigned(0xffff & (i >> 0) , bits)
20         I1 = toSigned(0xffff & (i >> 16), bits)
21         I2 = toSigned(0xffff & (i >> 32), bits)
22         I3 = toSigned(0xffff & (i >> 48), bits)
23
24         Q0 = toSigned(0xffff & (q >> 0) , bits)
25         Q1 = toSigned(0xffff & (q >> 16), bits)
26         Q2 = toSigned(0xffff & (q >> 32), bits)
27         Q3 = toSigned(0xffff & (q >> 48), bits)
28
29         x0 = I0 + 1j*Q0
30         x1 = I1 + 1j*Q1
31         x2 = I2 + 1j*Q2
32         x3 = I3 + 1j*Q3
33
34         x.append(x0)
35         x.append(x1)
36         x.append(x2)
37         x.append(x3)
38    return x
39
40 def deinterleave_quad(samples, bits=16):
41     x = []
42     for s in samples:
43         I0 = toSigned(0xffff & (s >> 0) , bits)
44         Q0 = toSigned(0xffff & (s >> 16), bits)
45         I1 = toSigned(0xffff & (s >> 32), bits)
46         Q1 = toSigned(0xffff & (s >> 48), bits)
47
48         x0 = I0 + 1j*Q0
49         x1 = I1 + 1j*Q1
50
51         x.append(x0)
52         x.append(x1)
53    return x
```

Script B.9: Generate atmospheric profile for the VLA operative band.

```
1 import numpy as np
2
3 vla = at.initAtmProfile(humidity=20, temperature="290K", altitude="2124m", pressure="
    780mbar", atmType=3, maxAltitude="18km")
4 spw = at.initSpectralWindow(1,fCenter="25.5GHz", fWidth="49GHz", fRes="100MHz")
5 at.setAirMass(1.0)
6 at.setUserWH20("2mm")
7 at.setSkyBackgroundTemperature(qa.quantity(2.73,'K'))
8 at.getSpectralWindow()
9
10 open('sim_vla_2mm.txt','w').close()
11
12 for i in range(spw):
13     freq = at.getChanFreq(i,0)['value'][0]
14     tauD = at.getDryOpacity(i,0)
15     tauW = at.getWetOpacity(i,0)['value'][0]
16     tot_tau = tauD + tauW
17     Tr = np.exp(-(tot_tau))
18     Tatm = at.getTebbSky(i,0)['value'][0]
19
20     data = open('sim_vla_2mm.txt','a')
21     data.write("{:0.6f},{:0.6f},{:0.6f},{:0.6f}".format(freq,tot_tau,Tr,Tatm) + "\n")
22     data.close()
23
24 print("Model generated successfully!")
```

APPENDIX C

SCHEMATICS

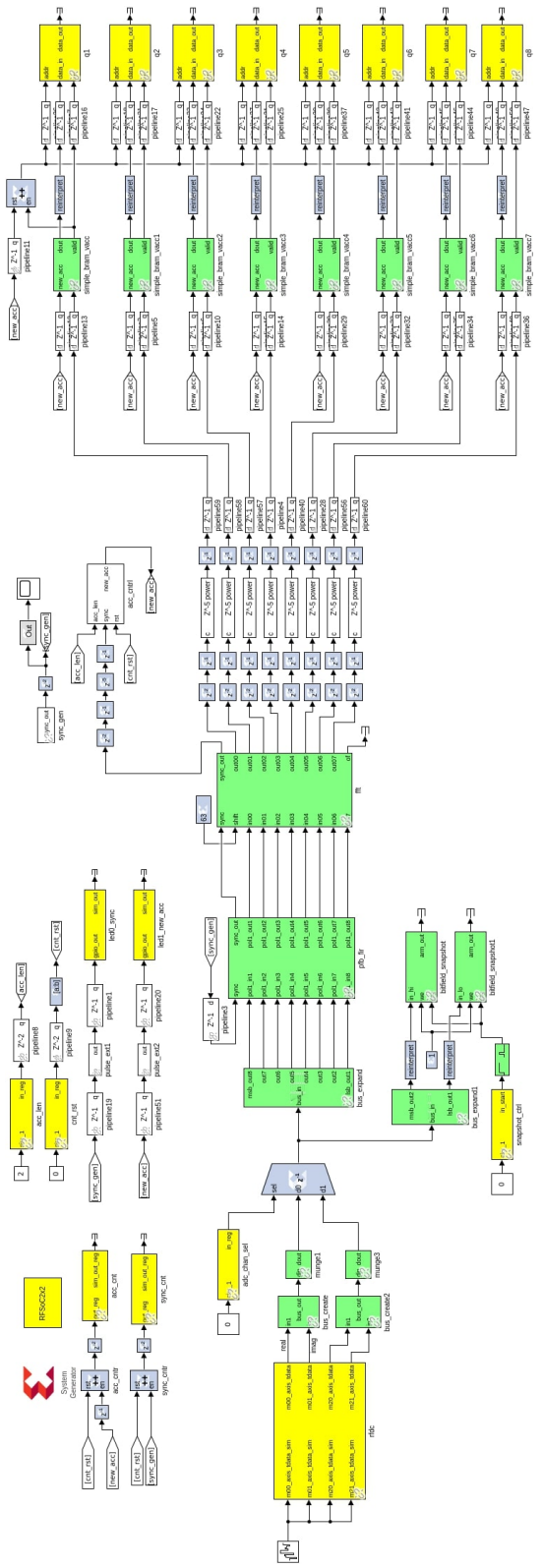


Fig. C.1: Digital spectrometer block diagram.

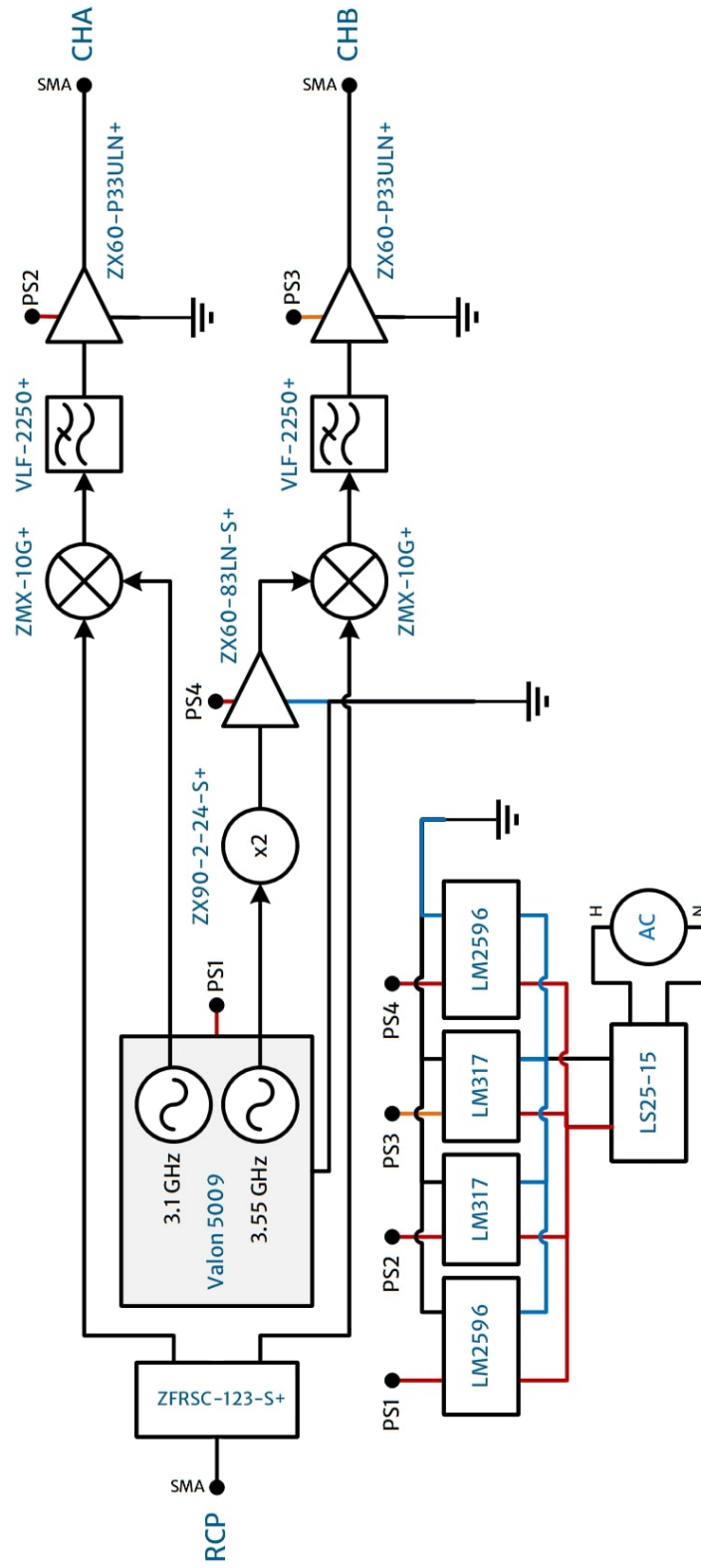


Fig. C.2: Down-conversion connections.

INTERMODULATION PRODUCTS

Intermodulation products are spurious signals generated in a mixing system: when an RF signal is mixed with that of the local oscillator, both the mix of the fundamental and the mix of the RF and LO harmonics are produced in the IF. Ideally, we should only get the desired signal in the IF, but due to the non-linearity of the electronics, additional unwanted components are also generated in the IF ([Gustrau, 2012](#)).

In a mixing stage, the intermodulation products are given by the combination of harmonics of the form:

$$v_{\text{IP(th)}} = m v_{\text{RF}} + n v_{\text{LO}}, \quad (\text{D.1})$$

where $m, n = 0, \pm 1, \pm 2, \pm 3, \dots$, and they determine the *order* (th) of the product as

$$|m| + |n|.$$

When $m + n = 2$, the products are located far from v_{RF} and v_{LO} and can be easily rejected from the IF. Nevertheless, the *third-order products* (IP3), and especially terms with $m = \pm 1, \pm 2$ and $n = \pm 1, \pm 2$, appear within the IF passband. In practice, the IP3 and higher-order products may represent a spurious problem by the subsequent stages of the receiver chain if the power of the desired and the local oscillator signals are high enough ([Pozar, 2011](#)).

We present the third-order intermodulation products resulting from the combination of the RF band and the LO tones in the back-end using m, n values within the interval $[-3, 3]$. Table [D.1](#) shows IP3 terms for the CHA chain, whereas Table [D.2](#) for the CHB chain: we highlight those terms that fall within the back-end band-pass.

Table D.1: IP3 terms for $\nu_{RF} = 3.1$ GHz to 7.1 GHz and $\nu_{LO} = 3.1$ GHz.

m		-3	-2	-1	0	1	2	3	0	1	2	-1	-2
n		0	1	2	3	2	1	0	-3	-2	-1	-2	-1
ν_{RF} [GHz]	ν_{LO} [GHz]	ν_{IP} [GHz]											
3.1	3.1	-9.3	-3.1	3.1	9.3	9.3	9.3	9.3	-9.3	-3.1	3.1	-9.3	-9.3
3.2	3.1	-9.6	-3.3	3.0	9.3	9.4	9.5	9.6	-9.3	-3.0	3.3	-9.4	-9.5
3.3	3.1	-9.9	-3.5	2.9	9.3	9.5	9.7	9.9	-9.3	-2.9	3.5	-9.5	-9.7
3.4	3.1	-10.2	-3.7	2.8	9.3	9.6	9.9	10.2	-9.3	-2.8	3.7	-9.6	-9.9
3.5	3.1	-10.5	-3.9	2.7	9.3	9.7	10.1	10.5	-9.3	-2.7	3.9	-9.7	-10.1
3.6	3.1	-10.8	-4.1	2.6	9.3	9.8	10.3	10.8	-9.3	-2.6	4.1	-9.8	-10.3
3.7	3.1	-11.1	-4.3	2.5	9.3	9.9	10.5	11.1	-9.3	-2.5	4.3	-9.9	-10.5
3.8	3.1	-11.4	-4.5	2.4	9.3	10.0	10.7	11.4	-9.3	-2.4	4.5	-10.0	-10.7
3.9	3.1	-11.7	-4.7	2.3	9.3	10.1	10.9	11.7	-9.3	-2.3	4.7	-10.1	-10.9
4.0	3.1	-12.0	-4.9	2.2	9.3	10.2	11.1	12.0	-9.3	-2.2	4.9	-10.2	-11.1
4.1	3.1	-12.3	-5.1	2.1	9.3	10.3	11.3	12.3	-9.3	-2.1	5.1	-10.3	-11.3
4.2	3.1	-12.6	-5.3	2.0	9.3	10.4	11.5	12.6	-9.3	-2.0	5.3	-10.4	-11.5
4.3	3.1	-12.9	-5.5	1.9	9.3	10.5	11.7	12.9	-9.3	-1.9	5.5	-10.5	-11.7
4.4	3.1	-13.2	-5.7	1.8	9.3	10.6	11.9	13.2	-9.3	-1.8	5.7	-10.6	-11.9
4.5	3.1	-13.5	-5.9	1.7	9.3	10.7	12.1	13.5	-9.3	-1.7	5.9	-10.7	-12.1
4.6	3.1	-13.8	-6.1	1.6	9.3	10.8	12.3	13.8	-9.3	-1.6	6.1	-10.8	-12.3
4.7	3.1	-14.1	-6.3	1.5	9.3	10.9	12.5	14.1	-9.3	-1.5	6.3	-10.9	-12.5
4.8	3.1	-14.4	-6.5	1.4	9.3	11.0	12.7	14.4	-9.3	-1.4	6.5	-11.0	-12.7
4.9	3.1	-14.7	-6.7	1.3	9.3	11.1	12.9	14.7	-9.3	-1.3	6.7	-11.1	-12.9
5.0	3.1	-15.0	-6.9	1.2	9.3	11.2	13.1	15.0	-9.3	-1.2	6.9	-11.2	-13.1
5.1	3.1	-15.3	-7.1	1.1	9.3	11.3	13.3	15.3	-9.3	-1.1	7.1	-11.3	-13.3
5.2	3.1	-15.6	-7.3	1.0	9.3	11.4	13.5	15.6	-9.3	-1.0	7.3	-11.4	-13.5
5.3	3.1	-15.9	-7.5	0.9	9.3	11.5	13.7	15.9	-9.3	-0.9	7.5	-11.5	-13.7
5.4	3.1	-16.2	-7.7	0.8	9.3	11.6	13.9	16.2	-9.3	-0.8	7.7	-11.6	-13.9
5.5	3.1	-16.5	-7.9	0.7	9.3	11.7	14.1	16.5	-9.3	-0.7	7.9	-11.7	-14.1
5.6	3.1	-16.8	-8.1	0.6	9.3	11.8	14.3	16.8	-9.3	-0.6	8.1	-11.8	-14.3
5.7	3.1	-17.1	-8.3	0.5	9.3	11.9	14.5	17.1	-9.3	-0.5	8.3	-11.9	-14.5
5.8	3.1	-17.4	-8.5	0.4	9.3	12.0	14.7	17.4	-9.3	-0.4	8.5	-12.0	-14.7
5.9	3.1	-17.7	-8.7	0.3	9.3	12.1	14.9	17.7	-9.3	-0.3	8.7	-12.1	-14.9
6.0	3.1	-18.0	-8.9	0.2	9.3	12.2	15.1	18.0	-9.3	-0.2	8.9	-12.2	-15.1
6.1	3.1	-18.3	-9.1	0.1	9.3	12.3	15.3	18.3	-9.3	-0.1	9.1	-12.3	-15.3
6.2	3.1	-18.6	-9.3	0.0	9.3	12.4	15.5	18.6	-9.3	0.0	9.3	-12.4	-15.5
6.3	3.1	-18.9	-9.5	-0.1	9.3	12.5	15.7	18.9	-9.3	0.1	9.5	-12.5	-15.7
6.4	3.1	-19.2	-9.7	-0.2	9.3	12.6	15.9	19.2	-9.3	0.2	9.7	-12.6	-15.9
6.5	3.1	-19.5	-9.9	-0.3	9.3	12.7	16.1	19.5	-9.3	0.3	9.9	-12.7	-16.1
6.6	3.1	-19.8	-10.1	-0.4	9.3	12.8	16.3	19.8	-9.3	0.4	10.1	-12.8	-16.3
6.7	3.1	-20.1	-10.3	-0.5	9.3	12.9	16.5	20.1	-9.3	0.5	10.3	-12.9	-16.5
6.8	3.1	-20.4	-10.5	-0.6	9.3	13.0	16.7	20.4	-9.3	0.6	10.5	-13.0	-16.7
6.9	3.1	-20.7	-10.7	-0.7	9.3	13.1	16.9	20.7	-9.3	0.7	10.7	-13.1	-16.9
7.0	3.1	-21.0	-10.9	-0.8	9.3	13.2	17.1	21.0	-9.3	0.8	10.9	-13.2	-17.1
7.1	3.1	-21.3	-11.1	-0.9	9.3	13.3	17.3	21.3	-9.3	0.9	11.1	-13.3	-17.3

Table D.2: IP3 terms for $\nu_{RF} = 3.1$ GHz to 7.1 GHz and $\nu_{LO} = 7.1$ GHz.

		m	-3	-2	-1	0	1	2	3	0	1	2	-1	-2
		n	0	1	2	3	2	1	0	-3	-2	-1	-2	-1
ν_{RF} [GHz]	ν_{LO} [GHz]	ν_{IP} [GHz]												
3.1	7.1	-9.3	0.9	11.1	21.3	17.3	13.3	9.3	-21.3	-11.1	-0.9	-17.3	-13.3	
3.2	7.1	-9.6	0.7	11.0	21.3	17.4	13.5	9.6	-21.3	-11.0	-0.7	-17.4	-13.5	
3.3	7.1	-9.9	0.5	10.9	21.3	17.5	13.7	9.9	-21.3	-10.9	-0.5	-17.5	-13.7	
3.4	7.1	-10.2	0.3	10.8	21.3	17.6	13.9	10.2	-21.3	-10.8	-0.3	-17.6	-13.9	
3.5	7.1	-10.5	0.1	10.7	21.3	17.7	14.1	10.5	-21.3	-10.7	-0.1	-17.7	-14.1	
3.6	7.1	-10.8	-0.1	10.6	21.3	17.8	14.3	10.8	-21.3	-10.6	0.1	-17.8	-14.3	
3.7	7.1	-11.1	-0.3	10.5	21.3	17.9	14.5	11.1	-21.3	-10.5	0.3	-17.9	-14.5	
3.8	7.1	-11.4	-0.5	10.4	21.3	18.0	14.7	11.4	-21.3	-10.4	0.5	-18.0	-14.7	
3.9	7.1	-11.7	-0.7	10.3	21.3	18.1	14.9	11.7	-21.3	-10.3	0.7	-18.1	-14.9	
4.0	7.1	-12.0	-0.9	10.2	21.3	18.2	15.1	12.0	-21.3	-10.2	0.9	-18.2	-15.1	
4.1	7.1	-12.3	-1.1	10.1	21.3	18.3	15.3	12.3	-21.3	-10.1	1.1	-18.3	-15.3	
4.2	7.1	-12.6	-1.3	10.0	21.3	18.4	15.5	12.6	-21.3	-10.0	1.3	-18.4	-15.5	
4.3	7.1	-12.9	-1.5	9.9	21.3	18.5	15.7	12.9	-21.3	-9.9	1.5	-18.5	-15.7	
4.4	7.1	-13.2	-1.7	9.8	21.3	18.6	15.9	13.2	-21.3	-9.8	1.7	-18.6	-15.9	
4.5	7.1	-13.5	-1.9	9.7	21.3	18.7	16.1	13.5	-21.3	-9.7	1.9	-18.7	-16.1	
4.6	7.1	-13.8	-2.1	9.6	21.3	18.8	16.3	13.8	-21.3	-9.6	2.1	-18.8	-16.3	
4.7	7.1	-14.1	-2.3	9.5	21.3	18.9	16.5	14.1	-21.3	-9.5	2.3	-18.9	-16.5	
4.8	7.1	-14.4	-2.5	9.4	21.3	19.0	16.7	14.4	-21.3	-9.4	2.5	-19.0	-16.7	
4.9	7.1	-14.7	-2.7	9.3	21.3	19.1	16.9	14.7	-21.3	-9.3	2.7	-19.1	-16.9	
5.0	7.1	-15.0	-2.9	9.2	21.3	19.2	17.1	15.0	-21.3	-9.2	2.9	-19.2	-17.1	
5.1	7.1	-15.3	-3.1	9.1	21.3	19.3	17.3	15.3	-21.3	-9.1	3.1	-19.3	-17.3	
5.2	7.1	-15.6	-3.3	9.0	21.3	19.4	17.5	15.6	-21.3	-9.0	3.3	-19.4	-17.5	
5.3	7.1	-15.9	-3.5	8.9	21.3	19.5	17.7	15.9	-21.3	-8.9	3.5	-19.5	-17.7	
5.4	7.1	-16.2	-3.7	8.8	21.3	19.6	17.9	16.2	-21.3	-8.8	3.7	-19.6	-17.9	
5.5	7.1	-16.5	-3.9	8.7	21.3	19.7	18.1	16.5	-21.3	-8.7	3.9	-19.7	-18.1	
5.6	7.1	-16.8	-4.1	8.6	21.3	19.8	18.3	16.8	-21.3	-8.6	4.1	-19.8	-18.3	
5.7	7.1	-17.1	-4.3	8.5	21.3	19.9	18.5	17.1	-21.3	-8.5	4.3	-19.9	-18.5	
5.8	7.1	-17.4	-4.5	8.4	21.3	20.0	18.7	17.4	-21.3	-8.4	4.5	-20.0	-18.7	
5.9	7.1	-17.7	-4.7	8.3	21.3	20.1	18.9	17.7	-21.3	-8.3	4.7	-20.1	-18.9	
6.0	7.1	-18.0	-4.9	8.2	21.3	20.2	19.1	18.0	-21.3	-8.2	4.9	-20.2	-19.1	
6.1	7.1	-18.3	-5.1	8.1	21.3	20.3	19.3	18.3	-21.3	-8.1	5.1	-20.3	-19.3	
6.2	7.1	-18.6	-5.3	8.0	21.3	20.4	19.5	18.6	-21.3	-8.0	5.3	-20.4	-19.5	
6.3	7.1	-18.9	-5.5	7.9	21.3	20.5	19.7	18.9	-21.3	-7.9	5.5	-20.5	-19.7	
6.4	7.1	-19.2	-5.7	7.8	21.3	20.6	19.9	19.2	-21.3	-7.8	5.7	-20.6	-19.9	
6.5	7.1	-19.5	-5.9	7.7	21.3	20.7	20.1	19.5	-21.3	-7.7	5.9	-20.7	-20.1	
6.6	7.1	-19.8	-6.1	7.6	21.3	20.8	20.3	19.8	-21.3	-7.6	6.1	-20.8	-20.3	
6.7	7.1	-20.1	-6.3	7.5	21.3	20.9	20.5	20.1	-21.3	-7.5	6.3	-20.9	-20.5	
6.8	7.1	-20.4	-6.5	7.4	21.3	21.0	20.7	20.4	-21.3	-7.4	6.5	-21.0	-20.7	
6.9	7.1	-20.7	-6.7	7.3	21.3	21.1	20.9	20.7	-21.3	-7.3	6.7	-21.1	-20.9	
7.0	7.1	-21.0	-6.9	7.2	21.3	21.2	21.1	21.0	-21.3	-7.2	6.9	-21.2	-21.1	
7.1	7.1	-21.3	-7.1	7.1	21.3	21.3	21.3	21.3	-21.3	-7.1	7.1	-21.3	-21.3	

*Then something happened
which unleashed the power of our imagination.*

S. Hawking